Internal structure and dynamics of extragalactic relativistic jets

INAUGURAL-DISSERTATION

zur
Erlangung des Doktorgrades
der Mathematisch-Naturwissenschaftlichen Fakultät
der Universität zu Köln

vorgelegt von

Mertens Florent
aus Tulle, France

Köln 2015

Berichterstatter:	Prof. Dr. J. Anton Zensus Prof. Dr. Andreas Eckart

Tag der mündlichen Prüfung: 26. Juni 2015

Abstract

Radio-loud AGN typically manifest powerful relativistic jets extending up to millions of light years and often showing superluminal motions organised in a complex kinematic pattern. A number of physical models are still competing to explain the jet structure and kinematics revealed by radio images using the Very Long Baseline Interferometer (VLBI) technique.

Robust measurements of longitudinal and transverse velocity field in the jets would provide crucial information for these models. This is a difficult task, particularly for transversely resolved jets in objects like 3C 273 and M87. To address this task, we have developed a new wavelet-based image segmentation and evaluation (WISE) technique for identifying significant structural patterns (SSP) of smooth, transversely resolved flows and obtaining a velocity field from cross-correlation of these regions in multi-epoch observations. Detection of individual SSP is performed using the wavelet decomposition and multiscale segmentation of the observed structure. The cross-correlation algorithm combines structural information on different scales of the wavelet decomposition, providing a robust and reliable identification of related SSP in multi-epoch images. A stacked cross correlation (SCC) method is also introduced to recover multiple velocity components from partially overlapping, optically thin emitting regions.

Test performed on simulated image of jets revealed excellent performance of WISE. The algorithm enables recovering structural evolution on scales down to 0.25 FWHM of the image point spread function (PSF). It also performs well on sparse or irregular sets of observations, providing robust identification for structural displacements as large as 3 PSF size.

The performance of WISE was further tested on astronomical images by applying it to several image sequences obtained as part of the MOJAVE long-term monitoring program of extragalactic jets with VLBI observations. The particular focus of the analysis was made on prominent radio jets in the quasar 3C 273 and the radio galaxies 3C 120 and 3C 111. Results showed the robustness and fidelity of results obtained from WISE compared with those coming from the “standard” procedure of using multiple Gaussian components to represent the observed structure. These tests demonstrated also the excellent efficiency of the method, with WISE analysis taking only a few minutes of computing time to recover the same structural information which required weeks of model fitting efforts.

Going beyond global one dimensional kinematic analysis, WISE revealed transverse structure in the the jet of 3C 273, with three distinct flow lines clearly present inside the jet and evolving in a regular fashion, suggesting a pattern that may rise as a result of Kelvin-Helmholtz (K-H) instability that has previously been detected in this jet.

The positional precision of the WISE decomposition was also critical on modeling the helical trajectory of the components in the jet of 3C 120, revealing an helical surface mode of the K-H instability with an apparent wavelength $\lambda_{\mathrm{app}} = 15.8\,\mathrm{mas}$

and evolving at an apparent speed $\beta^{w}_{\mathrm{app}} = 2.0\,\mathrm{c}$.

We finally present in this thesis the first detailed transverse velocity fields of the jet in M87 on scales of 10^3–$10^4 r_g$. Its proximity combined with a large mass of the central black hole make it one of the primary source to probe the jet formation and acceleration region. We analyzed 11 epochs of the M87 jet VLBA movie project observed at 3 weeks intervals revealing a structured and stratified flow, compatible with a magnetically launched, accelerated and collimated jet.

Based on the structural analysis obtained with WISE, important physical parameters of the flow could be determined. Using the velocity detected in the counter-jet and the intensity ratio between the jet and counter-jet, we estimated the viewing angle $\theta = 18°$. Differential velocity in the northern and southern limbs of the flow was explained by the jet rotation consistent with a field line with angular velocity $\Omega \sim 10^{-6} s^{-1}$ and corresponding to a launching location in the inner part of the accretion disk.

The stratification in the flow was unveiled from a SCC analysis that detected a slow mildly relativistic layer ($\beta \sim 0.5c$) associated either with the instability pattern speed or an outer wind, and a fast accelerating stream line ($\gamma \sim 2.5$).

The acceleration of the jet together with the collimation profile of the flow, was successfully modeled by solving the magnetohydrodynamics wind equation, indicating a total specific energy $\mu \sim 6$, and a transition from Poynting to kinetic energy at a distance $z_{eq} \sim 3000 R_s$, in a good agreement with previous analytic and simulation work.

Zusammenfassung

Radio-laute aktive Galaxiekerne (AGN) weisen starke relativistische Jets auf, die sich über Millionen Lichtjahre erstrecken und sich häufig in komplexen kinetischen Mustern anordnen, die sich mit Überlichtgeschwindigkeit fortbewegen. Mehrere physikalische Modelle versuchen derzeit die Morphologie und Kinematik von very long baseline interferometry (VLBI) Radio Aufnahmen dieser Objekte zu erklären.

Robuste Messungen longitudinaler und transversaler Geschwindigkeitsfelder innerhalb dieser Jets liefern wichtige Informationen über diese Modelle. Dies stellt eine schwierige Aufgabe dar, insbesondere für transversal aufgelöste Jets, wie sie in 3C 273 und M87 zu finden sind. Um dieses Problem zu lösen haben wir eine wavelet basierte Bildsegmentierungs- und Bewertungstechnik (WISE) für charakteristische strukturelle Muster (SSP) glatter und transversal aufgelöster Flüsse entwickelt. Außerdem lässt sich hierdurch anhand von Aufnahmen, die sich über mehrere Epochen erstrecken, durch Kreuzkorrelation ein Geschwindigkeitsfeld dieser Regionen bestimmen. Die Detektion individueller SSPs erfolgt über eine Waveletdekomposition und Segmentation auf verschiedenen Skalen der beobachteten Struktur. Der Kreuzkorrelationsalgorithmus kombiniert strukturelle Informationen aus verschiedenen Skalen der Wavelet-dekomposition und liefert hierdurch eine belastbare und verlässliche Identifikation von im Zusammenhang stehenden SSPs aus Aufnahmen von mehreren Epochen. Eine stacked cross correlation (SCC) wird ebenfalls benutzt um mehrere Geschwindigkeitskomponenten teilweise überlappender Emissionsregionen zu rekonstruieren.

Tests mit simulierten Aufnahmen von Jets zeigen, dass WISE diese Aufgabe ausgezeichnet erledigt. Der Algorithmus rekonstruiert die strukturelle Evolution auf Skalen bis zum 0.25 fachen des FWHM der PSF dieser Bilder. Es zeigt gut Leistung beim Umgang mit vereinzelt oder irregulär beobachteten Datensätzen und ermöglicht eine robuste Identifikation von Dislokationen bis zur dreifachen PSF Größe.

WISE wurde des weiteren an astronomischen Aufnahmen getestet, in dem es auf verschiedene Sequenzen von VLBI Aufnahmen angewendet wurde, welche im Rahmen des MOJAVE Langzeitaufnahmeprogramms extra galaktischer Jets entstanden sind. Besonderer Fokus wurde auf die bekannten Radio-Jets des Quasars 3C 273 und der Radiogalaxien 3C 120 und 3C 111 gelegt. Die Ergebnisse bestätigen die mit WISE erreichbare Belastbarkeit und Genauigkeit im Vergleich mit den üblichen Methoden, welche multiple Gauss Komponenten nutzen um die beobachtete Struktur darzustellen. WISE ist außerdem hocheffizient. Es ist möglich innerhalb von Minuten die gleiche strukturelle Information zu rekonstruieren für die ansonsten ein Model-fitting Aufwand von Wochen benötigt würde.

Über die globale eindimensionale kinematische Analyse hinaus zeigte WISE eine transversale Struktur innerhalb des Jets von 3C 273 mit drei unterscheidbaren Flusslinien auf, welche sich klar innerhalb des Jets befinden und in regulärer Form entwickeln. Dies legt ein Muster nahe, das sich aus Kelvin-Helmholtz (K-H) Instabilitäten entwickelt, welche früher bereits in diesem Jet detektiert worden sind.

Die Positionsgenauigkeit der Dekomposition von WISE war ein kritischer Faktor in der Modellierung der spiralförmigen Trajektorien der Komponenten des Jets in 3C 120 und zeigte eine spiralförmige Oberflächen-Mode der K-H Instabilität mit einer scheinbaren Wellenlänge $\lambda_{\text{app}} = 15.8$ mas und einer scheinbaren Geschwindigkeit von $\beta_{\text{app}} = 2\ c$ auf.

Abschließend präsentieren wir das erste transversale Geschwindigkeitsfeld des Jets in M87 auf Skalen von 10^3–$10^4 r_g$. Die Kombination aus der unmittelbaren Nähe des Objektes zu uns und der großen Masse des zentralen super-massereichen schwarzen Loches (SMBH) machen es zu einer der primären Quellen um die Entstehung und die Beschleunigungsregion von Jets zu untersuchen. Wir haben 11 Epochen des M87 Jets im Rhythmus von 3 Wochen analysiert, welche einen strukturierten und geschichteten Fluss aufzeigen, der in guter Übereinstimmung mit einem magnetisch in Gang gesetzten, beschleunigten und kollimierten Jet ist.

Wichtige physikalische Parameter des Flusses konnten bestimmt werden. Durch Nutzung der Geschwindigkeiten, welche im Gegenjet detektiert wurden und des Intensitätsverhältnisses zwischen Jet und Gegenjet haben wir einen Beobachtungswinkel von $\theta = 18°$ ermittelt. Die differentielle Geschwindigkeit im nördlichen und südlichen Teil des Jets wurde als Ursache der Jetrotation mit einer Feldlinien Winkelgeschwindigkeit $\Omega \sim 10^{-6} s^{-1}$ interpretiert. Dies entspricht einer Startregion im inneren Teil der Akkretionsscheibe.

Die SSC Analyse zeigt eine Schichtung des Flusses in eine langsame leicht relativistische Schicht ($\beta \sim 0.5c$), welche entweder mit einer Geschwindigkeit des Instabilitätsmusters oder einem äußeren Wind assoziiert ist, und eine schnell beschleunigende Stromlinie ($\gamma \sim 2.5$).

Das Beschleunigungs und Kollimationsprofil des Flusses wurden erfolgreich modelliert indem die magnetohydrodynamische Windgleichung gelöst wurde. Dies liefert Hinweise auf eine spezifische Energie $\mu \sim 6$, und einen Übergang von Poynting zu kinetischer Energie in einer Entfernung von $z_{eq} \sim 3000 R_s$, was in guter Übereinstimmung mit früheren analytischen Arbeiten und Simulationen ist.

Contents

1 Introduction 1
1.1 Active Galactic Nuclei 1
1.2 Imaging an AGN jet 3
1.3 Motivation and organization of the work 5

2 Jet physics 7
2.1 Central engine and accretion disk 7
2.2 Jet launching 9
2.3 Jet acceleration and collimation 11
2.4 Instabilities 12
2.5 Relativistic effects 13

3 Wavelet-based Image Segmentation and Evaluation 15
3.1 Introduction 15
3.2 Wavelet-based image structure evaluation (WISE) algorithm 17
3.2.1 Wavelet transform 17
3.2.2 Conceptual structure of WISE 18
3.3 Segmented wavelet decomposition 20
3.3.1 Determination of significant wavelet coefficients 20
3.3.2 Localization of significant structural patterns 21
3.3.3 Identification of significant structural patterns 22
3.3.4 Uncertainty on the SSP position 23
3.4 Multiscale cross-correlation 23
3.4.1 Multiscale relations 25
3.4.2 Correlation criteria for MCC 26
3.4.3 Detection of SSP displacements 27
3.4.4 Overlapping multiple displacement vectors 30
3.4.5 Intermediate-scales wavelet decomposition 30
3.5 Stacked cross correlation 31
3.5.1 Significance of velocity components 32
3.5.2 Uncertainty on the velocity components 33
3.5.3 Summary 33

4 Testing the WISE algorithm 35
4.1 Introduction . . . 35
4.2 Jet simulation . . . 35
4.3 Sensitivity test . . . 37
4.4 Separation tests . . . 38
4.5 Structural displacement test . . . 39
  4.5.1 Accelerating outflow . . . 40
  4.5.2 Two-fluid outflow . . . 41
4.6 Stacked cross correlation . . . 42
  4.6.1 Summary . . . 45

5 WISE analysis of Mojave sources 47
5.1 Introduction . . . 47
5.2 Analysis of the images . . . 48
5.3 Jet kinematics in 3C 273 . . . 48
5.4 Jet kinematics in 3C 120 . . . 51
5.5 Jet kinematics in 3C 111 . . . 56
5.6 Summary and Discussion . . . 58

6 Kinematics of the jet in M87 on scales of 10^3–$10^4 r_g$ 61
6.1 Introduction . . . 61
  6.1.1 Jet properties at kiloparsec scales . . . 61
  6.1.2 Jet properties at sub-parsec to parsec scales . . . 62
6.2 WISE analysis of 7 mm VLBA observations . . . 64
  6.2.1 Velocity field analysis . . . 64
  6.2.2 Stacked cross correlation analysis . . . 67
    SCC analysis of the jet region between 0.5 and 1 mas from the core . . . 67
    SCC analysis of the jet between 1 and 4 mas from the core . . . 68
  6.2.3 Jet collimation . . . 71
6.3 WISE analysis of 2 cm VLBA observations . . . 73
6.4 Counter jet, viewing angle . . . 74
6.5 Jet rotation . . . 77
6.6 Jet collimation and acceleration . . . 81
  6.6.1 Asymptotic relations in the far-zone Poynting dominated approximation . . . 84
  6.6.2 Wind solutions . . . 87
6.7 Discussion . . . 90
  6.7.1 Stratification . . . 90
  6.7.2 Launching mechanism . . . 91
  6.7.3 Poynting to kinetic energy conversion . . . 92
  6.7.4 Estimate of mass-loss rate . . . 92
6.8 Summary . . . 93

7 Final conclusion and outlook **97**

Bibliography **116**

List of Figures **119**

List of Tables **121**

Chapter 1

Introduction

Astrophysical jets are collimated outflows of plasma. They are found to be associated with a vast range of astrophysical objects, from supermassive black holes in the case of Active Galactic Nuclei (AGN), to stellar mass black holes in microquasars, neutron stars in some X-ray binaries, or protostellar cores in young stellar objects (YSO). The most intriguing and powerful are certainly the relativistic jets launched in some categories of AGN. This PhD is focused on a study of such jets and particularly on their dynamics and internal structure.

1.1 Active Galactic Nuclei

Active galaxies are a class of galaxies hosting a bright compact central regions, also called Active Galactic Nuclei (AGN). The first evidence of active galaxies was found by Carl Seyfard in 1943, when he discovered that some galaxies (Seyfert galaxies) presented very high surface brightness at their nuclei and featured very strong line emission. Later, quasi-stellar objects (Quasars) were discovered as high red-shifted sources with intriguing properties. While they were first observed as point-like, like stars, their luminosity of the order $10^{12}L_\odot$ could not be explained by a stellar origin. A constraint on the mass of those objects can be determined from the Eddington condition that require that gravitational forces on an ionized gas exceed outward radiation pressure. Assuming a spherically symmetric object in hydrostatic equilibrium, an object with luminosity $L = 10^{12}L_\odot$ has to have a mass of the order of $10^7 M_\odot$. The fact that rapid variability was also observed, for which causality arguments would imply that the size of the continuum-emitting region must be of order light days, suggested that this system was matter accreting onto a super-massive black hole. This was one of the first pieces of evidence for the existence of black holes, due to the enormous mass of the body and the small size of the region where it has to be embedded. Several other classes of AGN were later discovered with different flux, spectral, and polarization variability characteristics.

AGN emit radiation in the whole electromagnetic spectrum and exhibit a broad range of luminosities, emission and absorption lines, spectral distributions and mor-

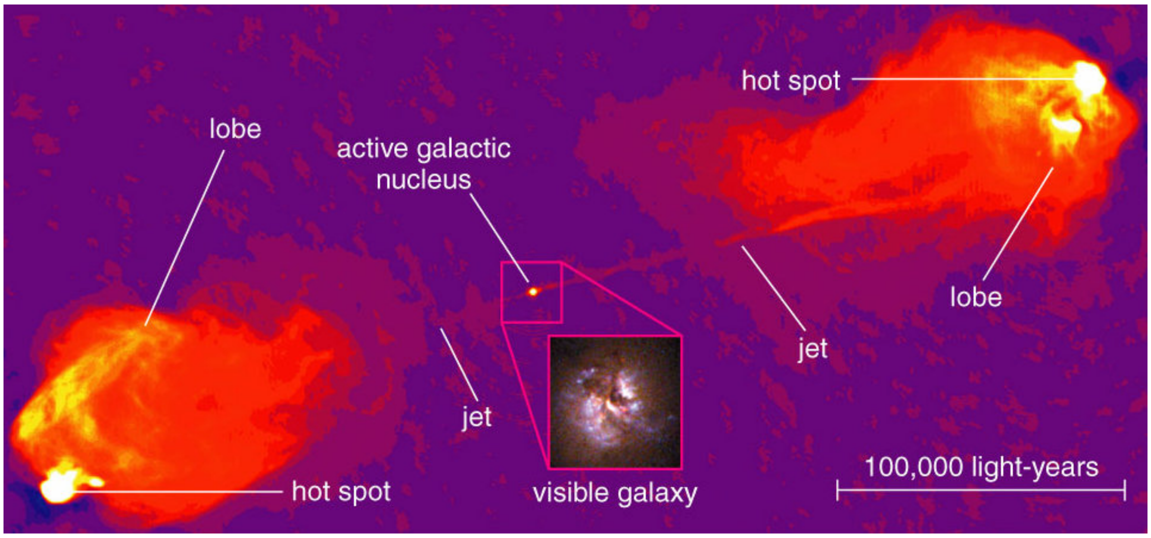

Figure 1.1: VLA image of the 100 kpc long jets in Cygnus A, an AGN with twin relativistic jets that eventually shock against the intergalactic medium producing lobes of synchrotron emission. Credit: NRAO, Pearson Education, Inc., publishing as Addison Wesley.

phologies. One of the main classification treats of AGN is the division between AGN with strong radio emission and AGN with weak or no radio emission. Another important AGN classifiers are the one related to the presence or absence of broad lines in the spectrum and the bolometric luminosity. The weak radio emitters are classified as Seyfert 1 or Seyfert 2 galaxies, depending on the presence of broad or narrow emission lines. Radio galaxies, quasars or blazars are different categories of strong radio emitters with increasing luminosity.

A fraction of AGN, mainly those with intense radio emission, manifest well collimated outflows (jets) ejected from the nucleus and dissipating their energy in the large-scale radio lobes. The bulk of radio emission originates from the jets and lobes, and so the presence of these structures is the main factor distinguishing between radio-loud and radio-quiet AGN. Jets can propagate over extremely large distances, reaching up to more than 1 Mpc. At large scales, two types of radio galaxies (FR I and FR II) are identified, depending on their morphological features [Fanaroff and Riley, 1974]. The FR II are characterized by powerful edge- brightened double lobes with prominent hot-spots and tend to be found in less dense environments, while the FR I have radio emission peaking near the nucleus, have rather edge-darkened lobes and frequently inhabit more dense environments. Cygnus A shown in Fig. 1.1 is a classic FR II radio source. Jets in quasars often appear to be one-sided, although in several objects a second or counter hot-spot is observed. In Blazars, the jets are very compact and one- sided.

Several unification schemes have been proposed to explain this observed diversity [Blandford and Rees, 1978; Urry and Padovani, 1995]. A lot of differences can be explained with changing the viewing angle, i.e., the angle between the orientation of the jet and accretion disk and our line of sight. The central regions of many AGN appear to contain obscuring material, probably in the form of gas and dust. Depending on the orientation, our line of sight would cross materials moving at different speed, explaining the different signature in the width of the emission lines. Superluminal motions have also been detected in some AGN jet [Rees, 1966] which can only be explained if relativistic speed is observed with small viewing angle. Another effect of a relativistic jet is that the radiation is strongly beamed along the jet direction. In this context Blazars and Quasars are objects viewed with a smaller viewing angle compare to radio galaxy, explaining the apparent larger intensity, and the one- sidedness of their jet. The various different class of AGN are summarized in Fig. 1.2.

1.2 Imaging an AGN jet

The electromagnetic radiation from AGN is spread over a wide range of frequencies from radio to γ-rays. The accretion disk emits mainly thermal optical-UV radiation, while the jets emits non-thermal synchrotron and inverse Compton radiation. The synchrotron radiation is emitted by relativistic charged particles when they are radially accelerated through magnetic fields. At kpc scales the jet emission peaks at low frequencies while the inner parsec region mainly emits at higher frequencies reaching up to optical, X-ray, and even gamma-ray regimes. An AGN jet is thus best observed in the radio regime. It should also be noted that some close by AGN jets have also been successfully observed in the optical and X-ray regime using the Hubble Space Telescope (HST) and the Chandra space telescope.

The limited resolution offered by single dish radio telescopes accelerated the development of radio interferometer consisting of an array of telescopes. Using this technique, it is possible to reach angular resolution inversely proportional to the largest distance between two sub-components of the array. Each two elements of an interferometer form an interferometric baseline and measure, at every instant, a particular interferometric visibility, which is one component of the Fourier transform of the spatial distribution of the brightness of the observed object. The total combination of all baseline visibilities comprise a combined measurement of an interferometric response of the observed object in the Fourier domain, also called u-v plane. Through inverse Fourier transform, it is thus possible to recover an image of the observed object. The procedure of creating images from these measurements is called aperture synthesis. For this operation to succeed it is important to measure as many visibilities as possible. This can be done by increasing the number of elements in the array, and designing the layout of the array so that it maximize the number of different baselines. Radio interferometers also take advantage of the rotation of the Earth to increase the number of baseline orientations. Several non-linear deconvolution algorithms have been developed to be able to produce images with a relatively sparse and irregular set of baselines. The CLEAN algorithm [Högbom, 1974] and the

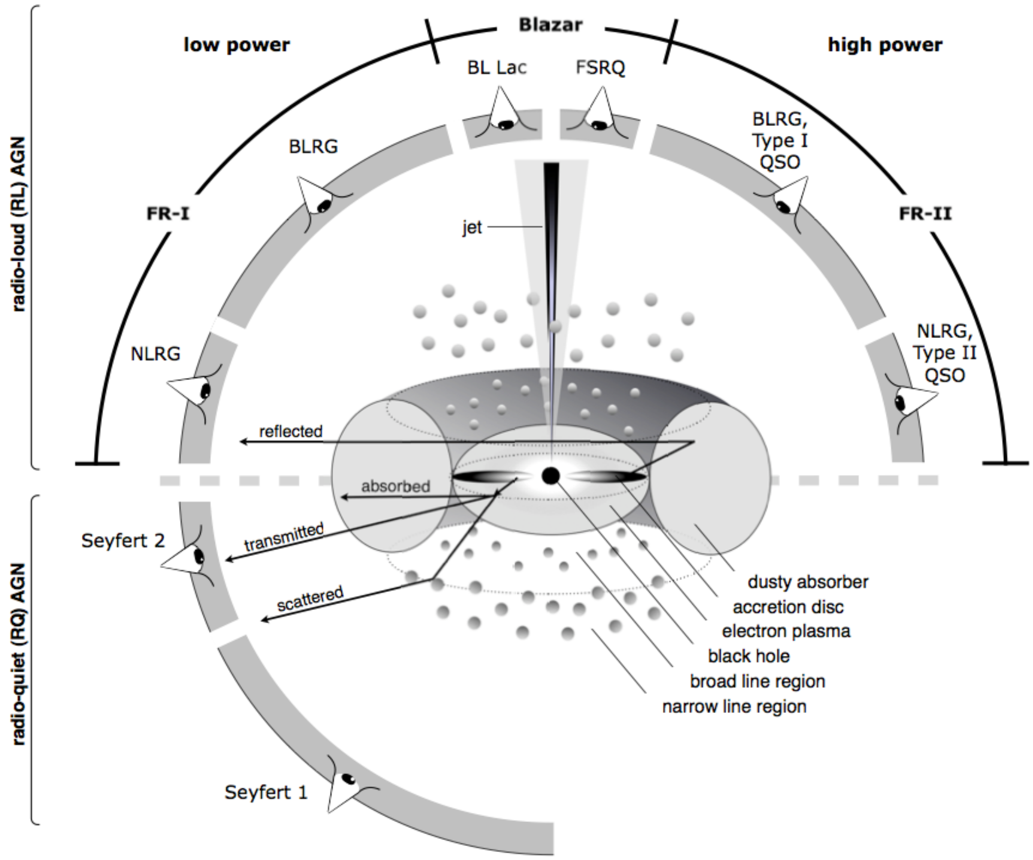
radio-loud (RL) AGN
radio-quiet (RQ) AGN
low power
Blazar
high power
BL Lac
FSRQ
BLRG
BLRG,
Type I
QSO
FR-I
FR-II
jet
NLRG
NLRG,
Type II
QSO
reflected
absorbed
transmitted
scattered
Seyfert 2
Seyfert 1
dusty absorber
accretion disc
electron plasma
black hole
broad line region
narrow line region

Figure 1.2: Schematic representation of the current AGN unification model. The division between radio-loud (upper part) and radio-quiet AGN (lowe part) can be explained by the presence or absence of a powerful jet responsible for most of the radio emission. Obscuring material around the black hole may explain the different emission lines characteristic. Relativistic beaming effect plays also a role in the observed luminosity of radio-loud AGN. Credit: Beckmann, Shrader.

Maximum Entropy Method are two popular method in radio astronomy.

In the early days of radio interferometry, the baseline length was limited to few kilometers. The three-elements One-Mile Telescope completed in 1964 was able to achieve a resolution of 80″ at 408 MHz. An advantage of observations at radio wavelengths in comparison to measurements at shorter wavelengths is that the telescopes output comprising both the amplitude (voltage) and phase of the incoming electromagnetic wave, can be easily transfered from one point to another through cables, and can even be recorded for later processing. This possibility led to the rapid increase of baselines length, and the development of the technique of Very Long Baseline Interferometry (VLBI). By combining telescopes separated by thousands of kilometers, it was possible to reaches angular resolution of smaller than one milliarcsecond of arc. The Very Large Baseline Array (VLBA), a dedicated VLBI instrument operated by the National Radio Astronomy Observatory (NRAO) has been in operation since 1993. It uses ten 25-meter telescopes spanning up to 8000 kilometers across the United States, and it is able to reach a resolution of 0.17 mas at 47 GHz. The European VLBI Network (EVN) operated by the European Consortium for VLBI is able to combine up to 20 individual telescopes spread across the entire globe, including some of the world's largest and most sensitive radio telescopes, making it the most sensitive VLBI array in the world. A good review about the effort and developments that made this instrument a reality can be found in Porcas [2009]. Increasing further the angular resolution requires either longer baselines or observing at higher frequency. Using space-based VLBI antennas such as HALCA [Hirabayashi et al., 1998] and RadioAstron [Kardashev et al., 2013], resolution as high as 10 µas can be reaches. Extending VLBI observations to millimeter and sub-millimeter wavelengths is another approach to achieve ultra hight angular resolution, with up to 50 µas at 3 mm wavelengths (86 GHz) [see Krichbaum et al., 2013, for details].

1.3 Motivation and organization of the work

The high resolution imaging capability offered by radio interferometry is key for our understanding of relativistic jets. Detailed analysis of the jet structure and evolution on sub-parsec to parsec scales can bring unique insights on the mechanisms involved in their formation, collimation and acceleration [Hada et al., 2011; Nakamura and Asada, 2013]. Investigations of jet stability and notably the structural pattern changes caused by Kelvin-Helmholtz instability pave the way to determining the physical parameters governing the flow [Lobanov and Zensus, 2001; Hardee et al., 2005]. Relativistic jets are also a prominent source of high energy emission and hence investigations of jets can serve as a laboratory for high energy plasma physics [Kirk and Duffy, 1999]. Structural variability can be analyzed in connection with high energy flares, thus probing the location and origin of high energy emission [Schinzel et al., 2012].

The task of producing an image from VLBI observations is challenging. Reconstructing an image from visibilities in the Fourier domain is essentially an inverse problem that is ill posed and will not have a unique solution. The combined continued progress in non-linear deconvolution techniques and increased sensitivity of radio telescopes have considerably improved the quality of radio interferometric images. Maps of several prominent relativistic jets shows transversely resolved structure and contain a wealth of morphological and dynamical information. Efficient extraction of this information is of paramount importance for understanding the physics and evolution of these objects. The algorithms and methods currently employed for this purpose (such as Gaussian model fitting) often use simplified approaches to describe the structure of resolved objects. Automated (unsupervised) methods for structure decomposition and tracking of structural patterns are needed for this purpose to be able to treat the complexity of structure and large amounts of data involved. This dissertation is primarily dedicated to development, testing, and application of pioneering methods for automated decomposition and tracking of two-dimensional structural patterns in extragalactic relativistic jets.

The dissertation is divided in five main parts. In Chapter 2, we provide a brief review on our current understanding on jets physics. In Chapter 3, we introduce a new wavelet-based image segmentation and evaluation (WISE) method for multiscale decomposition, segmentation, and tracking of structural patterns in astronomical images. In Chapter 4, WISE is tested against simulated images of relativistic jets. In Chapter 5, the jets in 3C 273, 3C 120 and 3C 111 are analyzed using data from the Monitoring Of Jets in Active galactic nuclei with VLBA Experiments (MOJAVE) program. Finally, in Chapter 6, we will present the results of the kinematic analysis of the innermost part of the M87 jet.

Throughout this thesis, we assume a cosmology with $H_0 = 70\ \mathrm{km\ s^{-1}\ Mpc^{-1}}$, $\Omega_M = 0.3$ and $\Omega_\Lambda = 0.7$

Chapter 2

Jet physics

Presence of astrophysical outflows have been found in diverse objects with remarkably large range of scales, masses, and physical types. The jets produced by active galactic nuclei (AGN) are probably the most powerful of this category. Direct or indirect indication of jets have also been found in microquasars, X-ray binaries, Young Stellar Objects (YSO) and Gamma Ray Bursts (GRB). Despite the large diversity of these objects, they all share two main elements that are critical for the formation of jets: a compact, rotating, and magnetized central engine, and matter accreting towards this central source. Different models have been invoked to explain the formation and propagation of jets. This chapter presents a brief summary of the basic concepts of magnetic outflows that is the most commonly accepted model that explain the observed structure and properties of the different categories of jets.

2.1 Central engine and accretion disk

The first key element common in all extragalactic jets is a compact object. In the case of AGN, this is the Super Massive Black Hole ($\sim 10^6$–$10^9 M_\odot$) , while it could be the white darf, neutron star or smaller black hole in X-ray binary, the collapsing star in GRB events or the protostars in YSO. Strong gravitational forces associated with the central object result in accretion surrounding material onto it, which is typically accompanied by formation of an accretion disk. The creation of an accretion disk provides the energy supply, in the form of kinetic energy of the infailling matter, necessary for the formation of the large scale jet. The configuration of this system is illustrated in Fig. 2.1

A Black Hole (BH) is characterized by its mass m, and its angular momentum J or, equivalently, dimensionless BH spin $a = J/J_{max}$ [Tchekhovskoy, 2015]. An important reference point of the black hole description is the event horizon surface, defined as the boundary in through which matter and light can fall inward towards the black hole but can never re-emerge [Beckmann and Shrader, 2012]. In the case of a non-rotating black hole ($a = 0$), this region occurs at the so-called Schwarzschild

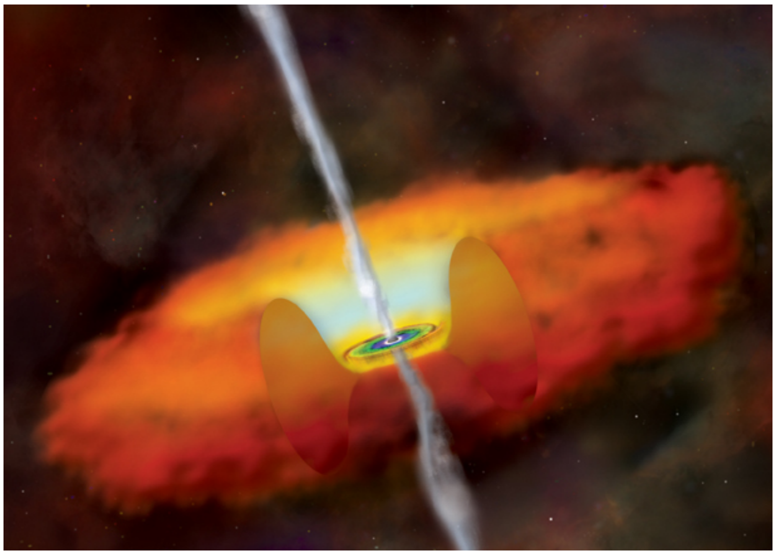

Figure 2.1: Artist view of a black hole surrounded by an accretion disk of hot gas and torus of cooler gas and dust. (Credit: NASA/CXC/M.Weiss).

radius:

$$R_s = \frac{2Gm}{c^2} \tag{2.1}$$

and gravitational field is described in terms of the Schwarzschild metric. In the case of rotating black hole ($0 < a < 1$), the Kerr metric is used, and the event horizon is defined as:

$$R_h = \frac{R_S}{2}(1 + \sqrt{1 - a^2}) \tag{2.2}$$

This basic difference between rotating and non-rotating black hole is actually an important one. The BH spin is an additional source of energy that can be extracted through the so-called Penrose process. Additionally, the spin will define the innermost stable circular orbit (ISCO), which correspond to the accretion disk inner radius. It varies from $r_{\mathrm{ISCO}} = 6R_s$ for a non rotating black hole to $r_{\mathrm{ISCO}} = 1R_s$ for a maximally rotating black hole [Bardeen et al., 1972].

The full detail of the mechanism of accretion onto the central black hole is still not clear. Several models have been invoked to explain the observed accretion properties. The Bondi accretion consider an approximated spherically symmetrical accretion flow. Following Beckmann and Shrader [2012], in this model the black hole will accrete matter at an approximate rate:

$$\dot{M}_B = \pi R_B^2 \rho v \tag{2.3}$$

with ρ and v the accretion wind density and velocity, and R_B the effective capture radius that is approximatively found using the escape velocity of the central engine:

$$R_B = \frac{2Gm}{v^2} \tag{2.4}$$

The actual amount of matter accreted by the central object is then defined in term of Bondi accretion rate $\dot{M}_{acc} = \alpha \dot{M}_B$, with α representing the efficiency of the accretion and is model dependent.

This model allows us to determine the basic physical conditions in the vicinity of an accreting object. However the accretion flow is unlikely to be spherically symmetrical close to the black hole, and we expect more a disk-shaped structure. A model for a thin, viscous disk (or alpha disk) has been first proposed by Shakura and Sunyaev [1973]. Different models of Advection Dominated Accretion Flow (ADAF) have also been invoked to explain the radiative inefficiently of some low luminosity AGN [Narayan et al., 1998].

2.2 Jet launching

In the canonical picture of the disc accretion, the formation of a collimated outflow can be viewed as an inevitable consequence of the accretion. There has to be a loss of momentum in order to have accretion due to momentum conservation law, and the transport of matter above the disk in the form of a wind is an efficient way to extract angular momentum. Analytic modeling and numerical simulation of such systems have found that a condition for the creation of such wind is the presence of a large scale magnetic field. The magnetic field in the vicinity of the black hole can be advected inwards by the accreting matter in the disk [Blandford and Payne, 1982], or alternatively it can be generated locally by a disk dynamo [Tout and Pringle, 1996]. Close to the disk, the field lines are anchored in the disk, and will co-rotate with it.

Considering a cylindrical coordinate system $(z,\, r,\, \phi)$, with z the axis of rotation, and $(r,\, \phi)$ the plane of the disk (see Fig. 2.2), the magnetic field can be decomposed into a poloidal, $\boldsymbol{B}_p = B_r(r,z)\hat{r} + B_z(r,z)\hat{z}$, and toroidal component, $\boldsymbol{B}_\phi = B_\phi(r,z)\hat{\phi}$. The poloidal field will dominate close to the disk, and can be written as [Vlahakis, 2015]:

$$\boldsymbol{B}_p = \frac{1}{r}\nabla\Psi(r,z) \times \hat{\phi} \tag{2.5}$$

with $\Psi(r,z)$ the so-called poloidal magnetic flux function. Field lines are defined as lines of constant flux function on the $(z,\, r)$ plane.

In the standard Blandford & Payne model, the energy source of the wind is the kinetic energy of the rotating disk, with the most powerful component of the jet, accelerated to high bulk Lorentz factor at large distance, being launched in the inner part of the accretion disk, close to the ISCO. In this region we can approximate the rotation to be Kelperian, and the corresponding angular velocity Ω can be written as:

$$\Omega = \sqrt{\frac{mG}{r_0^3}} \tag{2.6}$$

with r_0 the radius in the plane of the accretion disk of the field line, which we can call launching location. In a similar way, the jet can be launched from the magnetosphere

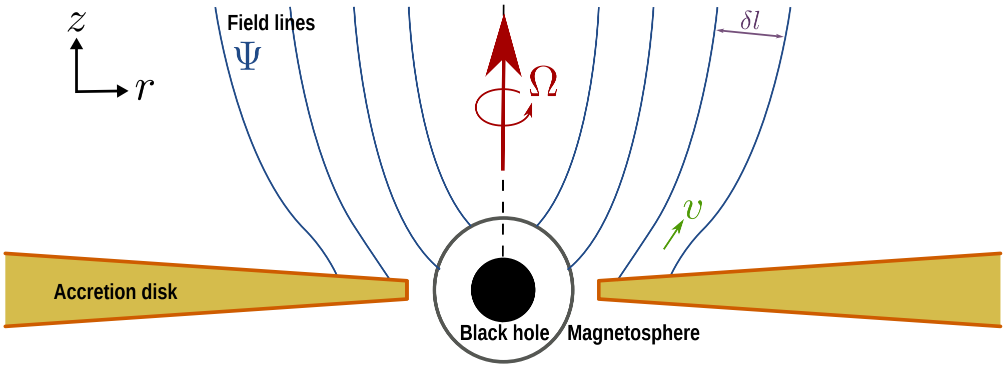

Figure 2.2: Illustration of the field lines configuration near the black hole. Field lines are either anchored in the accretion disk or in the magnetosphere of the rotating black hole. The two important parameters determining the power of the jet are the angular velocity of the central object or accretion disk Ω, and the magnetic flux Ψ. The distance between two field lines δl is an essential parameter of the acceleration and collimation of the jet after the fast magnetosconic point.

of a rotating black hole, extracting the rotational energy of the central engine through the Penrose process. Blandford and Znajek [1977] first demonstrated the viability of this hypothesis and found that the effective angular velocity of the corresponding field line would be:

$$\Omega_F \simeq 0.5\ \Omega_H = 0.5\frac{ac}{2r_H} \tag{2.7}$$

These two mechanisms of energy extraction are illustrated in Fig. 2.2 which shows field lines anchored in both the magnetosphere and the accretion disk. In the first case, the field line angular velocity will be constant $\Omega = \Omega_F$, while in the second case, it will decrease with the distance of the anchored point to the central engine. The field angular velocity define a critical point called the light cylinder radius at $r_{lc} = r/(\Omega c)$.

In the model of magnetic outflows that we are adopting here, a magneto- centrifugal mechanisms initiate the launching and acceleration [Blandford and Payne, 1982]. Magnetic pressure dominates in the low density and gas pressure of the atmosphere of the disk. While the flow co-rotates with the disk, it is unrestricted by the magnetic forced along the field lines [Spruit, 2010]. The flow experiences a centrifugal force accelerating it along them, much as if it were carried in a set of rotating rigid tubes anchored in the disk. At a distance called the Alfvén point (AP), close to the light cylinder in the case of relativistic flow, co-rotation of the field lines and the flow ceases, and the field starts lagging behind, developing a significant toroidal component. This transition can be seen in Fig. 2.3 where the Lorentz factor, velocity and magnetic field of a typical relativistic magnetic flow are plotted along the distance from the central engine. The acceleration by centrifugal forces will also halt at this transition point, and the magnetic pressure of the toroidal magnetic field will drive further acceleration through hoop stress forces up to another critical point, the fast

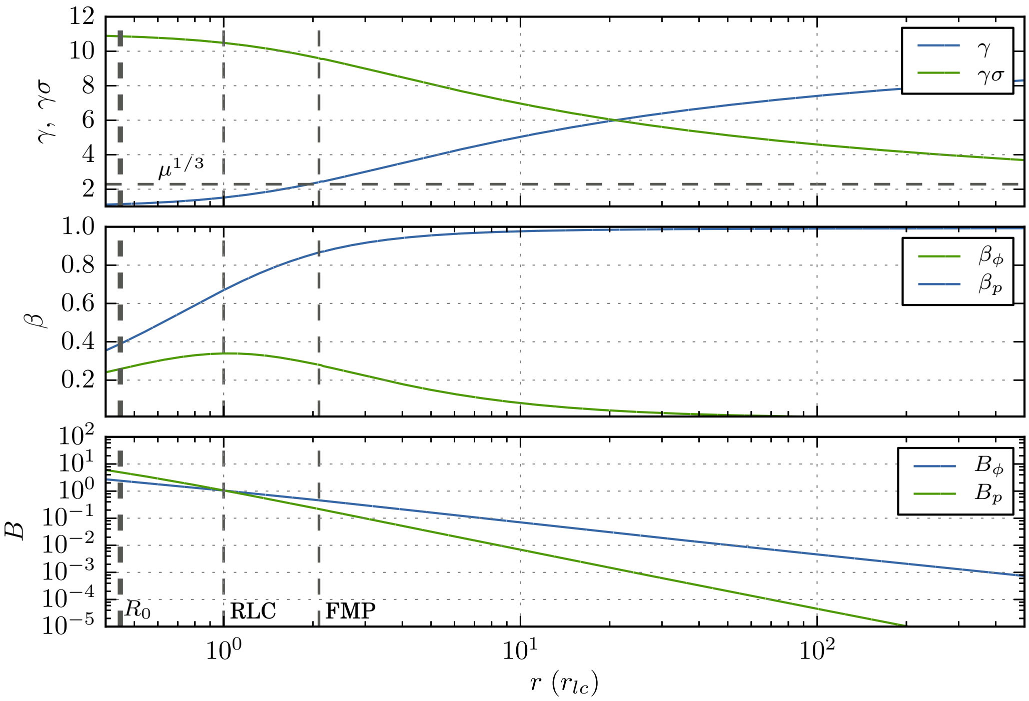

Figure 2.3: Typical example of evolution of a magnetic flow with distance from the central engine. Top panel: the Lorentz factor (blue) increases at the expense of the magnetic energy (green). Equipartition between kinetic and Poynting energy is achieved around $r_{eq} \sim 20 r_{lc}$. Middle panel: The toroidal velocity (green) is maximum at the light cylinder radius and then decrease. Bottom panel: The poloidal magnetic field (green) dominates at the inlet of the flow and decrease like $\sim 1/r^2$, while the toroidal magnetic field (green) decrease like $\sim 1/r$ and start to dominate around the light cylinder. In the three panels, the launching location (R_0), fast magnetosonic point and light cylinder are indicated.

magnetosonic point (FMP).

2.3 Jet acceleration and collimation

The total specific energy (matter + electromagnetic) μ and the angular momentum L are conserved along a field line. In the approximation of cold ideal magnetohydrodynamics MHD flow these can be expressed following Vlahakis [2015]:

$$\mu(\Psi) = \gamma - \frac{r\Omega B_\phi}{c\eta} \tag{2.8}$$

$$L(\Psi) = \gamma r v_\phi - \frac{crB_\phi}{\eta} \tag{2.9}$$

where γ is the bulk Lorentz factor of the flow, v_ϕ is the toroidal component of the velocity and η represents the distribution of mass flux at the inlet of the flow:

$$\eta = \frac{4\pi\gamma\rho_0\beta_p c^2}{B_p} \tag{2.10}$$

The ratio of the magnetic (or Poynting) to kinetic energy flux can be introduced by the magnetization parameter:

$$\sigma = \frac{\mu - \gamma}{\gamma} \tag{2.11}$$

At the inlet, the flow is non-relativistic ($\gamma_{in} \sim 1$) and is therefore Poynting dominated. It has been demonstrated [Vlahakis, 2015] that at the fast magnetosconic point the flow reaches a Lorentz factor $\gamma_f \sim \mu^{1/3}$ (also see Fig. 2.3). In fact, if the field lines were radial the flow would stop accelerating before this point, slowly reaching its maxmimum Lorentz factor $\gamma_{max} \sim \mu^{1/3}$ [Michel, 1969]. The additional acceleration that would explain the observed high Lorentz factor ($\gamma \sim 10$), and kinetic dominated flow [Sikora et al., 2005] strongly depends on the configuration of the field lines, and on their collimation. Li et al. [1992] found that acceleration can continue if the flow expansion is such that the distance between the field lines δl increase faster than the cylindrical distance r (see Fig. 2.2), which constitutes the so-called “magnetic noozle” mechanisms. After the FMP, acceleration and collimation are concurrent, explaining at the same time the observed Lorentz factors and opening angles of parsec scale of AGN jets. This process is slow, and both numerical simulation [Komissarov et al., 2007] and observations have shown that acceleration can indeed continue up to large distances ($z \sim 10^3$–10^4 R_s), achieving equipartition between Poynting and kinetic energy around $z_{eq} \sim 10^3$ R_s.

2.4 Instabilities

Different types of plasma instability can develop in relativistic flows, with Current driven (CD) instability and Kelvin-Helmholtz (K-H) instability being the most commonly expected ones.

The kink mode of the CD instability occurs when the jet have developed a strong toroidal magnetic field [Mizuno et al., 2012]. It is one of the most dangerous instabilities as it will act on the center of mass of the fluid, and is hence able to disrupt the outflow (see Panel C in Fig. 2.4). It might, however, be a necessary process as it is suspected to be one of the mechanisms able to transfer electromagnetic energy into plasma energy. As an MHD instability, it operates mainly in the Poynting dominated part of the jet.

The K-H instability is a consequence of velocity shear in a fluid. In AGN jets, it is expected to grow at the transition layer between the jet and the ambient medium and can be modeled by a pressure perturbation:

$$p_{\text{pert}} = \exp(i(kz + n\phi - wt)) \tag{2.12}$$

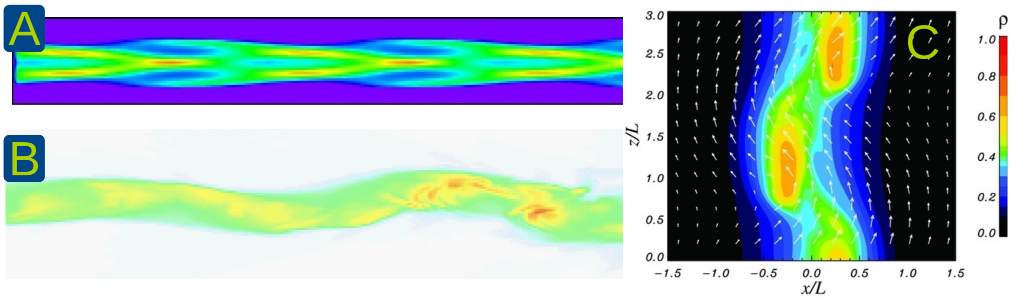

Figure 2.4: Example of instabilities that are known to develop in AGN jets. Simulation of linearly growing elliptical body mode and helical mode of the Kelvin-Helmholtz instability is shown in panel A and B respectively (Credit: P. Hardee). In panel C, we reproduce simulation of the kink mode of the Current Driven instability from Mizuno et al. [2012].

with k and n the longitudinal and azimuthal wavenumber respectively, and w the frequency. K-H instability can be classified by their wavenumber into different modes. The pinch ($n = 0$), helical ($n = 1$), and elliptical ($n = 2$) modes are expected to be most prominent in supersonic, relativistic flows [Lobanov and Zensus, 2001], each having a surface and multiple body mode (see Panel A and B in Fig. 2.4). Contrary to the CD instability, it will operate mainly in the kinetic energy dominated part of the jet.

2.5 Relativistic effects

AGN jets are fast, relativistic flows with high Lorentz factors, which makes a variety of relativistic effects affecting the observed manifestations of the jets. If a source of radiation is moving at a velocity near the speed of light along a direction close to the observer's line of sight, the time interval between the emission of two successive photon as measured in the observer's frame is reduced, and the source appears to move faster than it actually does [Blandford and Konigl, 1979]. If $\beta = v/c$ is the intrinsic speed of the flow, and θ the viewing angle, the apparent velocity β_{app} is obtained using:

$$\beta_{\text{app}} = \frac{\beta \sin(\theta)}{1 - \beta \cos(\theta)} \tag{2.13}$$

Relativistic Doppler effect will also alter the observed radiation of the source. As a consequence of time dilation and aberration of light, the radiation will be concentrated within a cone with an angle of $1/\gamma$ with respect to the flow direction, with γ describing the Lorentz factor of the plasma. The observed intensity will be boosted if observed at a viewing angle θ inside this cone (*i.e.*, $\theta < 1/\gamma$), while it will

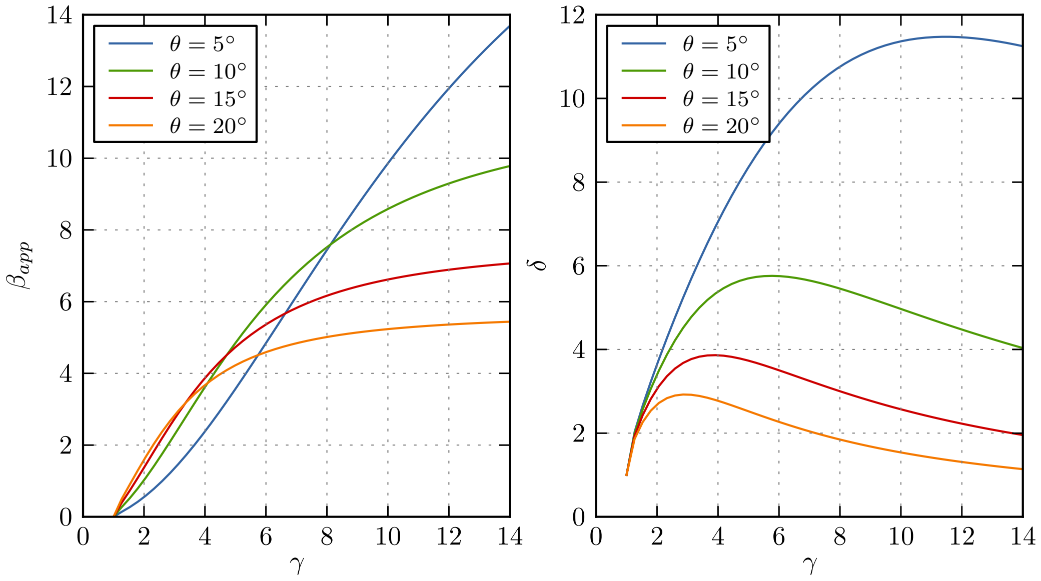

Figure 2.5: Example of relativistic effect with implication on the apparent velocity (left panel) and observed radiation (right panel). The apparent velocity β_{app} and Doppler factor δ is computed for different viewing angle θ and Lorentz factor γ of the flow.

be de-boosted outside this cone. The corresponding Doppler factor δ is:

$$\delta = \frac{1}{\gamma(1 - \beta\cos(\theta))} \tag{2.14}$$

The resulting dependences of the apparent velocity and Doppler boosting on γ and θ are illustrated in Fig. 2.5. Blazars with viewing angles $\theta \sim 5°$ are strongly boosted and can display large super-luminal motions. In misaligned blazars, like the jet in M87 with viewing angle $\theta \sim 20°$, the apparent velocity will be smaller and the jet appearance can also be affected by de-boosting of material with very high Lorentz factors.

Chapter 3

Wavelet-based Image Segmentation and Evaluation

Part of the work presented in this chapter is published in Mertens and Lobanov [2015]

3.1 Introduction

The steady improvements of the dynamic range of astronomical images and the ever-increasing complexity and detail of astrophysical modeling bring a higher demand on automatic (or *unsupervised*) methods for characterizing and analyzing structural patterns in astronomical images.

Several of the approaches developed in the fields of computer vision and remote-sensing to track structural changes [cf. Yuan et al., 1998; Doucet and Gordon, 1999; Arulampalam et al., 2002; Sidenbladh et al., 2004; Doucet and Wang, 2005; Myint et al., 2008] either require oversampling in the temporal domain or rely on multiband (multicolor) information that underlies the changing patterns. This renders them difficult to be used in astronomical applications that typically focus on tracking changes in brightness in a single observing band, which are monitored with sparse sampling, and in which the structural displacements between individual image frames often exceed the dimensions of the instrumental point spread function (PSF).

Astronomical images and high-resolution interferometric images in particular offer very limited (if any) opportunity to identify "ground control points" or to build "scene sets", as employed routinely in remote-sensing and machine-vision applications [cf. Djamdji et al., 1993; Zheng and Chellappa, 1993; Adams and Williams, 2003; Zitová and Flusser, 2003; Paulson et al., 2010]. Structural patterns observed in astronomical images often do not have a defined or even preferred shape, which is an aspect relied upon in a number of the existing object recognition algorithms [e.g., Agarwal et al., 2003]. Astronomical objects normally do not feature sufficiently robust edges that would warrant applying the edge-based detection and classification commonly used in object-recognition methods [Belongie et al., 2002]. In addition, astronomical images often feature partially transparent optically thin structures in which multiple structural patterns can overlap without full obscuration, which makes these images even more difficult to analyze using the algorithms developed for the purposes of remote-sensing and computer vision. Because of these specifics, automated analysis and tracking of structural evolution in astronomical images remains very challenging, and it requires implementing a dedicated approach that can address all of the main specific characteristics of astronomical imaging of evolving structures.

Currently, structural decomposition of astronomical images normally involves simplified supervised techniques based on identification of specific features of the structure [e.g., ridge lines, Hummel et al., 1992; Lobanov et al., 1998; Bach et al., 2008], analysis of image-brightness profiles [cf. Lobanov and Zensus, 2001; Lobanov et al., 2003] , or fitting the observed structure with a set of predefined templates (e.g., two-dimensional Gaussian features [Pearson, 1999; Fomalont, 1999]). Two-dimensional cross-correlation has been attempted only in very few cases [e.g., Biretta et al., 1995; Walker et al., 2008], each time requiring manual segmentation of images, which imposed strong limitations on the number of structural patterns that could be tracked.

In some particular situations, for instance, in images of extragalactic radio jets, distinct structural patterns cover a variety of scales and shapes from marginally resolved brightness enhancements caused by relativistic shocks embedded in the flow [Zensus et al., 1995; Unwin et al., 1997; Lobanov and Zensus, 1999] to thread-like patterns produced by plasma instability [Lobanov, 1998a; Lobanov and Zensus, 2001; Hardee et al., 2005]. In the course of their evolution, most of these patterns may rotate, expand, deform, or even break up into independent substructures. This makes template fitting and correlation analysis particularly challenging, and simultaneous information extraction on multiple scales and flexible classification algorithms are required.

Deconvolution algorithms [cf. Högbom, 1974; Clark, 1980] extended to multiple scales [e.g., Cornwell, 2008] might in principle be able to recover such complex structures. However, comparing structures imaged at different epochs is difficult as a result of the general non-uniqueness of the solutions provided by deconvolution and because of an obvious need to group parts of the solution together to describe structures that are substantially larger than the image PSF.

A more robust approach to automatize identification and tracking of structural patterns in astronomical images can be provided by a generic multiscale method such as wavelet deconvolution or wavelet decomposition [cf. Starck and Murtagh, 2006]. While wavelets are typically applied for image- denoising and compactification, they provide all ingredients necessary to decompose the overall structure in an image into a robust set of statistically significant structural patterns. This chapter explores the wavelet approach and presents a wavelet-based image segmentation and evaluation (WISE) method for structure decomposition and tracking in astronomical images. The method is based on combining wavelet decomposition with watershed segmentation and multiscale cross-correlation algorithms to treat temporal sparsity of astronomical images, multiscale structural patterns, and their large displacements between individual image frames.

The conceptual foundations of the method are outlined in Sect. 3.2. An algorithm for segmented wavelet decomposition (SWD) of structure into a set of statistically significant structural patterns (SSP) is introduced in Sect. 3.3. A multiscale cross-correlation (MCC) algorithm for tracking positional displacements of individual SSP is described in Sect. 3.4. Finally, a stacked cross correlation (SCC) method used to determine velocities components in stratified flow is developed in Sect. 3.5.

3.2 Wavelet-based image structure evaluation (WISE) algorithm

3.2.1 Wavelet transform

The wavelet transform is a time-frequency transformation that decomposes a square-integrable function, $f(x)$, by means of a set of analyzing functions, $\psi_{a,b}(x)$, obtained by shifts and dilations of a spatially localized square-integrable wavelet function $\psi(x)$, so that

$$\psi_{a,b}(x) = \frac{1}{\sqrt{a}}\psi\left(\frac{x-b}{a}\right) \quad (a \neq 0)\,, \tag{3.1}$$

where $a > 0$ is the scale parameter and b is the position parameter. The Morlet-Grossman definition [A. Grossmann, 1984] of the continuous wavelet transform for a one-dimensional function $f(x) \in L^2(R)$, the space of all square-integrable functions, is:

$$W(a,b) = \frac{1}{\sqrt{b}}\int f(x)\psi^{*}_{a,b}\left(\frac{x-b}{a}\right)dx\,. \tag{3.2}$$

Different discrete realisations of the wavelet transform exist [Mallat, 1989; Starck and Murtagh, 2006]. In the analysis presented here, the *à trou* wavelet [Holschneider et al., 1989; Shensa, 1992] is employed. The *à trou* wavelet transform has the advantage of yielding stationary, isotropic, and shift-invariant transformation which is well-suited for astronomical data analysis applications [Starck and Murtagh, 2006]. Different scaling functions can be used with this transform [Unser, 1999]. The choice of the scaling function is guided by the specific properties of the image and the information required to be extracted from the image [Ahuja et al., 2005]. In the following, we have used the *B-spline* scaling function (also called the *triangle function*).

For the purpose of this work, we consider digital astronomical images as sampled data $c_0(k)$ defined as a scalar product (computed at locations k) of a function $f(x)$ (sky brightness distribution, convolved with the instrumental point-spread-function) with a scalar scaling function $\phi(x)$, yielding

$$c_0(k) = \langle f(x), \phi(x-k)\rangle\,. \tag{3.3}$$

This operation corresponds to application of a low pass filter to a continuous function. The scaling function ϕ is chosen to satisfy the dilation equation

$$\frac{1}{2}\phi\left(\frac{1}{2}\right) = \sum_l h(l)\phi(x-l)\,. \tag{3.4}$$

In this expression, h is a discrete low pass filter associated with the scaling function. The smoothed data $c_j(k)$ at position k and a given resolution j, containing information of $f(x)$ on spatial scale $> 2^j$ is given by

$$c_j(k) = \frac{1}{2^j}\left\langle f(x), \phi(\frac{x-k}{2^j}\right\rangle\,, \tag{3.5}$$

which is obtained by computing the convolution

$$c_j(k) = \sum_m h(m)c_{j-1}(k+2^{j-1}l)\,. \tag{3.6}$$

The wavelet coefficients $w_j(k)$ containing information on spatial scales between 2^{j-1} and 2^j are then given by the difference between two consecutive scale resolutions:

$$w_j(k) = c_{j-1}(k) - c_j(k)\,. \tag{3.7}$$

Equations (3.4) and (3.7) gives the expression of the wavelet function for this particular transform:

$$\frac{1}{2}\psi\left(\frac{1}{2}\right) = \phi(x) - \frac{1}{2}\phi\left(\frac{1}{2}\right)\,. \tag{3.8}$$

This expression can be easily extended to a two-dimensional case. Applied to an image, it produces a set $w_j(k,l)$ of resolution-related views of the image which are called *wavelet scales*. The concept of spatial wavelet scale plays a role similar to that of a spatial frequency (cf., Fourier transformation): small scales correspond to high frequency and large scales to low frequency. In Figure 3.1, this relation is illustrated for a one-dimensional case by plotting the relative sensitivity of different wavelet scales to fiducial spatial scales represented through brightness distribution described by a Gaussian profile with the respective full width at half maximum (FWHM).

3.2.2 Conceptual structure of WISE

To characterize the structure and structural evolution of an astronomical object, the imaged object structure needs to be decomposed into a set of significant structural patterns (SSP) that can be successfully tracked across a sequence of images. This is typically done by fitting the structure with predefined templates [such as two-dimensional Gaussians, disks, rings, or other shapes deemed suitable for representing particular structural patterns expected to be present in the imaged region; Fomalont, 1999; Pearson, 1999] and allowing their parameters to vary. It is clear, however, that

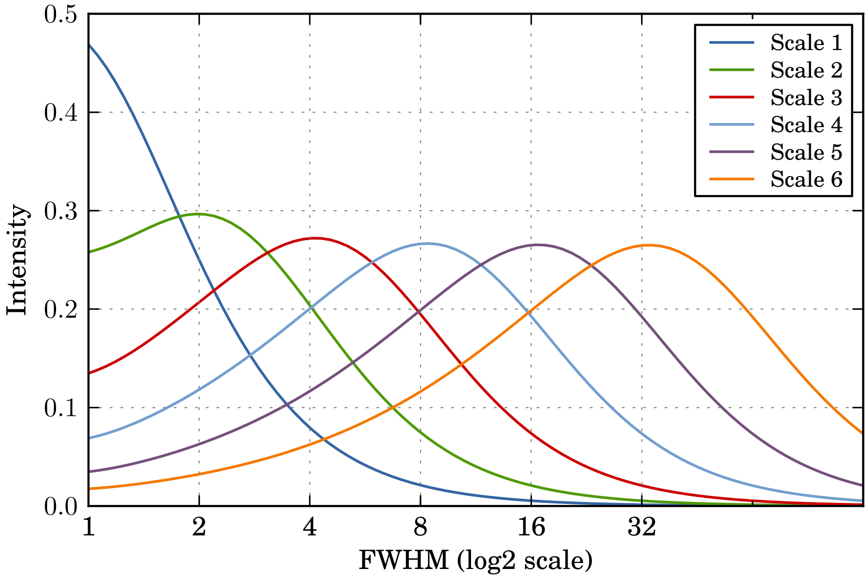

Figure 3.1: Relation between scales of a wavelet transform and spatial scales represented by the FWHM of a Gaussian profile. The individual curves represent the relative sensitivity of a given wavelet scale for recovering a Gaussian feature with a given FWHM. The FWHM for which a wavelet scale is the most sensible, characterized by a peak of intensity, is shown in abscissa. Wavelet transfrom is performed using the triangle scaling function.

for a robust structural decomposition made without a priori assumptions, the generic shape of these patterns must be allowed to vary as well. To ensure this, a method is needed that can automatically identify arbitrarily shaped statistically significant structural patterns, quantify their significance, and provide robust thresholding based on the significance of individual features.

The multiscale decomposition provided by the wavelet transform [Mallat, 1989] makes wavelets exceptionally well-suited to perform such a decomposition, yielding an accurate assessment of the noise variation across the image and warranting a robust representation of the characteristic structural patterns of the image. To further increase the robustness of the method, the multiscale approach is extended here to object detection, similarly to the methodology developed for the multiscale vision model [MVM; Rué and Bijaoui, 1997; Starck and Murtagh, 2006] in related work on object and structure detection [Men'shchikov et al., 2012; Seymour and Widrow, 2002]. By combining these features, we have developed a new, wavelet-based image structure evaluation (WISE) algorithm that is aimed specifically at the structural analysis of semi-transparent, optically thin structures in astronomical images. The method involves segmented wavelet decomposition (SWD) of individual images into arbitrary two-dimensional SSP (or image regions) and subsequent multiscale cross-correlation (MCC) of the resulting sets of SSP. A detailed description of the method is given below.

3.3 Segmented wavelet decomposition

The segmented wavelet decomposition (SWD) comprises the following steps to describe an image structure by a set of SSP:

1. A wavelet transform is performed on an image I by decomposing the image into a set of J sub-bands (scales), w_j, and estimating the residual image noise (variable across the image).
2. At each sub-band, statistically significant wavelet coefficients are extracted from the decomposition by thresholding them against the image noise.
3. The significant coefficients are examined for local maxima, and a subset of the local maxima satisfying composite detection criteria is identified. This subset defines the locations of SSP in the image.
4. Two-dimensional boundaries of the SSP are defined by the watershed segmentation using the feature locations as initial markers.

These steps essentially combine the MVM approach with watershed segmentation [Beucher and Meyer, 1993] and a two-level thresholding for the purpose of yielding a robust SSP identification procedure that would improve the quality of subsequent tracking of SSP that have been cross-identified in a sequence of images of the same object.

The SWD decomposition delivers a set of scale-dependent models (SDM), each containing two-dimensional features identified at the respective scale of the wavelet decomposition. The combination of all SDM provides a structure representation that is sensitive to compact and marginally resolved features as well as to structural patterns much larger than the FWHM of the instrumental PSF in the image. Moreover, individual SSP identified at different wavelet scales are partially independent, which allows for spatial overlaps between them and can be used to improve the robustness and reliability of detecting structural changes by cross-correlating multiple images of the same object.

3.3.1 Determination of significant wavelet coefficients

As has been discussed above, the wavelet transform of a signal produces a set of zero mean coefficient values w_j at each scale j. To extract significant wavelet coefficients and filter out the noise, a threshold, τ_j, is determined by requiring $|w_j| \geq \tau_j$ for the significant coefficients. The determination of τ_j depends on the noise characteristics in the image and a false discovery rate (FDR) ϵ. For the purpose of this work, it is assumed that the image noise is Gaussian. Techniques exists to handle other types of noise, for example using the Anscombe transform for Poisson noise. We refer to Starck and Murtagh [2006] for a complete review of noise treatment in wavelet analysis of images.

The wavelet transform does not change the Gaussian nature of the noise and hence the noise can be characterized at each scale of its wavelet decomposition by a zero mean and a standard deviation σ_j. This property can be used for relating the desired noise threshold τ_j to σ_j by setting $\tau_j = k_{\mathrm{s}}\sigma_j$ and requiring the significant coefficients to satisfy the condition $|w_j(x,y)| \geq k_{\mathrm{s}}\sigma_j$. Choosing $k_{\mathrm{s}} = 3$ gives an FDR $\epsilon = 0.002$. The application of the threshold condition yields a denoised map for each wavelet scale:

$$m_j(x,y) = \begin{cases} w_j(x,y) & \text{if } |w_j(x,y)| >= k\sigma_j \\ 0 & \text{otherwise }. \end{cases} \tag{3.9}$$

In order to determine σ_j from the standard deviation of the noise of the original image σ_{s}, the standard deviations σ_j^e are calculated for each scale of the wavelet decomposition of simulated Gaussian-noise data with $\sigma_{\mathrm{s,sim}} \equiv 1$. We then use the linearity of the wavelet transform to obtain σ_j from the relation $\sigma_j = \sigma_{\mathrm{s}}\sigma_j^e$ [Starck and Murtagh, 1994].

An estimate of σ_s can be obtained using one of the several techniques available for this purpose. If a noise map can be accessed, σ_{s} is provided simply by calculating the standard deviation of the entire map or of the relevant areas in the map. In other situations, k-sigma clipping or Median Absolute Deviation (MAD) estimation [Starck and Murtagh, 2006] can be applied to assess the noise properties in the image and obtain an estimate of σ_{s}.

3.3.2 Localization of significant structural patterns

A maximum filter is used to identify putative positions of SSP at each scale of the wavelet decomposition. The filter comprises applying the morphological operation of dilation with a structuring element of a desired size. The location of a local maxima occurs when the output of this operation is equal to the original data value. This defines a list of local maxima, H_j, at the scale j:

$$H_j = \{(x,y) : \mathrm{dilation}(w_j(x,y)) = w_j(x,y)\}\,. \tag{3.10}$$

The shape and size of the chosen structuring element affect the smallest separation of two detected local maxima. For our specific application, we use a diamond structuring element of a size that matched the scale at which it is applied; with the minimum size of two pixels. Each of the lists H_j is clipped at a specific detection threshold, ρ_j. This is done recalling that for Gaussian noise, the detection level is proportional to σ_j, hence $\rho_j = k_{\mathrm{d}}\sigma_j$ can be set. For successful detection thresholding, the condition $k_{\mathrm{d}} \geq k_{\mathrm{s}}$ must be satisfied (with $k_{\mathrm{d}} = 4$–5 typically providing good thresholds).

The threshold clipping can be applied for defining F_j as a group of significant feature locations:

$$F_j = \{f = (x,y) : (x,y) \in H \wedge |w_j(x,y)| \geq k_{\mathrm{d}}\sigma_j\}\,, \tag{3.11}$$

and these locations can be used for subsequently defining SSP in the image.

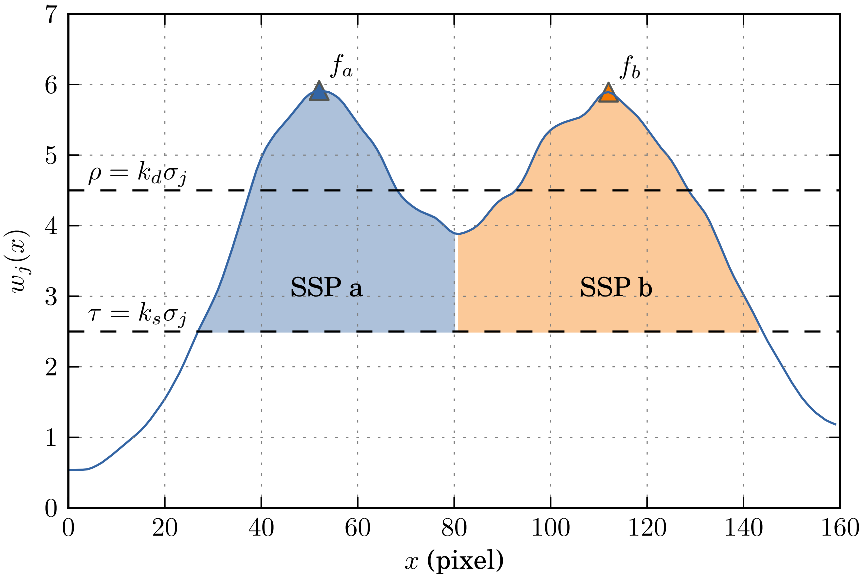

Figure 3.2: Schematic illustration of the method used for SSP localization, applied to a one-dimensional case. The local maxima (triangle marker) are located using the maximum filter and the SSP are associated with each of the local maxima by applying the watershed flooding algorithm. In this example the SSP "a" associated with the position f_a is defined by a region between 25 pix and 82 pix.

3.3.3 Identification of significant structural patterns

An SSP is defined as a 2D region of enhanced intensity extracted at a given wavelet scale. To determine the extent and shape of individual SSP associated with significant local maxima, image segmentation needs to be performed. The segmentation relates each local maximum to a range of surrounding pixels that can be considered part of this local intensity enhancement. The map of significant coefficients, m_j, is used for that purpose. The borders between individual regions are determined from the common minima located between the adjacent regions. This is achieved by watershed flooding [Beucher and Meyer, 1993]. The watershed flooding earns its name from effectively corresponding to placing a "water source" in each local minimum and "flooding" the image relief from each of these "sources" with the same speed. The moment that the floods filling two distinct catchment basins start to merge, a dam is erected to prevent mixing of the floods. The union of all dams constitutes the watershed line. Figure 3.2 illustrates the application of the watershed segmentation in a one-dimensional case.

The watershed segmentation is performed on $-m_j$ at all scales j with F_j as "water sources", or markers. Each local maximum f_a of F_j gives a region $s_{j,a}$ defined as

$$s_{j,a}(x,y) = \begin{cases} m_j(x,y) & \text{if } (x,y) \text{ is inside the} \\ & \text{watershed line of } f_a; \\ 0 & \text{otherwise} \end{cases} . \tag{3.12}$$

The resulting SSP representation of an image at the scale j is finally derived as the group of regions:

$$S_j = \{s_{j,a} : f_a \in F_j\} \, . \tag{3.13}$$

An example of applying the SSP identification is shown in Fig. 3.3 for a simulated image of a compact radio jet.

3.3.4 Uncertainty on the SSP position

A zero order estimate on the uncertainty on the SSP position can be derived following Fomalont [1999]:

$$\sigma_x = \frac{b_x}{\sqrt{2}\ \mathrm{SNR}}, \ \ \sigma_y = \frac{b_y}{\sqrt{2}\ \mathrm{SNR}} \tag{3.14}$$

with b_x and b_y the beam size along the x and y coordinate respectively, assuming an elliptical PSF, which is approximately the case for application to VLBA maps, and SNR the signal to noise ratio of the SSP.

3.4 Multiscale cross-correlation

To detect structural differences between two images of an astronomical object made at epochs t_1 and t_2, one needs to find an optimal set of displacements of the original SSP (described by the groups of SSP $S_{j,1}, j = 1, ..., J$) that would match the SSP in the second image (described by $S_{j,2}$, $j = 1, ..., J$). Cross-correlating $S_{j,1}$ and $S_{j,2}$ is a natural tool for this purpose. There are two specific issues that need to be addressed, however, to ensure that the cross-correlation analysis is reliable. First, a viable rule needs to be introduced to identify the relevant image area across which the cross-correlation is to be applied. The typical choices of using the full image area or manually selecting the relevant fraction of the image [Pushkarev et al., 2012; Fromm et al., 2013] are not satisfactory for this purpose. Second, the probability of false matching needs to be minimized for features with sizes smaller than the typical displacement between the two epochs.

These two requirements can be met by multiscale cross-correlation (MCC), which combines the structural and positional information contained in S_j at all scales of the wavelet decomposition. The MCC uses a coarse-to-fine hierarchical strategy that is well known in image registration. This principle has first been used in Vanderbrug and Rosenfeld [1977] and Witkin et al. [1987], who used Gaussian pyramids. It was then extended to the wavelet transform by Djamdji et al. [1993] and Zheng and Chellappa [1993]. We refer to Zitová and Flusser [2003] and Paulson et al. [2010] for a review on the different techniques developed in this area. However, none of theses algorithms can be directly applied for our purpose. The main reasons for this difficulty are the following:

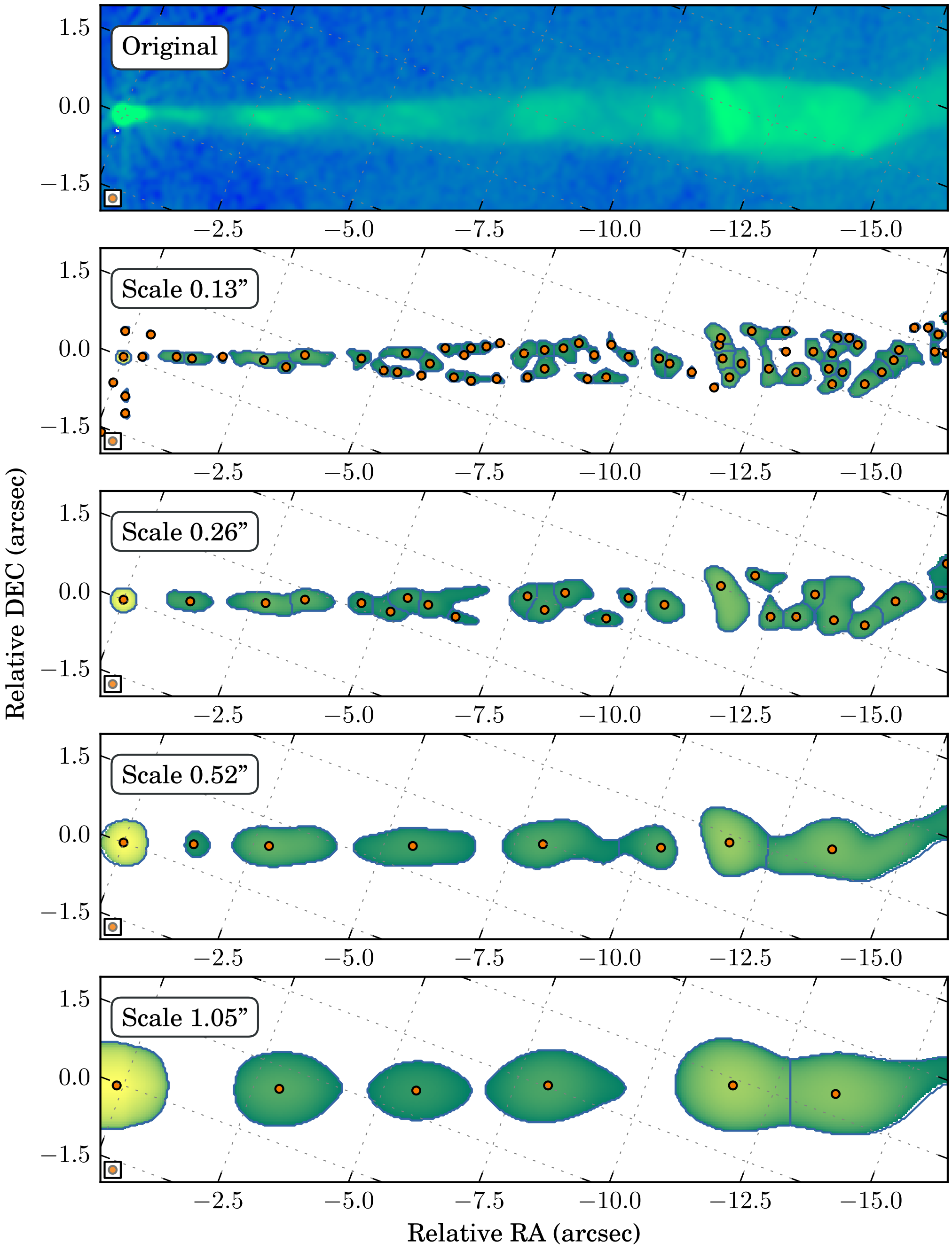

Figure 3.3: Example of the SWD decomposition performed on a radio map of the jet in M87 observed using the VLA telescope. The original image is shown in the top panel (Credit: Biretta & Owen, NRAO). The lower panels show the resulting SWD decomposition obtained at scales of 0.4, 0.8, and 1.6 time the beam size. The different SSP are enclosed in a blue line, while the location of there local maxima is indicated by orange points. The different Knots in the jets are best described at large scale while filaments identified as K-H instability start to be visible at smallest scale.

1. The images we consider are sparsely sampled (with structural displacements on the order of the PSF size or even larger) and do not offer a set of "ground-control points" that facilitate image registration (while this aspect is a critical feature of virtually all of the remote-sensing and computer-vision algorithms).
2. The images are often dominated by optically thin structures (with the possibility of two or more independent structural features projected onto each other and often having different displacement or velocity vectors).
3. The structural patterns do not have a defined or even preferred shape, and their shape may also vary from one image to another.

All these aspects call for a method that differs significantly from the approaches used in the fields of remote sensing and computer vision.

Considering that SSP identified by the SWD at the wavelet scale j have a typical size of 2^j, the largest displacement detectable on the scale j must be smaller than 2^j. Identification of the structural displacements can then begin from choosing J, the largest scale of the wavelet decomposition, such that it exceeds the largest expected displacement, but still satisfies the upper limit on J given by the largest scale containing statistically significant wavelet coefficients. After correlating $S_{J,1}$ with $S_{J,2}$, the respective correlations between $S_{j,1}$ and $S_{j,2}$ on smaller scales are restricted to within the areas covered by $S_{J,1}$ and $S_{J,2}$ in the two images. Alternatively, this approach can also be used iteratively, restricting correlations on a given scale j to within the areas of the correlated features identified at the $j+1$ scale. This algorithm is illustrated in Fig. 3.4. Details of the procedure for relating SSP identified at different scales are discussed in the next section.

3.4.1 Multiscale relations

Multiscale relations between SSP identified at different spatial scales can be derived from the basic region properties. We note again that the sizes of SSP identified at the scale j are on the order of 2^j. Hence, any two individual SSP s_a and s_b of S_j, identified around respective local maxima f_a and f_b, are separated from each other by at least 2^j. This corresponds to the inequality

$$\|f_a - f_b\| \gtrapprox 2^j, \forall f_a, f_b \in F_j, a \neq b\,. \tag{3.15}$$

If one determines a displacement $\Delta_{j+1,b}$ of the SSP $s_{j+1,b}$ at the scale $j+1$ between two epochs t_1 and t_2, the following relation can be applied for the features of F_j that are inside $s_{j+1,b}$:

$$\Delta_{j,a} = \Delta^{j+1}_{j,a} + \delta_{j,a}\,, \tag{3.16}$$

for all $f_a \in F_j$ and $f_b \in F_{j+1}$, so that $s_{j+1,b}(f_a) > 0$ and the condition $\Delta^{j+1}_{j,a} = \Delta_{j+1,b}$ is satisfied. From Eqs. (3.15) and (3.16), it also follows that

$$\|\delta_{j,a}\| < \frac{2^{j+1}}{2}\,. \tag{3.17}$$

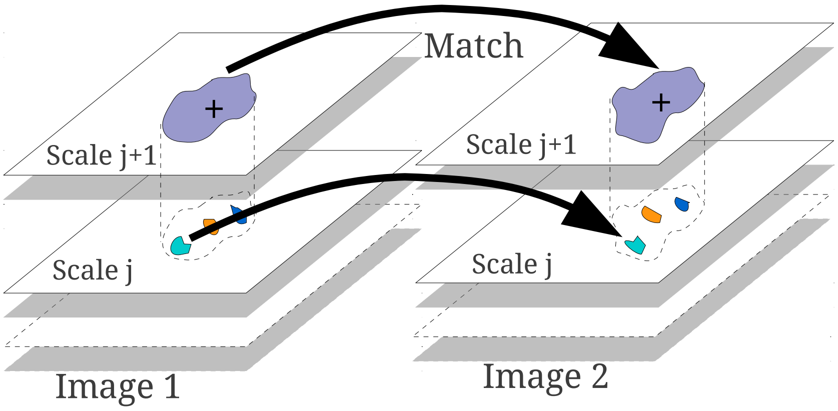

Figure 3.4: Illustration of the feature-matching method using a coarse-to-fine strategy. The calculated displacement at a higher (larger) scale is used to constrain the determination of the feature displacements at a lower (smaller) scale. In this particular example, the displacement of the SSP at scale $j+1$ is used as initial guess for displacements of its child SSPs at scale j. The initial guesses are subsequently refined by cross correlation.

Based on these relations, we introduce the following MCC algorithm to detect structural changes between two images of an astronomical object:

1. The largest scale J of a wavelet decomposition is chosen such that either the largest expected displacement is smaller than 2^J or J corresponds to the largest scale with statistically significant wavelet coefficients.

2. Displacements of SSP features are determined at the largest scale J. For this calculation, all $\Delta_{J,a}^{J+1}$ are set to zero, and $\Delta_{J,a} = \delta_{J,a}$ is calculated for each SSP.

3. At each subsequent scale j ($j < J$), $\Delta_{j,a}^{j+1}$ is determined first by adopting the displacement $\Delta_{J,a}$ measured at the $j+1$ scale for the SSP in which the given j-scale region $s_{j,a}$ falls. Then the total displacement for this SSP is given by $\Delta_{j,a} = \Delta_{j,a}^{j+1} + \delta_{j,a}$.

In this algorithm, the only quantity that needs to be calculated at each scale is the relative displacement $\delta_{j,a}$. This quantity is bound by Eq. (3.17) and, within this bound, it can be determined reliably from the cross-correlation.

3.4.2 Correlation criteria for MCC

The correlation is calculated between a reference image r and a target image t, with the time order of the two images not playing any role. The correlation coefficients can be estimated using a number of different correlation criteria (see Giachetti [2000] for a review). The most commonly used criteria are the cross correlation,

$$C_{\mathrm{CC}}(r,t) = \sum r_i t_i \,, \tag{3.18}$$

and the sum of squared differences,

$$C_{\mathrm{SSD}}(r,t) = \sum (t_i - r_i)^2 \,, \tag{3.19}$$

with i the pixel index. The tolerance to an offset between the reference and the target image is obtained by subtracting the mean value from the image intensity (zero-mean correlation). Similarly, tolerance to scale change is obtained by dividing it by its root-mean-square (normalized correlation).

The MCC algorithm is required to be not sensitive to both the image offset and scale change. The zero-mean normalized cross correlation (ZNCC) and zero-mean normalized sum of the squared difference (ZNSSD) can be applied for this purpose. Pan et al. [2010] have demonstrated that these two criteria are equivalent. MCC uses the ZNCC method, based on its excellent computational performance [Lewis, 1995]. The ZNCC is given by

$$C_{\mathrm{ZNCC}}(r,t) = \frac{\sum \overline{r_i}\,\overline{t_i}}{\sqrt{\sum \overline{r_i}^2 \sum \overline{t_i}^2}} \,, \tag{3.20}$$

with $\overline{r_i} = r_i - \overline{r}$, and $\overline{r}$ being the mean of r. This criterion reaches its highest unity value when the reference and target image are identical.

To detect structural changes between the reference and target images, each single SSP $s_{j,a}$ of the reference image is cross correlated with the target image. As every SSP is constrained to be located within a specific region, one is actually only interested in determining the correlation over that region. To achieve this, a weighting function, ω is introduced, which is normalized to unity and provides $\omega \equiv 0$ everywhere except inside the region containing the SSP of interest. A weighted zero-mean normalized cross correlation (WZNCC) can then be defined as

$$C_{\mathrm{WZNCC}}(r,t) = \frac{\sum \overline{r_i\omega_i}\,\overline{t_i\omega_i}}{\sqrt{\sum \overline{r_i\omega_i}^2 \sum \overline{t_i\omega_i}^2}} \,. \tag{3.21}$$

3.4.3 Detection of SSP displacements

As shown in Sect. 3.4.1, the displacements of individual features are determined starting from the largest scale and progressing to the smallest scale of the wavelet decomposition. For each SSP at the scale j, an initial guess for its displacement is provided by the displacement measured for the region at the scale $j+1$, which includes the SSP in question. The initial guess is then refined via the cross correlation.

This simple procedure is complicated by the fact that individual SSP may merge, split, or overlap as a result of structural changes occurring between the two observations. This means that the displacement for which the cross correlation is maximized does not necessarily provide the correct solution. Such a situation in exemplified in Fig. 3.5. In this example, SSP b is moving faster than SSP a. As a consequence, cross correlating the SSP b at the epoch t_1 with w_{j,t_2} yields the global maximum at $x_a^{t_2}$ and a local maximum at $x_b^{t_2}$. The formal cross-correlation solution will be incorrect in this case. To avoid such errors (or at least to reduce their probability), it is necessary to cross-identify groups of close SSP that can be related (*i.e.*, causally connected) to each other in the two images. The cross correlation can then be applied to these groups as well as to their individual members, so that a set of possible solutions is found for all SSP, and the final solution is determined through a minimization analysis applied to the entire group of SSP.

At the first step of this procedure, subsets of features G_j are defined that are considered to be interrelated. As was discussed in Sect. 3.4, at the scale j, f_a is independent from f_b if $\|f_a - f_b\| > 2^{j+1}$. Then,

$$G_{j,u} = \{x_i, x_i \in F_j \wedge \forall x_l \in F_j \setminus G_{j,u}, \|x_i - x_l\| \geq 2^{j+1}\}\,, \tag{3.22}$$

with

$$F_j = \sum_u G_{j,u}\,. \tag{3.23}$$

At the second step, cross correlation is applied, yielding several possible displacement vectors for each feature of such a group. Considering the multiscale relations described in Sect. 3.4.1, the correlation coefficients at $\delta = (\delta x, \delta y)$ can be calculated for a given feature f_a of a group $G_{j,u}$:

$$\begin{aligned}\gamma_{j,a}(\delta x, \delta y) = C_{\mathrm{WZNCC}}(&s_{j,a}(x + \Delta x_{j,a}^{j+1} + \delta x, y + \Delta y_{j,a}^{j+1} + \delta y),\\ &w_j^{t_2}(x,y))\,,\end{aligned} \tag{3.24}$$

with $\|\delta\| < 2^j$.

As illustrated by the example shown in Fig. 3.5, for complex and strongly evolving structures, it is possible that formally the best cross-correlation solution provided by the largest $\gamma_{j,a,\max}$ may be spurious. Hence, to avoid such spurious estimates of the displacement vectors, all local maxima of $\gamma_{j,a}$ that are above a certain threshold κ (with κ usually set ≥ 0.8) may be considered as possibly relevant solutions. These local maxima are found using the maximum filter method described in Sect. 3.3.2.

After identifying all relevant local maxima, the WZNCC of the group of features is calculated for each possible group solution, and we select the combination of individual displacement δ that maximizes the group correlation. This operation is repeated for all groups of features $G_{j,u}$. This approach provides a robust estimate of the statistically significant structural displacement vectors across the entire image and at each structural scale.

In summary, our cross-correlation procedure comprised the following main steps:

1. Individual initial displacements and bounds are determined for each SSP using the relations of Eqs. (3.16) and (3.17).
2. Groups of causally connected features are defined.

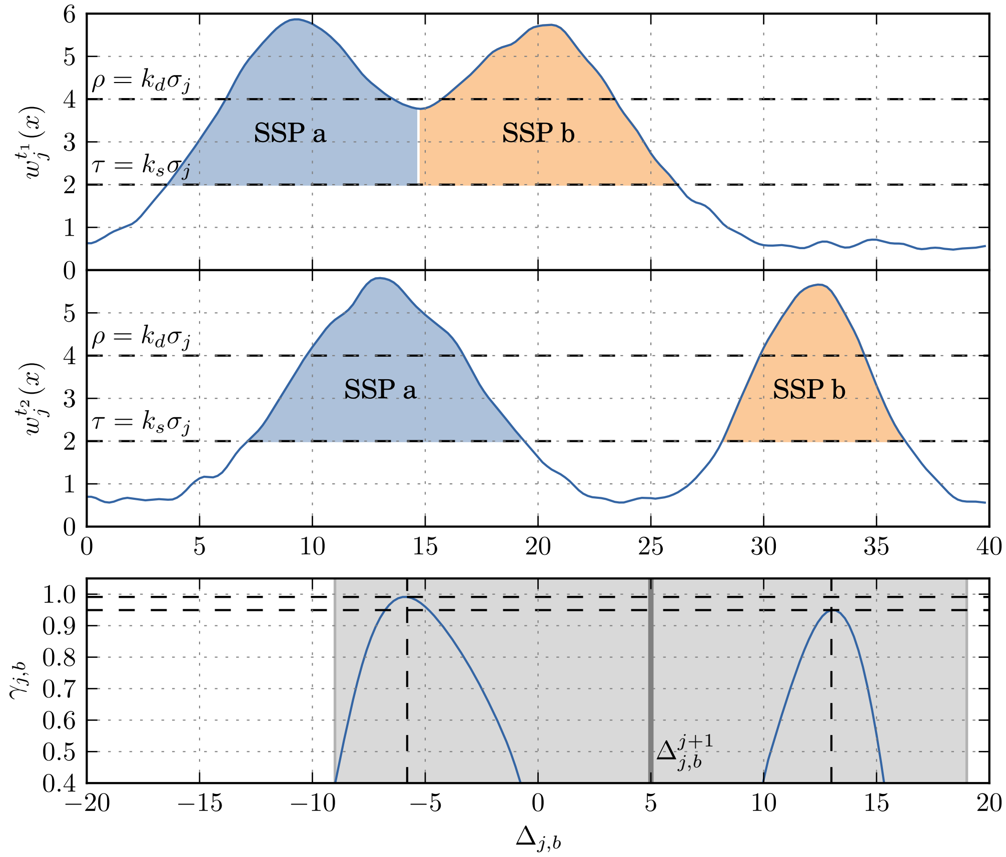

Figure 3.5: Schematic illustration of the detection method used for displacement measurements in a one-dimensional case. In the upper two panels the wavelet decomposition at a scale j of the reference (top panel) and target image is plotted, with two detected SSP marked with colors and letters. The x-axis of each panel is given in pixels. The result of WZNCC between SSP b and the target image is plotted below in the third panel. Two potential displacements are identified within the bounds (gray area) defined by Eq. (3.17) and the initial displacement guess $\Delta_{j,b}^{j+1}$ obtained from analysis at scale $j+1$. To select the correct one and to reduce the chance for erroneous cross-correlation, the group motion of causally connected SSP (in this case SSP a and SSP b) is also included in the cross-correlation analysis, which results in the identification of the displacement $\Delta_{j,b} = 12$.

3. Cross-correlation analysis is performed using the WZNCC for the groups and each of their elements, resulting in a set of potential displacements.

4. The final SSP displacements are determined by selecting a combination of individual displacements that maximizes the overall group correlation.

3.4.4 Overlapping multiple displacement vectors

In images of optically thin structures, several physically disconnected regions with different sizes and velocities may overlap, causing additional difficulties for a reliable determination of structural displacements (observations of transversely stratified jets would be one particular example of such a situation). Using the partial independence of SSP identified by the SWD recovered at different wavelet scales, the MCC method can partially recover these overlapping displacement components. The largest detectable displacement inside a region is determined by the largest wavelet scale j for which this region can be described by at least two SSP. Then, as described in Sect. 3.4.1, the largest detectable displacement would be 2^j. If velocity gradients or multiple velocity components are expected inside this region, then this might not be sufficient and the analysis might have to be started again at a wavelet scale that describes the desired region by three or four different SSP.

The multiscale relations described in Sect. 3.4.1 rely on the assumption that SSP detected at a scale j move, on average, like their parent SSP detected at scale $j + 1$. This assumption sets limits for detecting different speeds at different scales. Between the two scales $j + 1$ and j, this limit, determined by Eq. (3.16), is approximately 2^j. As the velocity difference approaches this limit, matching becomes more difficult. If a very strong stratification or distinctly different overlapping velocity components are expected, it is possible to relax this constraint by introducing a tolerance factor k_{tol} in Eq. (3.17),

$$\|\delta_{j,a}\| < k_{\mathrm{tol}} * 2^j \,. \tag{3.25}$$

This modification may increase the formal probability of spurious matches, but the overall negative effect of introducing the tolerance factor will be largely moderated by the cross-correlation part of the algorithm. A similar limit applies if the gradient of velocity inside an SSP is similar to the SSP size.

3.4.5 Intermediate-scales wavelet decomposition

The ability of the MCC procedure to cross identify SSP in pair of images relies on the smooth transition between scale $j + 1$ and scale j. To improve cross identification, one can construct a scaling function for which the wavelet decomposition will cover intermediate scales. The coefficients w_j at scale j of the wavelet decomposition contains information on spacial scales between 2^{j-1} and 2^j. At scale j, the coefficients of an intermediate-scale wavelet decomposition (IWD) would contains information

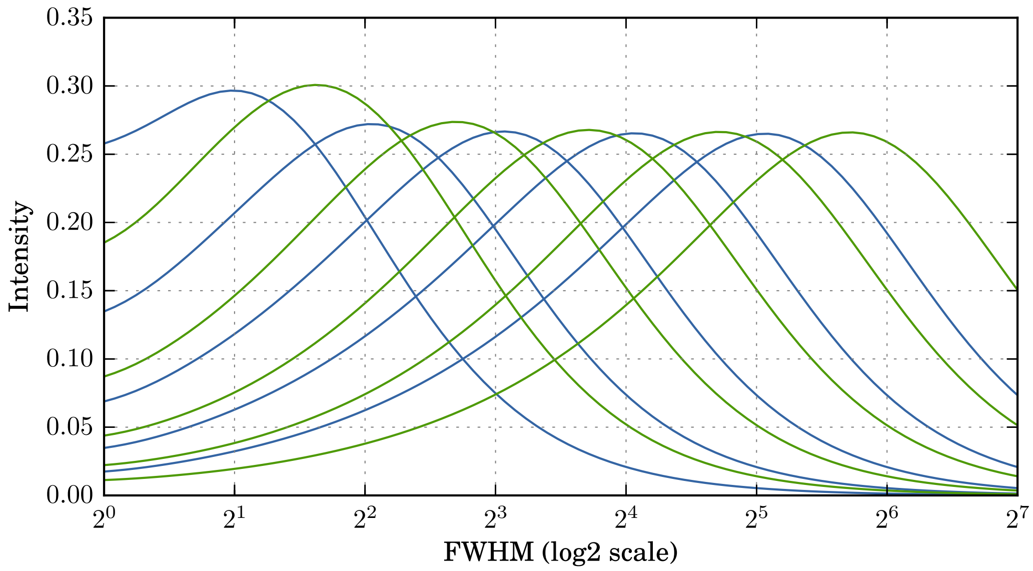

Figure 3.6: Similar to Fig. 3.1 with a triangle scaling function (blue) and a triangle2 scaling function (green). This demonstrate the ability of the triangle2 function to be used as an intermediate-scales wavelet decomposition.

on spacial scales between $1.5 \times 2^{j-1}$ and 1.5×2^{j}. The MCC would then be performed inserting scale j of the IWD in between scale j and scale $j+1$ of the SWD.

The discrete low pass filter associated with the triangle scaling function is:

$$\begin{pmatrix} 1/4 & 1/2 & 1/4 \end{pmatrix} \tag{3.26}$$

We can construct a triangle2 scaling function that can be used for the corresponding IWD. It's discrete low pass filter is:

$$\begin{pmatrix} 1/16 & 1/4 & 3/8 & 1/4 & 1/16 \end{pmatrix} \tag{3.27}$$

This is illustrated in Fig. 3.6 which, similarly to Fig 3.1, describe the sensibility of a wavelet scale to fiducial spacial scales in the images for the scaling functions triangle and triangle2.

3.5 Stacked cross correlation

In Sect. 3.4.4, we have seen that WISE is able to discriminate overlapping features having different velocities. The problem is however challenging, and in the presence of strong stratification or image of poor signal to noise, the cross identification of SSP might fail. We will introduce now an alternative method to the identification of overlapping velocity components that make use of the WISE decomposition.

As shown in Sect. 3.4.3, the displacement of a single SSP can be inferred by the location of the maximum of the cross correlation between two epochs. In the presence of stratification and more complex structure, the resulting cross correlation map contains several peaks corresponding to several potential displacements (e.g. Fig. 3.5). The MCC procedure resolves this issue taking into account the motion found at different scales of the wavelet decomposition and the group motion of causally connected SSP. Another approach is possible if the stratification is homogeneous over an extended region (e.g. two flows with different but constant velocities) and/or if several observations of a same steady stratified flow is available. In this case, one is looking after two or more main velocity components corresponding to different layers of the flow and the cross correlation response of several SSP may be joined or stacked.

The cross correlation $\gamma_{j,a}$ of an SSP a measured at a scale j between epochs t_1 and t_2 is given by Eq. 3.24. In order to reduce the impact of the noise, we only consider here prominent peaks p above a threshold κ (typically taken to 0.6) and model them as two dimensional Gaussian shape $f(p)$ with width corresponding to the error on the displacement:

$$\tilde{\gamma}_{j,a} = \sum_{p} f(p) \tag{3.28}$$

The stack cross correlation of a set of SSP from different scales and epochs is then:

$$\mathrm{SCC} = \frac{\sum_t \sum_j \sum_a \tilde{\gamma}_{j,a}}{N_{SSP}} \tag{3.29}$$

with N_{SSP} the total number of SSP. If several set of epochs with inhomogeneous time interval are stacked together, an additional transformation from displacement to velocity need to be done. This result into a 2D map with peaks corresponding to the main displacement/velocity components.

3.5.1 Significance of velocity components

It is critical to determine the significance of individual maxima found by the stacked cross correlation. Here again, strong stratification and insufficient number of SSP stacked together can lead to spurious detection of velocity components. In the case where several set of epochs are joined together, we can use bootstrapping to determine the probability for a certain correlation coefficient to be resulting from an inadequate sampling. The bootstrapping consists on computing test stacked cross correlation (SCC) for a large number of (typically 1000) trials with the set of epochs randomly shuffled. Confidence interval (CI) for each velocity components can then be calculated from the mean and standard deviation of the test SCC. For the velocities corresponding to small displacements (typically, below 1/2 the beam size), the mean coefficient of the shuffled sets will be overestimated and corrected CI need to be computed for this case adding a small shift (1/5 the beam size) to the images.

3.5.2 Uncertainty on the velocity components

An estimate of the uncertainty of significant velocity component can be obtained from Monte Carlo simulation. A large number of test SCC is again computed this time with all the SSP randomly shifted by an amount derived from a normal distribution, with its standard deviation taken as the uncertainty on the SSP location (see sect. 3.14). The position of a velocity component identified in the formal SCC will be shifted in the test SCC, and the standard deviation of this shift correspond to the uncertainty on the velocity component. It should be noted that for this measure to be valid, the shifts themselves must constitute a Gaussian distribution with the mean corresponding to the velocity component of the formal SCC.

3.5.3 Summary

In this chapter we have introduced a new analysis framework, WISE, which has the potential to significantly leverage the information contains in astronomical images. The method combines automatic segmented wavelet decomposition with a multiscale cross-correlation algorithm, which enables reliable identification and tracking of statistically significant structural patterns. The WISE algorithm comprises three main constituent parts::

- The segmented wavelet decomposition (SWD) is the key component of WISE. It provides a a structure representation, sensitive to compact and marginally resolved features as well as to large scale structural patterns, in form of a set of structural significant patterns (SSP).
- The multiscale cross correlation (MCC) algorithm is dedicated at recovering structural evolution. It combines structural information on different scales of the wavelet decomposition to provides a robust and reliable identification of related SSP in multi-epoch images.
- A stacked cross correlation (SCC) is introduced to recover multiple velocity components from partially overlapping emitting regions. While MCC is able to partially recover overlapping displacement components, the SCC is a statistical approach providing robust identification of multiple velocity components providing an estimate on the significance and the uncertainty for each velocity component.

In Chapter 4 we will characterize the robustness and fidelity of WISE using simulated images of jets. Application on astronomical images will also be presented in Chapter 5. Further discussion on the performance of WISE will also be presented at this stage.

Chapter 4

Testing the WISE algorithm

Part of the work presented in this chapter is published in Mertens and Lobanov [2015]

4.1 Introduction

To evaluate the performance of WISE, two sets of tests were performed. The first set consisted of testing the SWD algorithm for sensitivity to features at low SNR (*sensitivity test*) and for distinguishing close and overlapping patterns (*separation test*). At the second stage of testing, the full WISE algorithm (combining the SWD and the MCC parts) was applied to evaluate the sensitivity of the method of detecting spatial displacements of individual patterns (*displacement test*). Finally the stacked cross correlation is also tested for the detection of the main velocity components in a stratified flow.

For the application of the WISE algorithm, simulated images of optically thin relativistic jets were prepared that contained divergent and overlapping velocity vectors manifested by structural displacements generated for a range of spatial scales.

In the following discussion, we define the SNR of a feature as its peak intensity over the noise level in the image.

4.2 Jet simulation

The simulated jet had an overall quasi-conical morphology, with a bright and compact narrow end ("base" of the jet) and smooth underlying flow pervaded by regions of enhanced brightness (often called "jet components") moving with velocities that varied in magnitude and direction. The underlying flow was simulated by a Gaussian cylinder with FWHM w_{jet} evolving with the following relation:

$$w_{\mathrm{jet}}(z) = r_0 \frac{z}{z_0 + z} + r_1 \frac{z}{z_1} \tan(\phi_0)\,, \tag{4.1}$$

where r_0 is the width at the base of the jet, z_0 the axial z-coordinate of the jet base, and z_1 the z-coordinate of the point after which $w(z)$ increase linearly with an

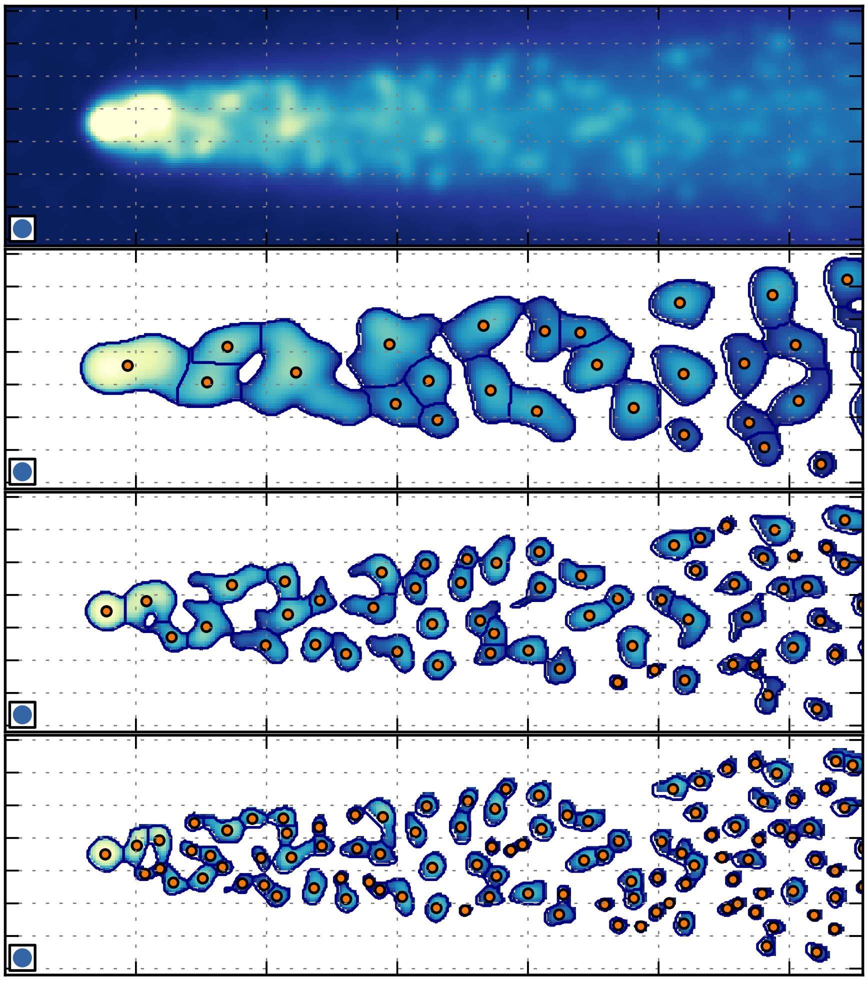

Figure 4.1: Top panel shows a map of a simulated radio jet as described in Sect. 4.2. The lower panels show the resulting SWD decomposition obtained at scales of 1.6, 0.8, and 0.4 beam size.

opening angle of ϕ_0, and intensity i_{jet} evolving with the relation:

$$i_{\text{jet}}(z) = i_0 \left(\frac{z}{z_0} \right)^{\alpha}, \tag{4.2}$$

where α is the damping factor.

The jet base was modeled by a Gaussian component located on the jet axis, at the position z_0. The moving features, also modeled by Gaussian components (with randomly distributed parameters), were added in the area defined by the jet after z_1. The resulting image was finally convolved with a circular or elliptical PSF to study the effect of different instrumental PSFs on the WISE reconstruction of the simulated structural displacements. An example of a simulated jet image together with the SSP detected with the SWD at three different scales is shown in Fig. 4.1.

4.3 Sensitivity test

This test was designed to represent as closely as possible the generic use of the SWD algorithm for detecting and classifying structural patterns in astronomical images. The test was performed on a simulated image of a jet, as illustrated in Sect. 4.2. For this particular simulation a circular PSF with a FWHM of 10 pixels was applied. The morphology of the underlying jet was given by the initial width $r_0 = 5\,\mathrm{FWHM}$ and an opening angle of 8°.

Superimposed on the smooth underlying jet background, Gaussian features with different sizes and intensities were then added. The features were separated widely enough from each other to avoid overlapping. The SWD method was applied to the simulated image, and the SWD detections were then compared to the positions, sizes, and intensities of the simulated features. For the purpose of comparison, we also performed a simple direct detection (DD), which consist of detecting local maxima that are above a certain threshold directly on the image. Similarly as for the SWD detection, the threshold for the DD method was set to $k_\mathrm{d}\sigma_\mathrm{n}$, where k_d is the detection coefficient as defined in Sect. 3.3.2, and σ_n the standard deviation of the noise in the image. When we determined whether a detected feature corresponded to a simulated one, we used a tolerance of 0.2 FWHM of the beam size on the position.

The resulting fractional detection rates are shown in Fig. 4.2 for simulated features of three different sizes and are simuarized in table 4.1. One can see that the SWD method successfully recovers 95% of extended features at SNR $\gtrsim 6$, which makes it a reliable tool for detecting the statistically significant structures in astronomical images. In this particular test the SWD method outperform the DD method by a factor of approximatively 4. As shown in Table 4.1, the detection limit is a function of the detection threshold k_d.

Table 4.1: Performance of the SWD detection compared to a direct detection (DD) in terms of SNR at which at 95% of the simulated features are detected. Results are obtained for features with sizes of 0.2, 0.5, and 1 FWHM of the beam and for different detection threshold factors k_d. The bottom row of the table shows the mean false-detection rate (FDR) found in each test.

Feature size	SNR at 95% detection rate			
[FWHM]	SWD detection			DD
	$k_\mathrm{d} = 5$	$k_\mathrm{d} = 4$	$k_\mathrm{d} = 3$	$k_\mathrm{d} = 4$
0.2	5.1	4.4	3.4	27.6
0.5	5.7	4.8	4.6	29.4
1	8.0	6.6	5.9	36.0
FDR	0	0.01	0.1	0.03

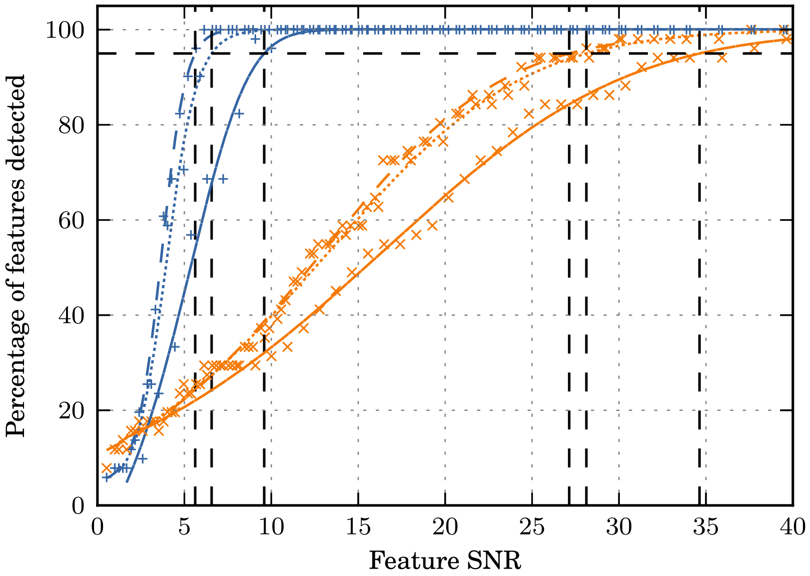

Figure 4.2: Fractional detection rates of the SWD method (blue lines) in comparison with the direct detection (DD, yellow lines). width: 0.2 (dashed line), 0.5 (dotted line) and 1 (plain line) time the FWHMs of the beam. Limits above which at least 95 % of features are detected are 5.6, 6.6, 9.6 for the SWD method and 27.1, 28.1 and 34.6 for the DD method. The number of false detection at the above limit is 3% for the DD, while it stay null in the case of SWD.

4.4 Separation tests

The separation tests were designed to characterize the ability of the SWD method to distinguish two close features. In this test, the images structure comprised two Gaussian components of finite size that were partially overlapping. The two components were defined by their respective SNR, S_1 and S_2 and FWHM, w_1 and w_2, and they were separated by a distance Δ_s. For the purpose of quantifying the test results, the fractional component separation $r_s = 2\Delta_s/(w_1 + w_2)$ was introduced. The tests determined the smallest r_s for various combinations of the component parameters at which the two features are detected. The performance of the SWD algorithm was again compared with results from applying the DD method introduced in Sect. 4.3.

In the first separation test, the ratio $\kappa_w = w_1/w_2$ was varied while setting the SNR of the two features $S_1 = S_2 = 20$. Note that the features partially overlapped at their half-maximum level for $r_s \leq \kappa_w/(1 + \kappa_w)$. The results of this test are shown in Fig. 4.3, with SWD always performing better than the DD. In addition to this, the evolution of smallest detectable r_s with κ_w indicates two different regimes for SWD. For $1 \leq \kappa_w < 2$, SWD progressively outperforms DD, with the difference between the two increasing as κ_w increases. At $\kappa_w \geq 2$, SWD undergoes a fundamental transition, with both features ultimately being always detected (at the 2-pixel separation limit). This is the result of the multiscale capability of the SWD to identify and separate power concentrated on physically different scales.

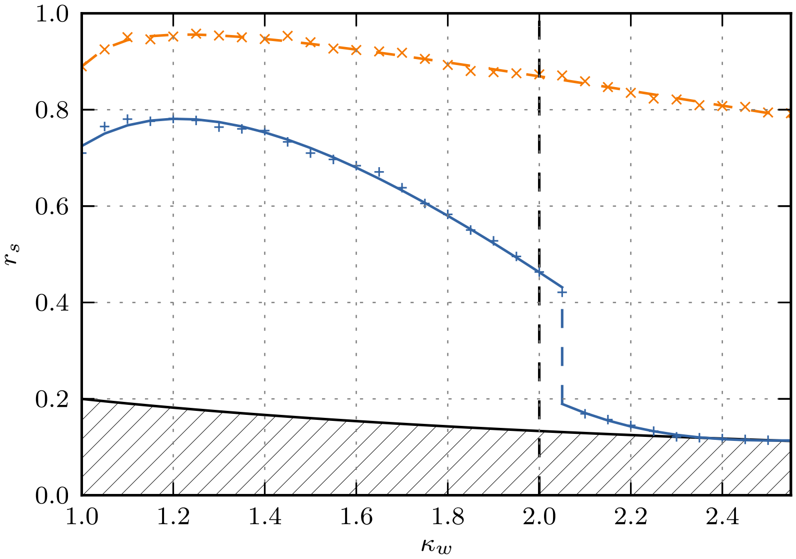

Figure 4.3: Characterization of the separability, r_s, of two close features with varying FWHM ratio, κ_w. Separation limit is determined for the SWD method (blue cross) and a direct detection method (yellow cross) as introduced in Sect. 4.3. The gray hatched area is the region in the plot for which the separation between the two features is lower than 2 pixels.

In the second separation test, the ratio $\epsilon_\mathrm{s} = S_1/S_2$ was varied for features with $w_1 = w_2 = 10$ pixels. The result demonstrates that SWD performs better than DD, with improvement factors rising from 30 % to 50 % with increasing SNR ratio ϵ_s.

Both tests show that SWD is successful at resolving out two close and partially overlapping features. Assuming that the simulated component width w_2 in both tests is similar to the instrumental PSF, r_s can be interpreted as $\approx 2/(1+\kappa_\mathrm{w})$ PSF, implying that SWD successfully distinguishes two marginally resolved features separated by $\approx 0.35\,\mathrm{PSF}\,(1+\epsilon_\mathrm{s})^{3/2}/(1+\epsilon_\mathrm{s}^2)^{1/2}$, which is close to the expected limit

$$r_\mathrm{s,lim} \approx \frac{2}{\sqrt{\pi}} \ln\left[\frac{S_2(1+\epsilon_\mathrm{s})+1}{S_2(1+\epsilon_\mathrm{s})}\right]^{1/2} \frac{(1+\epsilon_\mathrm{s})^2}{\sqrt{1+\epsilon_\mathrm{s}^2}} \times \mathrm{PSF}$$

for resolving two close features [*cf.* *Bertero et al.*, *1997*].

4.5 Structural displacement test

These tests used the full WISE processing on a set of two simulated jet images, first using the SWD algorithm to identify SSP features in each of the images, then applying the MCC algorithm to cross-correlate the individual SSP and to track their displacements from one image to the other. The jet images were simulated using the procedure described in the beginning of this section. A total of 500 elliptical features were inserted randomly inside the underlying smooth jet, with their SNR spread uniformly from 2 to 20 and the FWHM of the features ranging uniformly from 0.2 to 1 beam size. The simulated structures were convolved with a circular Gaussian (acting as an instrumental PSF) with a FWHM of 10 pixels. A damping factor α of -0.3 was used.

Positional displacements were introduced to the simulated features in the second image. The simulated displacements have both regular and stochastic (noise) components introduced as follows:

$$\Delta_x = f_x(x) + G_x\,, \quad \Delta_y = f_y(x) + G_y\,, \tag{4.3}$$

where f_x and f_y are the regular components of the displacement, and G_x and G_y are two random variables following the Gaussian distributions described by the respective means $< G_x >$, $< G_y >$ and standard deviations σ_x, σ_y. After the two images were generated, SSP were detected independently in each of them with the SWD and were subsequently cross-identified with the MCC.

4.5.1 Accelerating outflow

This displacement test explores a kinematic scenario describing an accelerating axial outflow with a sinusoidal velocity component transverse to the main flow direction:

$$f_x(x) = a + bx + cx^2\,, \quad f_y(x) = d\cos\left(\frac{2\pi\, x}{T}\right)\,. \tag{4.4}$$

Results of the WISE application are shown in Figs. 4.4–4.5 for $a = -2$, $b = 0.02$, $c = 0.00012$, $d = 10$, $T = 200$, for the stochastic displacement components with $\sigma_x = \sigma_y = 2$ and $\sigma_x = \sigma_y = 5$ (0.2 FWHM and 0.5 FWHM), respectively (all linear quantities are expressed in pixels). The largest expected displacement between the two images is 40 pixels. The WISE analysis was performed on scales 2–6 (corresponding to 4–64 pixels).

The comparison between the simulated displacements and the displacements detected by WISE reveals an excellent performance of the matching algorithm. To assess this performance, we computed the root mean square of the discrepancies between the simulated and detected displacements:

$$e_x = \sqrt{\frac{1}{N}\sum_{i=1}^{N}\left(\Delta x_i - f_x(x_i)\right)^2} \tag{4.5}$$

$$e_y = \sqrt{\frac{1}{N}\sum_{i=1}^{N}\left(\Delta y_i - f_y(x_i)\right)^2}\,, \tag{4.6}$$

where Δx_i, Δy_i are the measured x and y components of the displacement identified for the i^{th} simulated component, and x_i is the position of that component along the x axis in the first simulated image. The e_x and e_y determined from the WISE

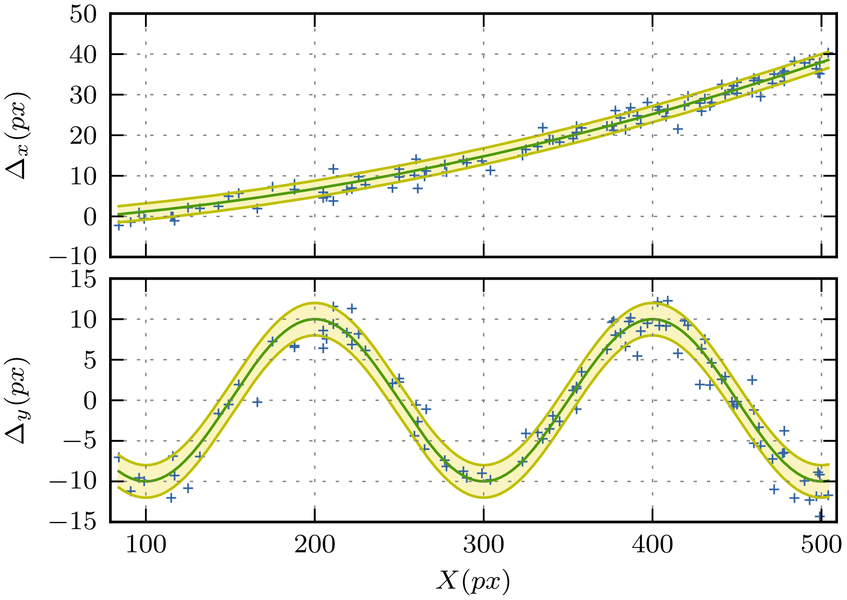

Figure 4.4: WISE decomposition and analysis of a simulated jet with an accelerating sinusoidal velocity field. The input velocity field (green line) is defined analytically and modified with a Gaussian stochastic component with an r.m.s of 0.28 FWHM of the convolving beam. The r.m.s. margins due to the stochastic component are represented by the yellow-shaded area. A total of 87% of all detected SSP have been successfully matched by WISE. The detected positional changes (blue crosses) show r.m.s. deviations of 0.19 and 0.20 FWHM (in x and y coordinates, respectively) from the simulated sinusoidal field.

decomposition do not exceed the σ_x and σ_y of the simulated data. For the first we obtain $e_x = 0.19$ and $e_y = 0.20$, while for the second test, we obtain $e_x = 0.43$ and $e_y = 0.42$. The number of positively matched features decreases with increasing stochastic component of the displacements, but the errors of WISE decomposition always remain within the bounds determined by the simulated noise.

These comparisons indicate that WISE performs very well even in the case of relatively large spurious and random structural changes (which may result from deconvolution errors, phase noise, and incompleteness of the Fourier domain coverage by the data). Because such spurious displacement is expected at a level of $\lesssim \mathrm{FWHM}/\sqrt{\mathrm{SNR}}$, WISE should be able to reliably identify displacement in regions detected at $\mathrm{SNR} \gtrsim 4$.

4.5.2 Two-fluid outflow

The purpose of this test was to investigate the possibility of using WISE to detect multiple velocity components in optically thin materials in which overlapping structures are moving at different speeds. To simulate such a two-fluid outflow, the initial set of features was divided into two groups F_1 and F_2. The SNR and FWHM of these features were derived from the same distribution. The simulated displacements, $\Delta_{1,2}$,

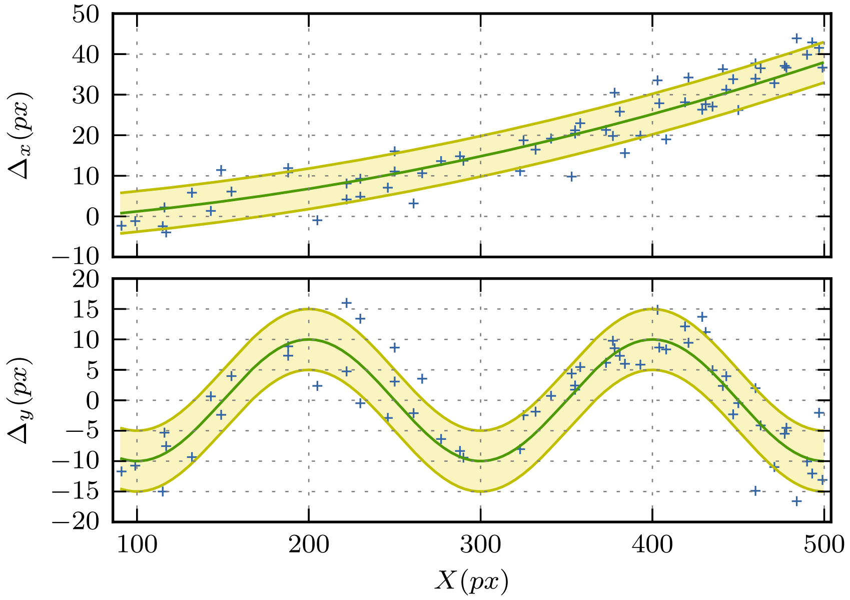

Figure 4.5: Same as in Fig. 4.4, but for the simulated stochastic component with an r.m.s. of 0.71 FWHM of the convolving beam. The total of 54% of all identified SSP have been successfully matched between the two simulated images. The respective r.m.s of the deviations of the detected displacements from the analytic sinusoidal velocity field are 0.43 FWHM and 0.42 FWHM, in x and y coordinates, respectively.

were oriented longitudinally (along the x-axis) in the outflow and were the same in all of the features of a given group, with $\Delta x_1 = a$ and $\Delta x_2 = b$, for the feature in F_1 and F_2, respectively.

Results of the WISE application are shown in Fig. 4.6 for $a = 5$ px, $b = 20$ px and $\sigma_x = \sigma_y = 2$ px (with a PSF size of 10 px). It is expected that a combination of more than two epochs is required to obtain enough positional changes to distinguish the two different values of the speed. In this case, combining the total of four epochs is found to be necessary. The speeds of individual features were determined through a statistical analysis of the detected displacements. The distribution of the detected displacements shown in Fig. 4.6 is bimodal, with two clearly separated peaks, and it can be used to derive the mean speed and its r.m.s. for each of the two simulated flow components. This yields $\Delta x_1 = 19.2 \pm 2.7$ px and $\Delta x_2 = 5.2 \pm 3.0$ px, which agrees well with the displacements used to simulate the two components of the flow.

4.6 Stacked cross correlation

The purpose of the stacked cross correlation analysis is to estimate the main velocity components of a stratified flow. To test this method, a similar setup as in sect 4.5.2 is used: simulated jets are prepared with two or more group of features for which different simulated displacements are assigned. Several epochs are generated and SCC is computed on a region of the images using pair of consecutive epochs. Peaks

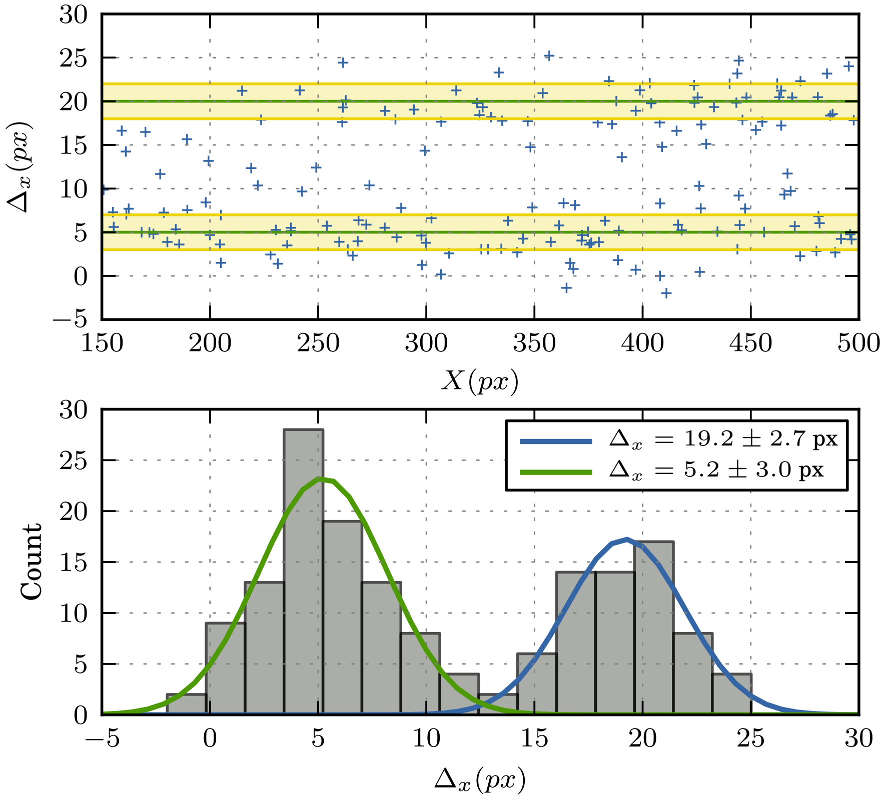

Figure 4.6: WISE decomposition and analysis of a simulated jet with two speed components. Two groups of features evolving at two different speeds are simulated. Upper panel: Blue crosses show the displacements detected by WISE from successive pairs in four simulated images (epochs). Green lines and orange shades indicate the two simulated displacements and r.m.s. of the Gaussian stochastic component. Lower panel: The histogram of the detected positional changes reveals two distinct components of the speed. The mean values of the speed and their r.m.s., indicated in the top right corner, agree well with the simulated displacements $\Delta x_1 = 5\,\text{px}$ and $\Delta x_2 = 20\,\text{px}$.

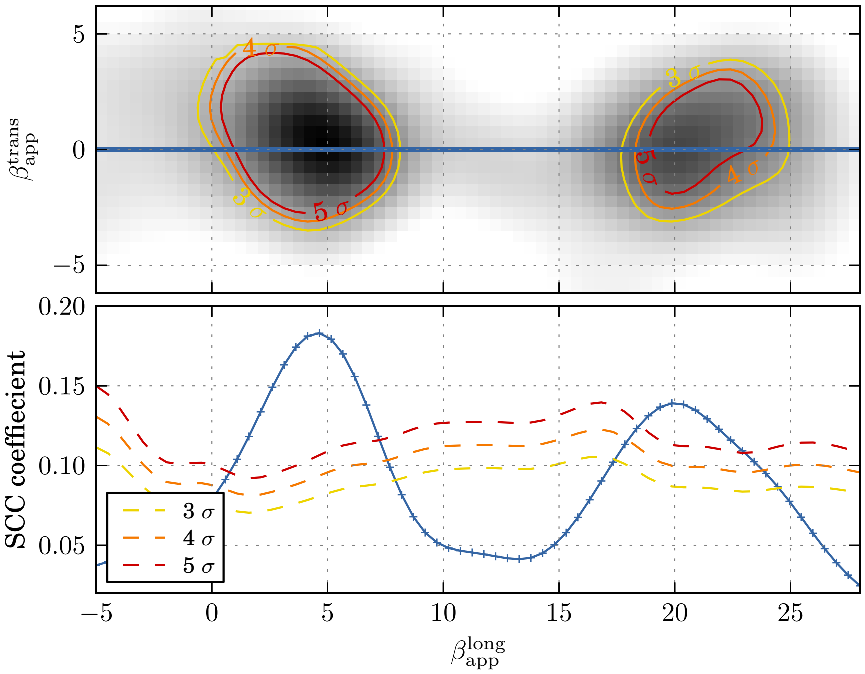

Figure 4.7: Stacked cross correlation analysis of simulated stratified jet. The resulting cross correlation map is shown at the top in greyscale along with contour of the significance. A slice along the longitudinal speed is shown at the bottom. SCC successfully identified the velocities of the two layers with a significance larger than $5\,\sigma$.

in the resulting cross correlation map are then located using a similar method as in Sect. 3.3.2. Additionally in order to obtain sub-pixel precision on the peak location, a 2D Gaussian is fitted on small box of the beam size around the local maximum. Significance and error of this peaks are measured following the procedures introduced in sect 3.5.1 and sect 3.5.2.

In a first test, a two fluid scenario is simulated in which a first group of features evolve with $\Delta x_1 = 5\,\mathrm{px}$, $\Delta y_1 = 0\,\mathrm{px}$, and a second group of features evolve with $\Delta x_2 = 20\,\mathrm{px}$, $\Delta y_2 = 0\,\mathrm{px}$. In both group, $\sigma_x = \sigma_y = 2\,\mathrm{px}$ is used. We recall that in our simulation the beam size is 10 px. Ten epochs are generated and SCC is computed on a region of 10 time the beam size longitudinally to the simulated jet using scales 1, 2 and 3 of the wavelet decomposition. This gives a total of 264 SSP. Result of this test is shown in Fig. 4.7. The SCC map display two prominent peaks corresponding to the two simulated displacements. No other peaks are found. For the first peak, a displacement of $\Delta x_1 = 4.5 \pm 0.4\,\mathrm{px}$ and a significance of $11.4\,\sigma$ is found. For the second peak, we measure $\Delta x_1 = 20.5 \pm 0.8\,\mathrm{px}$ with a significance of $6.7\,\sigma$. As a cross check, we confirm that for both displacements the distribution of displacements found in the test SCC used to measure the uncertainties is Gaussian with mean value corresponding to the formal displacement. This result are in perfect agreement with the simulated displacements. We should note also that we improved the uncertainties by a factor of 3 to 4 in comparison with the similar test performed

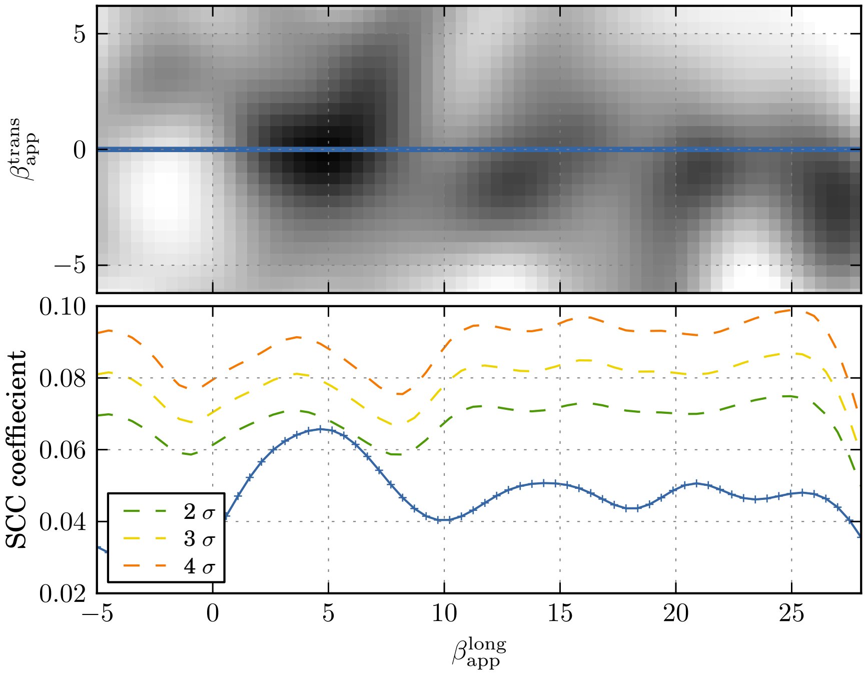

Figure 4.8: Stacked cross correlation analysis of simulated jet with random velocity field. The resulting cross correlation map is shown at the top in greyscale along with contour of the significance. A slice along the longitudinal speed is shown at the bottom. In the lower panel a random velocity field is simulated. In this case no peak with significance greater than $2\,\sigma$ could be detected.

in sect. 4.5.2 using normal WISE analysis. Also in this previous test only 4 epochs were considered, a much larger region were analyzed, totaling 370 SSP.

We will now test the correctness of our significance measurement by simulating a set of images in which no outstanding velocity components are present. To achieve this we simulate a single group of feature with random displacements drawn from a uniform distribution $0\,\mathrm{px} \leq \Delta_x \leq 40\,\mathrm{px}$ and $-5\,\mathrm{px} \leq \Delta_y \leq 5\,\mathrm{px}$. A similar procedure to the first test is then used to determine the peaks location and significance. The result is shown in Fig. 4.8. No peaks are found with more than $2\,\sigma$ significance compatible with the simulated random displacements.

4.6.1 Summary

Tests of WISE performed on simulated images demonstrated its capabilities for a robust decomposition and tracking of two-dimensional structures in astronomical images.

The WDS was tested against a direct detection (DD) algorithm in both sensitivity and separability. We noted improvements in three ways. First, the sensitivity was considerably improved: SWD was able to robustly detect features 5 times fainter than the DD, and doing so for both compact and larger structure. Second, the SWD keeps a low and predictable false detection rate. Finally, thanks to the multiscale nature of the decomposition, WDS greatly outperforms the DD for the detection of two close and partially overlapping features.

The MCC algorithm of WISE was tested using simulated images of jet with different analytically defined velocity fields. MCC performed remarkably well, recovering successfully complex velocity field even in the presence of important random structural changes. The test demonstrated also the ability of WISE to recover displacement as large as 3 time the beam size.

Finally, the SCC was tested in the scenario of a two fluid outflow. SCC was successful in detecting the two velocity component of the simulated stratified flow, being able to estimate the significance and uncertainty of each velocity components.

Chapter 5

WISE analysis of Mojave sources

Part of the work presented in this chapter is published in Mertens and Lobanov [2015]

5.1 Introduction

We have tested the performance of WISE on astronomical images by applying it to several image sequences obtained as part of the MOJAVE[1] long-term monitoring program of extragalactic jets with Very Large Baseline Interferometry (VLBI) observations [Lister et al., 2013, and references therein]. The particular focus of the analysis was made on prominent radio jets in the quasar 3C 273 and the radio galaxies 3C 120 and 3C 111. These jets show a rich structure, with a number of enhanced brightness regions inside a smooth and slowly expanding flow. This richness of structure has, on the one hand, been difficult to analyze by means of fitting it by two dimensional Gaussian features, on the other hand, it has always suggested that the transversely resolved flows may manifest a complex velocity field, with velocity gradients along and across the main flow direction [cf. Lobanov and Zensus, 2001; Hardee et al., 2005; Kadler et al., 2008].

The MOJAVE observations, with their typical resolution of 0.5 milliarcsecond (mas), transversely resolve the jets in the three objects and, in addition, they also reveal apparent proper motions of 3 mas/year in 3C 120 [Lister et al., 2013], which makes these jets excellent targets for attempting to determine the longitudinal and transverse velocity distribution and testing at the same time the performance of WISE.

The WISE analysis was applied to the self-calibrated hybrid images provided at the data archive of the MOJAVE survey[2]. The results of WISE algorithm were compared to the MOJAVE kinematic modeling of the jets based on the Gaussian model fitting of the source structure [see Lister et al., 2013, for a detailed description of the kinematic modeling].

---

[1] Monitoring Of Jets in Active galactic nuclei with VLBA Experiments

[2] www.physics.purdue.edu/MOJAVE

5.2 Analysis of the images

For each object, the MOJAVE VLBI images were first segmented using the SWD algorithm, with each image analyzed independently. The image noise was estimated by computing σ_j at each wavelet scale, as described in Sect. 3.3.1. Based on these estimates, a $3\,\sigma_j$ thresholding was subsequently applied at each scale. This procedure provides a better account for the scale dependence of the noise in VLBI images [Lal et al., 2010; Lobanov, 2012], which is expected to result from a number of factors including the coverage of the Fourier domain and deconvolution.

Following the segmentation of individual images, MCC was performed on each consecutive pair of images, providing the displacement vectors for all SSP that were successfully cross-matched. The images were aligned at the position of the SSP that was considered to be the jet "core" (which is typically, but not always, the brightest region in the jet). This was done to account for possible positional shifts resulting from self-calibration of interferometric phases and for potential positional shifts (core shift) due the opacity at the observed location of the jet base [Lobanov, 1998b; Kovalev et al., 2008].

For SSP that were cross-identified over a number of observing epochs, the combination of these displacements provided a two-dimensional track inside the jet. The track information from several scales was also combined whenever a given SSP was cross-identified over several spatial scales.

5.3 Jet kinematics in 3C 273

The MOJAVE database contains 69 images of 3C 273, with the observations covering the time range from 1996 to 2010 and providing, on average, one observation every three months. The PSF (restoring beam) size is on average 0.5 × 1.0 mas with a position angle (PA) of -2.3 degrees. The SWD was performed with four scales, ranging from 0.2 mas (scale 1) to 1.6 mas (scale 4).

For the MCC part of WISE, the individual images were aligned at the positions of their respective strongest and most compact components ("core" components) as identified by the MOJAVE model fits. The kinematic evolution of most of the detected SSP is fully represented by the MCC results obtained for a single selected SWD scale. However, long-lived features in the flow could eventually expand so much that the wavelet power associated with a specific SSP would be shifted to a larger scale, and the full evolution of such a feature was described by a combination of MCC applications to two or more SWD scales.

The core separations of individual SSP obtained from WISE decomposition are compared in Fig. 5.1) with the results from the MOJAVE kinematic analysis based on the Gaussian model fitting of the jet structure. To provide this comparison, the effective resolution of WISE must be reduced by excluding the scales 1–2 from the consideration. Comparison of the MOJAVE and the results obtained from the

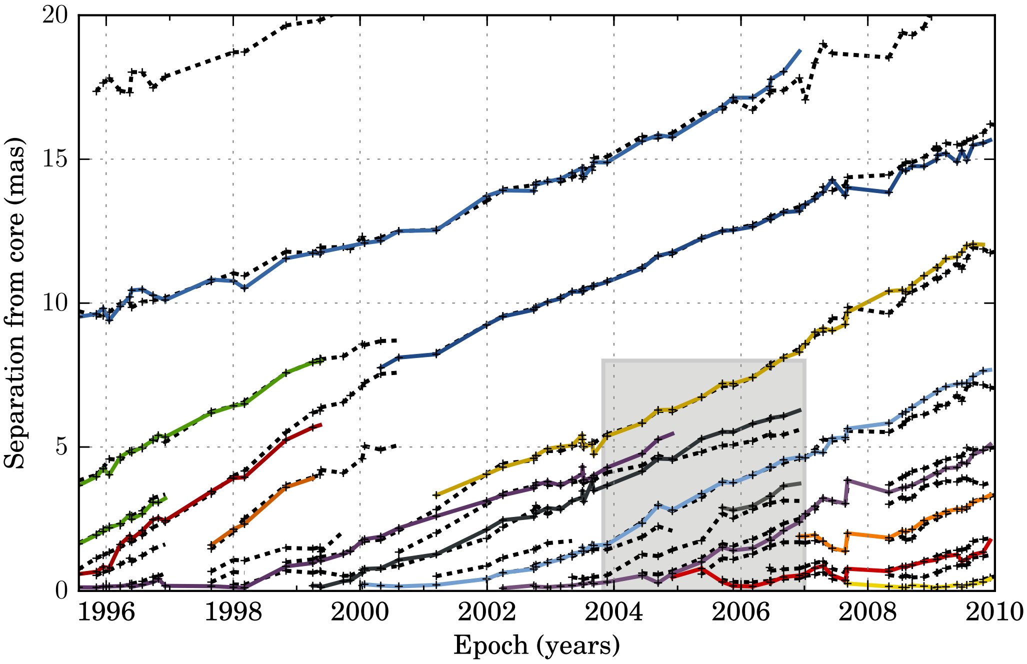

Figure 5.1: Core separation plot of the most prominent features in the jet of 3C 273. The model-fit based MOJAVE results (dashed lines) are compared with the WISE results (solid lines) obtained for SWD scales 3 and 4 (selected to match the effective resolution of WISE to that of the Gaussian model fitting employed in the MOJAVE analysis). A detailed analysis, also including SWD scales 1 and 2, was performed for the observations made between 11/2003 and 12/2006 (gray box); the results are shown in Fig. 5.3.

scales 3 and 4 of the WISE decomposition is shown in Fig.5.1. It indicates that WISE detects consistently nearly all the components identified by the MOJAVE model fitting analysis, with a very good agreement on their positional locations and separation speeds.

The two-dimensional tracks of the WISE features detected with this procedure are shown in Fig. 5.2, overplotted on a single-epoch image of the jet. The displacement tracks clearly show several “flow lines” threading the jet, which can be associated with the instability pattern identified in it [Lobanov and Zensus, 2001]. Some of these tracks can also be identified in Gaussian model fitting, but only if there is no substantial structural variations across the jet. If this is not the case, Gaussian model fitting becomes too expensive and too unreliable for the purpose of representing the structure of a flow. In this situation, WISE provides a better way to treat the structural complexity. We therefore conclude that WISE can be applied for the task of automated structural analysis of VLBI images of jets (and similar sequences of images of objects with evolving structure), yielding a great increase in the speed of the analysis (analyzing 69 images of 3C 273 took about ten minutes of computing, while the model fitting of these images required several days of the researchers’ time).

However, WISE can certainly go beyond the resolution of Gaussian model fitting

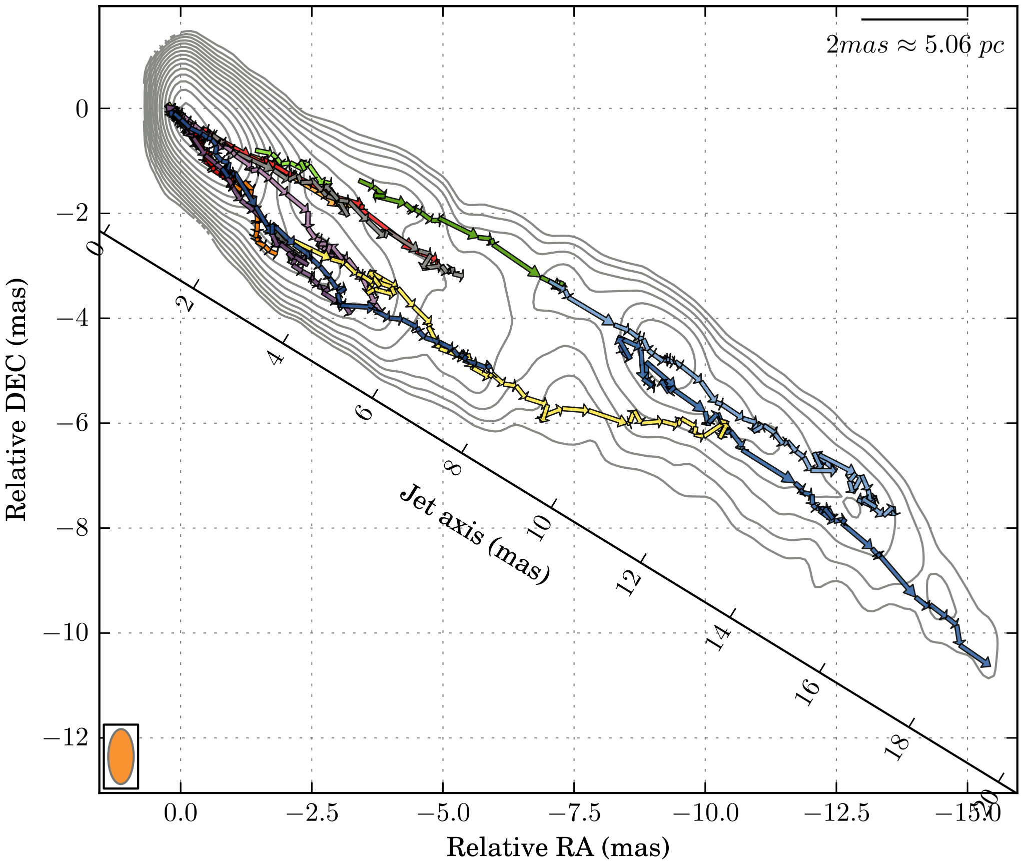

Figure 5.2: Two-dimensional tracks of the SSP detected by WISE at scales 3–4 of the SWD and compared in Fig. 5.3 with the features identified in the MOJAVE analysis of the images. The tracks are overplotted on a stacked-epoch image of the jet rotated by an angle of 32 degrees. Colors distinguish individual SSP continuously tracked over certain period of time. Several generic "flow lines" are clearly visible in the jet. These patterns are difficult to detect with the standard Gaussian model fitting analysis.

by also including the scales 1–2 which are smaller than the transverse dimension of the flow. An example of such an improvement is shown in Fig. 5.3, which focuses on MOJAVE observations of 3C 273 made between November 2003 and December 2006. At core separations larger than about 2 mas, WISE persistently detects several features at locations where the Gaussian model fits have been restricted to representing the structure with a single component. This is a clear sign of transverse structure in the flow, which is illustrated well by the respective displacement tracks shown in Fig. 5.3. These tracks provide strong evidence for a remarkably rich transverse structure of the flow, with three distinct flow lines clearly present inside the jet. These flow lines evolve in a regular fashion, suggesting a pattern that may rise as a result of Kelvin-Helmholtz instability, possibly due to one of the body modes that have been previously identified in the jet based on a morphological analysis of the transverse structure [Lobanov and Zensus, 2001]. That analysis also implied that

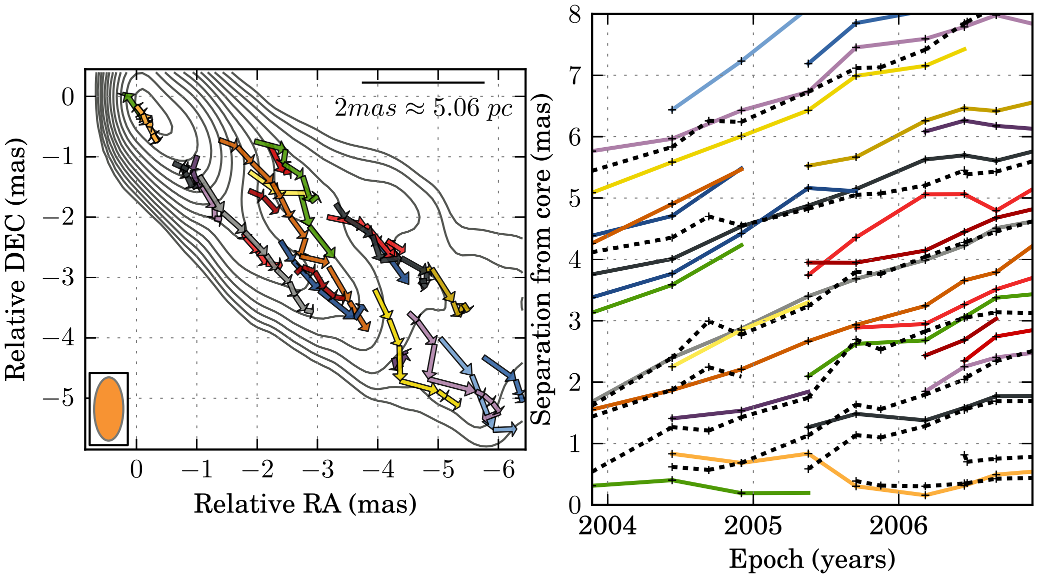

Figure 5.3: Detailed analysis of the jet of 3C 273 at the scale 2 of SWD for the epochs between 11/2003 and 12/2006. Right panel shows the Core separation plot. Dashed lines show the MOJAVE model fit components, colored tracks present the SSP detected and tracked by WISE. Left panel shows two-dimensional tracks of the detected SSP. Significant transverse structure is found in the jet, with up to three distinct flow lines showing strong and correlated evolution. At core separations $\gtrsim 2$ mas, WISE detects more significant features as the jet becomes progressively more resolved in the transverse direction (which also indicates that the structural description of the jet provided by Gaussian model fitting is no longer optimal). The apparent inward motion detected in a nuclear region (0– 0.3 mas) is most likely an artifact of a flare in the jet core.

the flow pattern probably rotates counterclockwise, and this rotation is consistent with the general southward bending of the displacement vectors (particularly visible in Fig. 5.3 at distances of 4.5–6 mas).

5.4 Jet kinematics in 3C 120

The MOJAVE database for 3C 120 comprises 87 images from observations made in 1996–2010, averaging to one observation every three months (but with individual gaps as long as one year). The PSF size is on average 0.5×1.3 mas with a PA of -4.6 degrees. We prepared these images for WISE analysis using the same approach as applied for 3C 273. To ensure sensitivity to the expected displacements of $\lesssim 3$ mas between subsequent images, we applied SWD on five scales, from 0.2 mas (scale 1) to 3.2 mas (scale 5).

Applied to the MOJAVE images of 3C 120, WISE detects a total of 30 moving SSP. The evolution of 24 SSP is fully traced at the SWD scale 2 (0.4 FWHM), and combining two SWD scales is required to describe the evolution of the six remaining

SSP. The resulting core separations of the SSP plotted in Fig. 5.4 generally agree very well with the separations of the jet components identified in the MOJAVE Gaussian model fit analysis. For the moving features, displacements as large as ~ 3 mas were reliably identified during the periods with the least frequent observations.

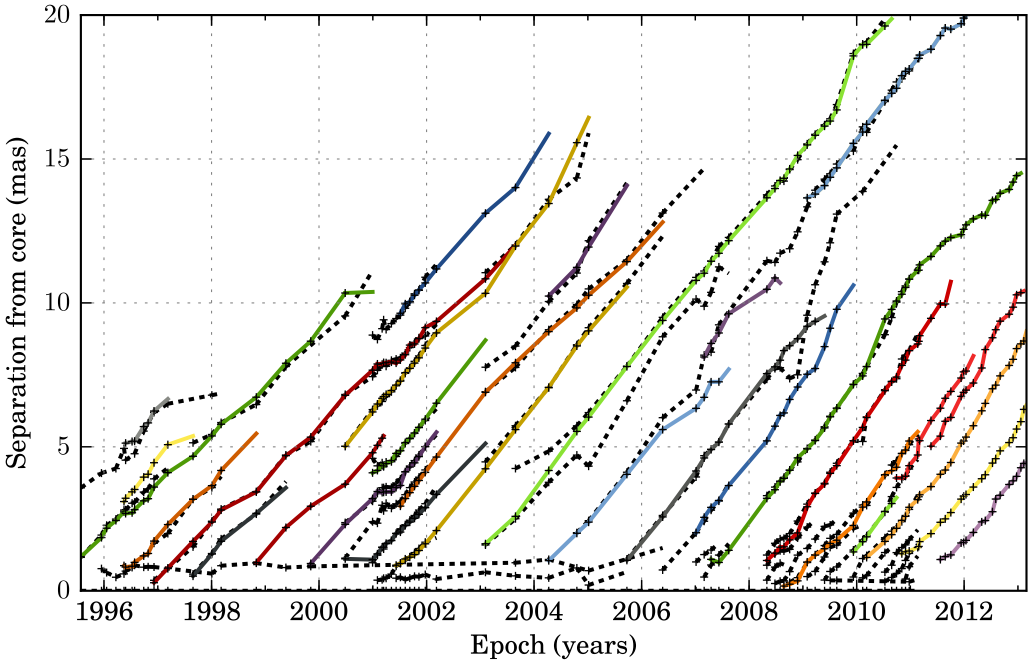

Figure 5.4: Core-separation plot of the features identified in the jet of 3C 120. The model-fit based MOJAVE results (dashed lines) are compared with the WISE results (solid lines) obtained for SWD scales 2 and 3 (selected to match the effective resolution of WISE to that of the Gaussian model fitting employed in the MOJAVE analysis).

The only obvious discrepancy between the two methods are the quasi-stationary features that are identified in the MOJAVE analysis, but are absent from the WISE results. A closer inspection of the wavelet coefficients recovered at the SWD scale 1 does not yield a statistically significant detection of an SSP at the location of the MOJAVE stationary component either.

The stationary feature identified in the MOJAVE analysis is often separated by less than 1 FWHM from the bright core, while it is substantially (factors of $\sim$ 50–100) weaker than the core. This extreme flux density ratio between two clearly overlapping components may impede identifying the weaker feature against the formal thresholding criteria of WISE. The fact that the Gaussian model fitting was performed in the Fourier domain (not affected by convolution) may have given it an advantage in this particular setting. Subjective decision making during the model fitting may also have played a role in the resulting structural decomposition.

Reaching a firm conclusion on this matter would require assessing the statistical significance of the model fit components identified with the stationary features and performing the SWD separation test for extreme SNR ratios. We defer this to fu-

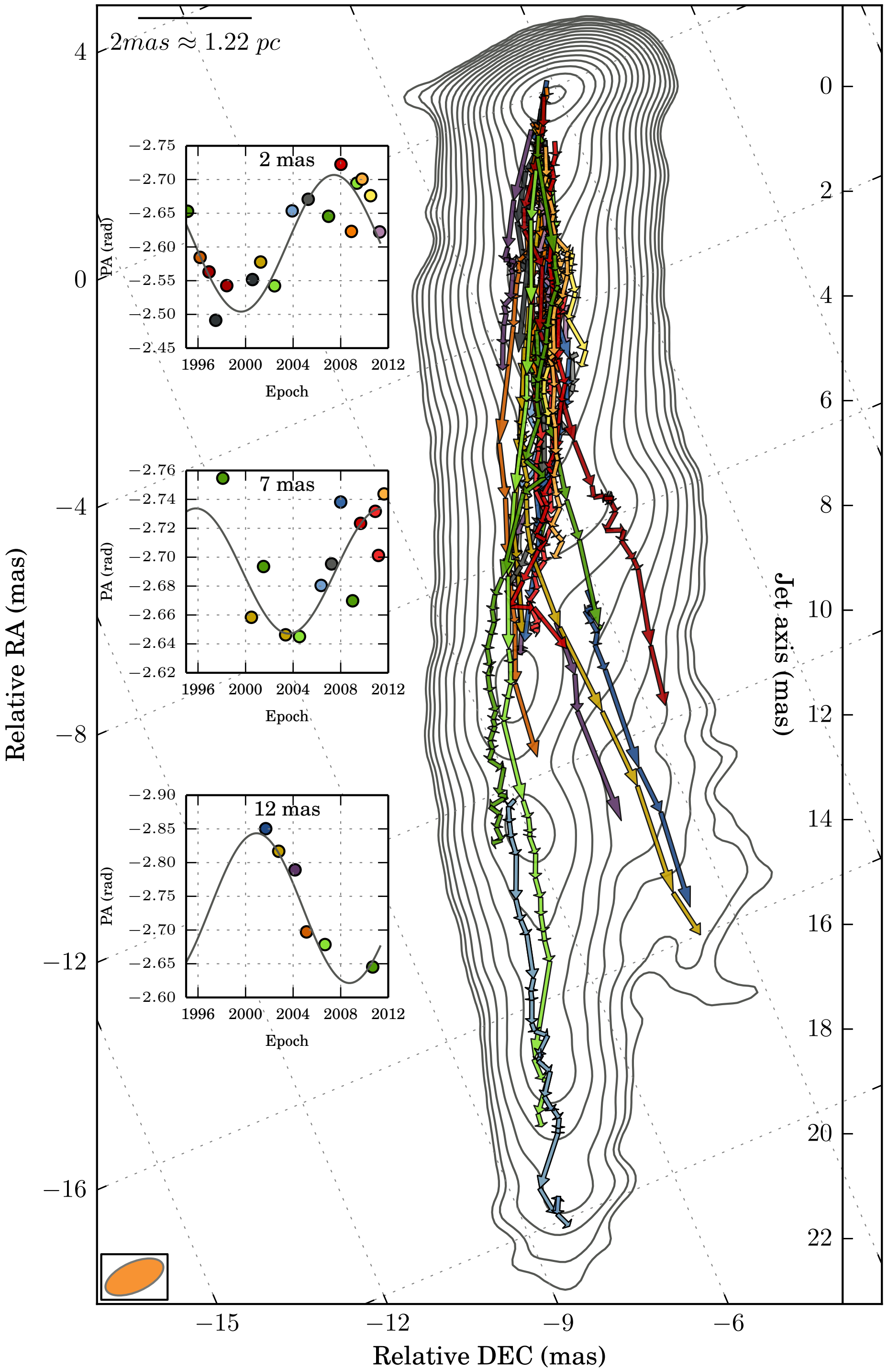

Figure 5.5: Two-dimensional tracks of SSP detected in 3C 120 overplotted on a stacked-epoch image of the jet rotated by -1.17 radian. The colored tracks correspond to the features plotted in Fig. 5.4 in the same color. The three insets show the time and PA of each components crossing a distance from the core of 2 mas, 7 mas and 12 mas respectively. The PA change can be fitted by a sinusoid.

ture analysis of the data on 3C 120, while noting again that WISE has achieved its basic goal of providing an effective automated measure of kinematics in a jet with remarkably rapid structural changes.

The magnitude of the structural variability of the jet in 3C 120 is further seen in Fig. 5.5, which shows the two-dimensional tracks of the SSP identified with WISE. The shape of individual tracks suggests a helical morphology, consistent with the patterns predicted from modeling the jet in 3C 120 with linearly growing Kelvin-Helmholtz instability [Hardee et al., 2005]. In this framework, the observed evolution of the component tracks is consistent with the pattern motion of the helical surface mode of the instability identified by Hardee et al. [2005].

The helical path of the components will result in position angle (PA) change over time that can be modeled by a sinusoid. We measures the time and PA of each components crossing a certain distance from the core (DFC). The exact timing is obtained by interpolation between the epoch before and after the component cross the DFC. Accurate measurements of the PA are made from linear fitting of the 2D track of the component taking only into account the features 3 mas before and 3 mas after the DFC. We repeat this operation for several DFC between 2 mas and 12 mas with a 0.25 mas step (corresponding to half time the beam size) and a sinusoidal function is fitted. Three examples of this procedure are shown in the insets of Fig. 5.5. At all DFC, the PA change is well described by a sinusoid with a period $T = 5700 \pm 350$ days. The instability is also evolving in the jet with a proper motion β^{w}_{app} which is generaly different from the flow proper motion β^{f}_{app}. We measured the time at which the sinusoid is maximum for all DFC (see Fig. 5.6), and found that our result can be well described by a linear function whose slope correspond to the apparent velocity of the instability:

$$\beta^{w}_{\mathrm{app}} = 2.0 \pm 0.1\,\mathrm{c} \tag{5.1}$$

Combining T and β^{w}_{app} gives us the apparent wavelength of the instability:

$$\lambda_{\mathrm{app}} = T\beta^{w}_{\mathrm{app}} = 15.8 \pm 1.3\,\mathrm{mas} \tag{5.2}$$

To further emphasize the evolution of the instability over time, we plot in Fig. 5.7 the path followed by the components as obtained from the simple sinusoidal modeling. The helical twist is in particular well visible after 8 mas from the core.

Hardee et al. [2005] also suggested that the structure of the flow is strongly dominated by the helical surface mode, which may explain the apparent lack of structural detail uncovered by WISE on the finest wavelet scale. In this case, observations at a higher dynamic range would be needed to reveal higher (and weaker) modes of the instability developing in the jet on these spatial scales. Altogether, the example of 3C 120 again demonstrates the reliability of the WISE decomposition and analysis of a structural evolution that can be inferred from comparing multiple images of an astronomical object.

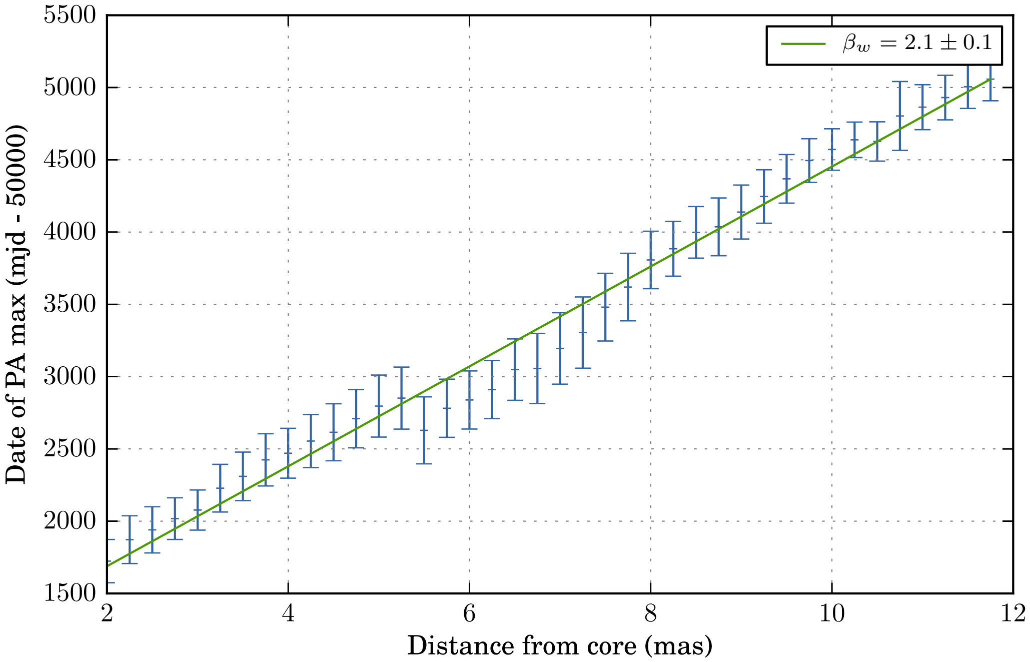

Figure 5.6: Time of the first PA maximum of the sinusoid function describing the change of PA with time at a certain distance from the core. The velocity of the instability ($\beta_w = 1.9 \pm 0.1$) is obtained from a linear fit.

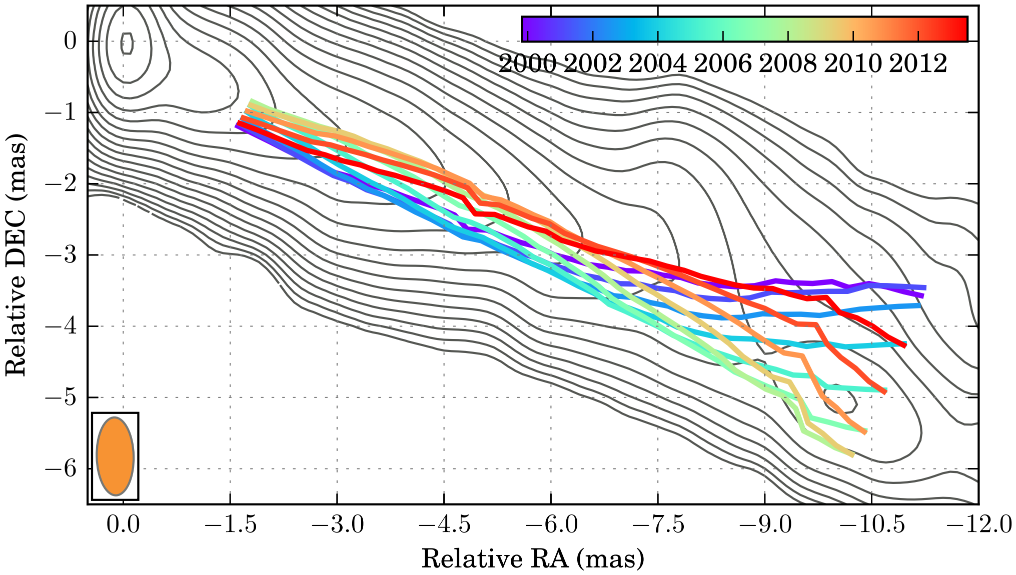

Figure 5.7: Evolution of the instability in the jet of 3C120 with time. For several epochs indicated by color, a line connect the corresponding PA of the fitted sinusoid function describing the change of PA with time. The plot confirms the significant and evolving transverse structure in the jet.

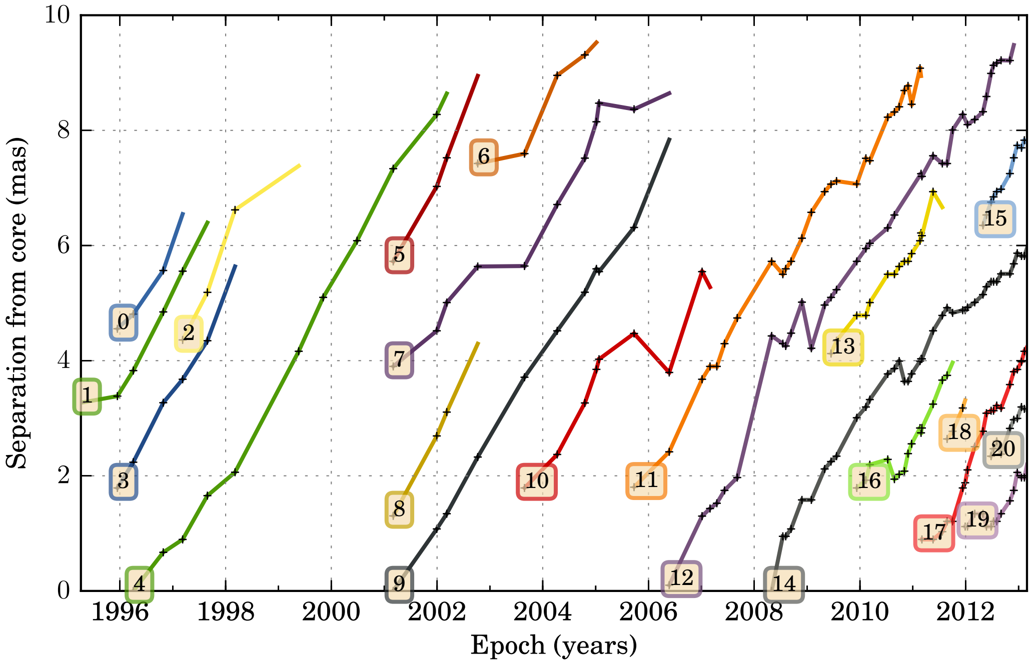

Figure 5.8: Core-separation plot of the features identified in the jet of 3C 111. The model-fit based MOJAVE results (dashed lines) are compared with the WISE results (solid lines) obtained for SWD scales 2 and 3 (selected to match the effective resolution of WISE to that of the Gaussian model fitting employed in the MOJAVE analysis).

5.5 Jet kinematics in 3C 111

The MOJAVE database contains 67 images of 3C 111, with the observations covering the time range from 1996 to 2013 and providing, on average, one observation every five months, and since ∼ 2008 an increased cadence of one observations every month on average. The PSF size is on average 0.6×0.9 mas with a PA of -6.3 degrees. The SWD was performed with four scales, ranging from 0.4 mas (scale 2) to 3.2 mas (scale 5).

Applied to the MOJAVE images of 3C 111, WISE detects a total of 20 moving SSP. The evolution of 12 SSP is fully traced at the SWD scale 2 (0.4 FWHM), and combining two SWD scales is required to describe the evolution of the 8 remaining SSP. The resulting core separations of the SSP plotted in Fig. 5.8. Only sparse observation are available up to ∼ 2008, still WISE perform well in this case and was able to detect displacements as large as 4 times the beam size.

Structural variability is also quite important in this source as shown in Fig. 5.9, which shows the two-dimensional tracks of the SSP identified with WISE. Some components shows radial trajectory with constant velocity (e.g. components 4 and 9), while several others follow an helical path with apparent deceleration (e.g. components 11, 12, 13, 14). This is best viewed in Fig. 5.10 which present the 2D tracks of a selection of components. This variety in trajectories has also been in noted in

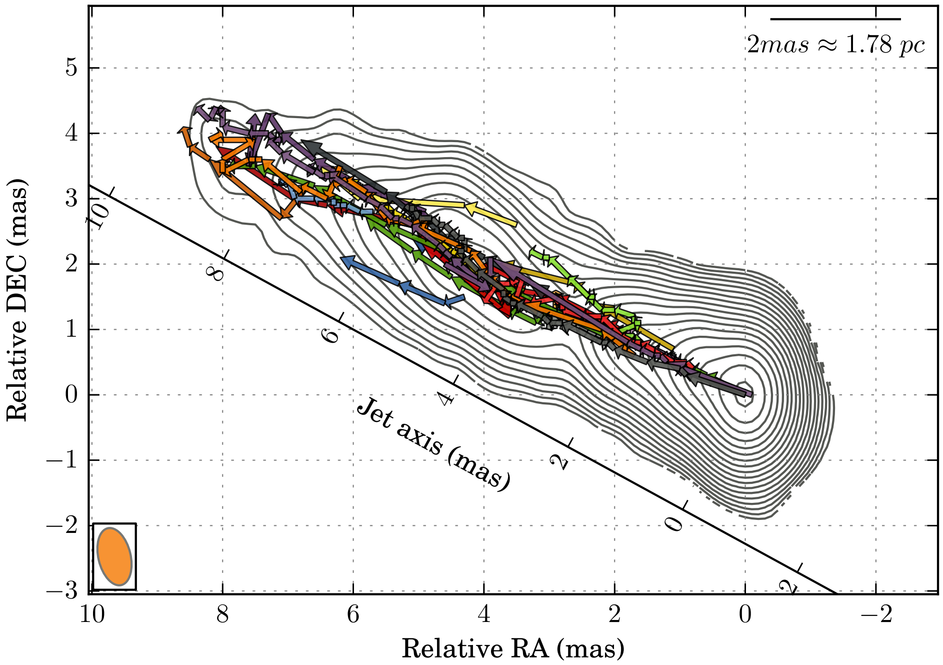

Figure 5.9: Two-dimensional tracks of SSP detected in 3C 111 at scale 2 of SWD. The colored tracks correspond to the features plotted in Fig. 5.8 in the same color. The tracks are overplotted on a stacked-epoch image of the jet.

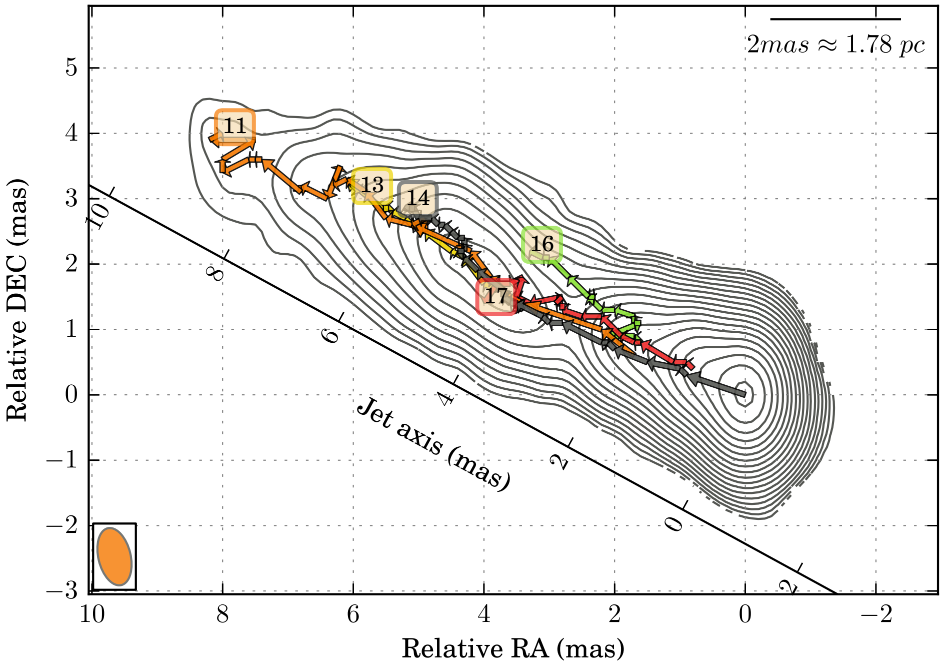

Figure 5.10: Similar to Fig. 5.9 for a selection of components.

Lister et al. [2013] for several parsec scale jets, and can generally be explained by flow instabilities. We can also note that the component identified in Kadler et al.

[2008] as being an aftermath of the 1996 major radio flare is component 4 in our analysis.

5.6 Summary and Discussion

Applications of WISE on the VLBI images of three prominent extragalactic jets showed the robustness and fidelity of results obtained from WISE compared with those coming from the "standard" procedure of using multiple Gaussian components to represent the observed structure. The inherent multiscale nature of WISE allows it also to go beyond the effective resolution of the Gaussian representation and to probe the two-dimensional distribution of structural displacements (hence probing the two-dimensional kinematic properties of the target object).

In addition to this, the multiscale approach of WISE has several other specific advantages. First, it allows simultaneous detection of unresolved and marginally resolved features as well as extended structural patterns at low SNR. Second, the method provides a dynamic and structural scale-dependent account of the image noise and uses it as an effective thresholding condition for assessing the statistical significance of individual structural patterns. Third, multiple velocity components can also be distinguished by the method if these components act on different spatial scales – this can be a very important feature to study the dynamics of optically thin emitting regions such as stratified relativistic flows, with a combination of pattern and flow speed and strong transverse velocity gradients.

Combining several scales also improved the cross-correlation employed by WISE, ensuring a reliable performance of the method in the case of severely undersampled data (with the structural displacement between successive epochs becoming larger than the dimensions of the instrumental point spread function).

In its present realization, WISE performs well on structures with moderate extent, while it may face difficulties in correctly identifying continuous structural details in which one of the dimensions is substantially smaller than the other (e.g., filamentary structure and thread-like features). If the ratio between the largest and smallest dimensions of this structure is lower than the ratio of the largest and smallest scales of WISE decomposition, the continuity of this structure may in principle be recognized. For more extreme cases, WISE will break the structure into two or more SSP that are considered independent. A remedy for this deficiency may be found in considering groups of SSP during the MCC part of WISE, or by applying more generic approaches to feature identification [*e.g.*, shapelets; *cf.* Starck and Murtagh, 2006].

Another probable, requiring additional attention is the scale crossing of individual features that may occur as a result of expansion (as was illustrated by the example of 3C 273) or the particular evolution of a complex three- dimensional emitting region projected onto the two-dimensional picture plane. At the moment, this problem has to be treated manually and outside of WISE, but an automated approach is clearly desired. One possibility here is to use the wavelet amplitudes associated with the same SSP at different scales and to select the dominant scale adaptively based on the comparison of these amplitudes and their changes from one observing epoch to another.

Implementing this step may also require implementing a reliable error estimation for the flux densities, and dimensions of SSP identified by WISE. This can be done on the basis of SNR estimates performed at each individual scale of WISE decomposition. Generically, it is expected that and SSP detected with a given SNR at a particular wavelet scale would have flux errors $\propto l_{\mathrm{w}}/\mathrm{SNR}^{-1}$ and the error on the SSP dimension would be $\propto l_{\mathrm{w}}/\mathrm{SNR}^{-1/2}$ [cf. Fomalont, 1999]. Such estimates can be implemented as a zeroth-order approach, but a more detailed investigation of the error estimates for the segmented wavelet decomposition is clearly needed.

Chapter 6

Kinematics of the jet in M87 on scales of 10^3–$10^4 r_g$

6.1 Introduction

M87 (Virgo A, NGC 4486, 3C274) is a giant elliptical galaxy. Its proximity ($D = 16.7$ Mpc; Jordán et al. [2005]) combined with a large mass of the central black hole ($M_{BH} \simeq 6.1 \times 10^9 M_\odot$; Gebhardt et al. [2011]) make it one of the primary source to probe the jet formation and acceleration at the base, and therefore has been extensively studied in the past. For this source, 1 mas $\sim$ 0.08 pc $\sim$ 140 R_s.

6.1.1 Jet properties at kiloparsec scales

The kiloparsec structure of the jet in M87 have been extensively observed in the radio regime using the Very Large Array (VLA) [Owen et al., 1989], the optical regime using the Hubble Space Telescope (HST) [Biretta et al., 1995], and the X-ray regime using the Chandra space telescope [Marshall et al., 2002]. Observations show a edge brightened conical jet with an apparent opening angle $\Theta_{\rm obs} \sim 6.5°$. The jet manifests several bright knots (see Fig. 6.1), with a particularly strong feature HST-1 located at a projected distance of $z_{\rm obs} \sim 0.84''$ mas. The jet expends uniformly up to knot A at a distance $z_{\rm obs} \sim 12''$. Analysis of multi-epoch observations has yielded detections of superluminal speeds of up to $\beta_{\rm app} \sim 6c$ in the optical [Biretta et al., 1999; Meyer et al., 2013] and $\beta_{\rm app} \sim 4c$ in the radio [Biretta et al., 1995; Cheung et al., 2007; Giroletti et al., 2012] at the location of HST-1, with evidence of deceleration downstream from this point. Several components with subluminal speed ($\beta_{\rm app} \sim 0.5c$) were also detected all along the jet [Biretta et al., 1999].

Both in the radio and optical maps, bright filaments, twisted into an apparent double helix have been identified. This has been successfully modeled as a consequence of Kelvin Helmholtz (K-H) instability developing in the jet [Lobanov et al., 2003; Hardee and Eilek, 2011], that also explains the slow features found in this jet. In the optical regime, the jet structure is dominated by knots, while the filaments

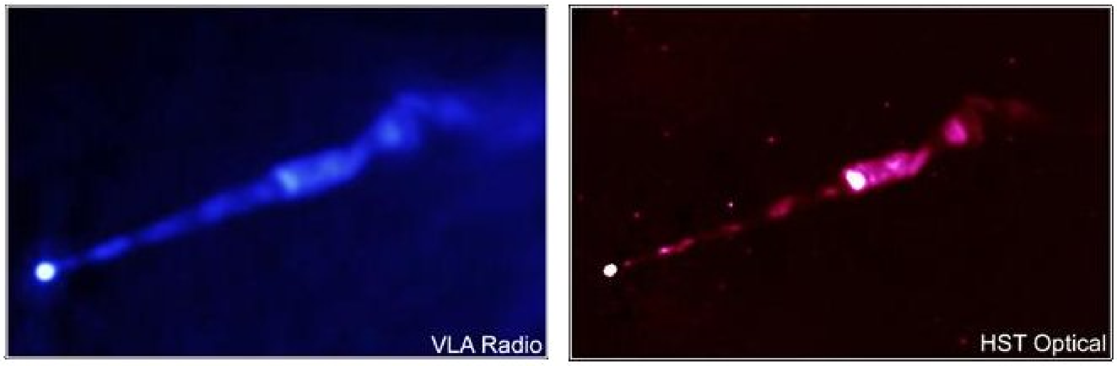

Figure 6.1: Radio and Optical image of the jet in M87 observed using the VLA and HST telescopes showing the kiloparsec structure. Credit: Radio: F. Zhou, F.Owen (NRAO), J.Biretta (STScI) Optical: NASA/STScI/UMBC/E.Perlman et al.

are more pronounced in the radio images. This difference has been interpreted in the framework of a stratified jet by Perlman et al. [1999a], in which the high energy plasma particles emitting optical synchrotron radiation originate from regions close to the spine of the flow, while from lower energy, radio emitting particles are concentrated in the outer layers of the flow.

6.1.2 Jet properties at sub-parsec to parsec scales

With the Very Large Baseline Interferometry (VLBI) technique, we are able to observe the jet in M87 down to sub-parsec scales, with the instrumental resolution increasing proportionally to the frequency of observation. At the same time, the observed VLBI core, considered to be located as the position on the jet at which the synchrotron self-absorption optical depth becomes unity, gets closer to the true base of the jet [Konigl, 1981]. Mulifrequency observations in conjunction with a phase-referencing technique were used by Hada et al. [2011] to probe the location of the central black hole, which was found to be at a projected distance from only about 40 R_s from the radio core observed at 43 GHz.

At lower frequencies, we are able to observe more extended structure at parsec scales and therefore make the connection with kiloparsec (kpc) structure observed with the VLA or HST. This approach was employed for determining the collimation profile of the jet[Asada and Nakamura, 2012]. A transition to a conical jet was found to occur at a projected distance $\sim$ 350 mas from the core. Upstream from that point, a parabolic jet has its radius r scaling with the deprojected distance from the core z as $r \propto z^a$, with $a = 1.73$ indicating that the jet is being collimated by magnetohydrodynamic (MHD) processes [Meier et al., 2001].

Proper motion detected in the jet in M87 at parsec scales has been the subject of a long debate. The jet has been observed at a 2 cm wavelengths as part of the MOJAVE project, with a reported slow sub-luminal speed ($\beta_{\text{app}} \sim 0.01c$) [Kovalev et al., 2007] which seems to be in contradiction with proper motion up to $\beta_{\mathrm{app}} \sim 4c$ observed at HST-1. Recently, [Asada et al., 2014] using European VLBI Network (EVN) observations at 1.6 GHz claimed to have detected gradual acceleration of the jet between 100 mas and 900 mas, finding a link between the sub-luminal acceleration found in the first 20 mas of the jet, and the relativistic speed at HST-1. A major issue is still persistent in this picture: Assuming that the jet is intrinsically bidirectional and symmetric, detection of a sub-luminal speed would imply a jet to counter-jet intensity ratio near unity while the jet in M87 is essentially one sided. The presence of a counter-jet seems to be confirmed by 2 cm and 7 mm VLBI observations. It however is not observed extending over more than 2 mas, and the jet to counter-jet intensity ratio is about 10. An alternative explanation proposed by Kovalev et al. [2007] is that this slow detected speed is either a pattern speed or a slow wind from an outer sheath. This conclusion is supported by the limb-brightened morphology of the jet. A reason why fast components were not found from the MOJAVE observation would then be the lack of sufficiently dense time sampling. The MOJAVE observations of M87 are indeed particularly irregular with an average time intervals of about 200 days, resulting in a maximum reliable speed detection of about $1c$, considering a separation of about the beam size between consecutive epochs. While Kovalev et al. [2007] could not identify any fast component, [Ly et al., 2007] reported possible features with speeds between $0.25c$ and $0.4c$ at a distance of 3 mas from the core, unfortunately based on only 2 epochs.

In an attempt to finally assess the true bulk speed of the jet at sub-parsec scales, systematic 7 mm Very Large Baseline Array (VLBA) observations were performed by Walker et al. [2008]. A first set of pilot observations indicated that a fast moving component could indeed be identified. This led to a program that produced a batch of eleven observations between 27 January 2007 and 26 August 2007, with an average time interval of 21 days, which allowed detection of apparent speeds as high as $3c$. The result is a set of excellent- quality, high-resolution VLBI maps with nearly homogeneous image rms noise. In these images, nearly the entire jet is well resolved, with up to 3 beams widths across the flow. The limb-brightened morphology is striking, especially if one looks at the stacked image that comprises the eleven observations into a single, high-sensitivity map. Determination of the velocity of the flow is however difficult from these data. The standard procedure for making proper motion measurements relies on modeling the source with a set of Gaussian components and cross-identifying those components between epochs. In this case, the complexity of the transversely resolved structure of the jet does not allow us to proceed with this approach. Visual inspection was done in an attempt to identify apparently related features and a speed of about $2c$ was consistently found [Walker et al., 2008]. This method obviously lacks objectivity and robustness, and it is difficult to use it for obtaining a complete velocity field map of the jet.

The WISE method presented in a previous chapter of this thesis is well suited for dealing with the frequent VLBI observations of M87 and studying the complex morphology and kinematics of the sub-parsec scale jet. In this chapter WISE analysis of the jet in M87 at sub-parsec scale is presented. In section 6.2, the WISE method is used to determine the two-dimensional velocity field and the collimation profile of the jet from the 7 mm VLBA observations of Walker et al. [2008]. An attempt at analyzing 2 cm VLBA observations from the MOJAVE project is presented in section 6.3. In section 6.4 the viewing angle is derived from the velocity observed on the counter-jet side. In section 6.5, we present an estimate of jet rotation inferred from the differential velocity between the northern and southern limbs of the jet. This allow us to constraint the field line angular velocity. Using the measured velocity field, the acceleration and collimation process is analyzed in the context of the MHD jet theory (Sect. 6.6). Based on these findings, the physical properties of the jet are discussed in section 6.7, addressing in particular the issues of the jet stratification, the magnetization, the launching mechanism, as well as the mass loading.

Throughout this Chapter, a cylindrical coordinate system (z, r, ϕ), is adopted, where z and r correspond to the axial and radial coordinates of the jet.

6.2 WISE analysis of 7 mm VLBA observations

We analyzed eleven epochs of the jet in M87 observed with the VLBA between 27 January 2007 and 26 August 2007 with an average time interval of 21 days and an average restoring beam of 0.43 × 0.21 mas. We refer to Walker et al. [2008] for a complete description of the data reduction. At the cadence of the 7 mm VLBA measurements, a displacement comparable to one fifth of the beam corresponds to a proper motion of 0.74 mas/yr, or $0.18c$, making this data set perfectly suited to detect speeds over $3c$ as well as slower subluminal speeds.

6.2.1 Velocity field analysis

WISE analysis of the M87 data is performed as described in chapter 3. Each map is decomposed and segmented using the Segmented Wavelet Decomposition (SWD) method, which provides a description of the two-dimensional jet structure based on a set of significant structural patterns (SSP). These features are then cross-identified between epochs using the Multiscale Cross Correlation (MCC) method in order to obtain proper motions.

To ensure sensitivity to the expected displacements of $\sim 2c$, we applied the SWD on eight scales, from 0.07 mas to 0.84 mas, using a triangle scaling function. Following Sect. 3.4.5, an intermediate scale wavelet decomposition is also performed using a triangle2 scaling function. This ensures a maximum detectable displacement of about 0.84 mas implying a maximum detectable motion of about 15 mas/yr ($\beta_{\mathrm{app}} \sim 4c$).

The MCC is then performed on each consecutive pair of images. Based on previous measurements and on a visual inspection, we expect a mixture of high and low displacements. To ensure the correct detectability of both displacements, we use a tolerance factor of 1.5. The correlation threshold is set to 0.6. Finally, velocity constraints are set according to the expected largest displacement ranges: in the jet side, the longitudinal velocities are allowed to range between -2 mas/yr and 15 mas/yr, transversally they are allowed to range between -5 mas/yr to 5 mas/yr. On the counter jet side, velocities ranging between -2 mas/yr and 2 mas/yr longitudinally and transversally are allowed. We will only consider the displacements determined at the lowest scale (0.07 mas) for the analysis.

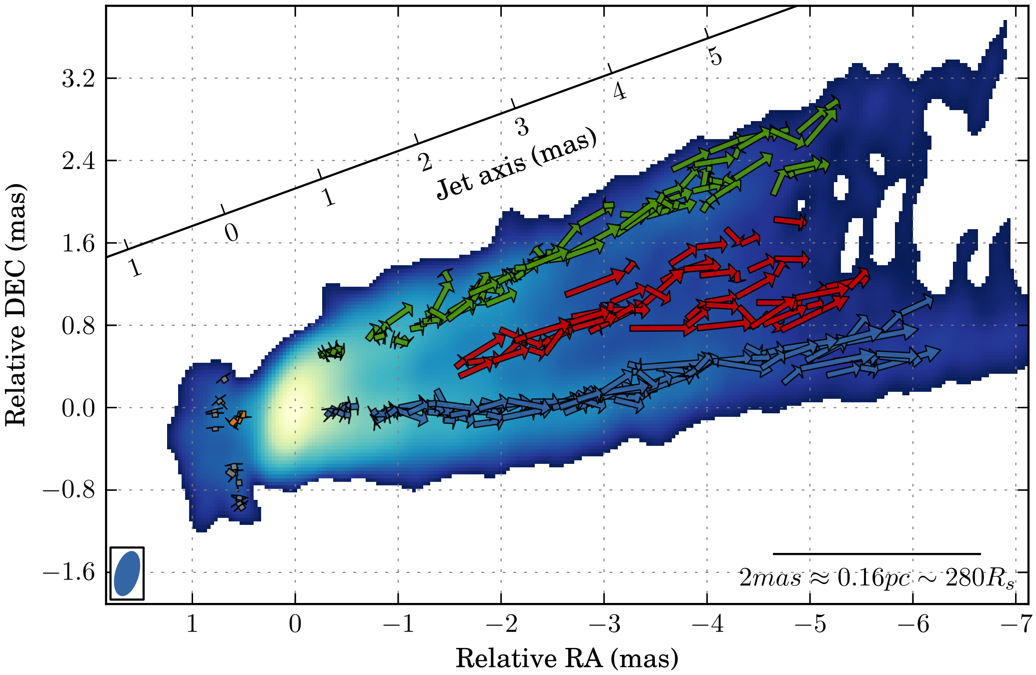

Figure 6.2: Observed displacements of the significant structural patterns detected in the jet of M 87. Three main regions are detected: a southern (blue) and northern (green) rail and a central region (red). The component found in the inner part of the counter jet (orange), is interpreted as originating from the counter jet. In the outer part (gray), slower motion is found with tendency for a south to north direction.

At each epoch of observation, a total of 68 SSPs are detected on average. A matching SSP is found on 51 % of these detections, resulting in a total of 391 displacement vectors. The normalized cross correlation between matching sets of SSPs is on average over 0.8. Uncertainty in the velocity is obtained from the uncertainty in the SSP position which is computed using the method in Sect. 3.3.4.

The SSP displacements obtained from this analysis are shown in Figure 6.2, and the transverse and longitudinal components of the corresponding velocities are plotted in Figure 6.3. These two Figures reveal the complex kinematics of the jet, with subluminal and superluminal motions. The extracted information on the dynamics of the jet is extremely rich. Before further analysis, we summarize the main phenomenological observations:

- Three self consistent regions are found in the jet. In the edge-brightened part

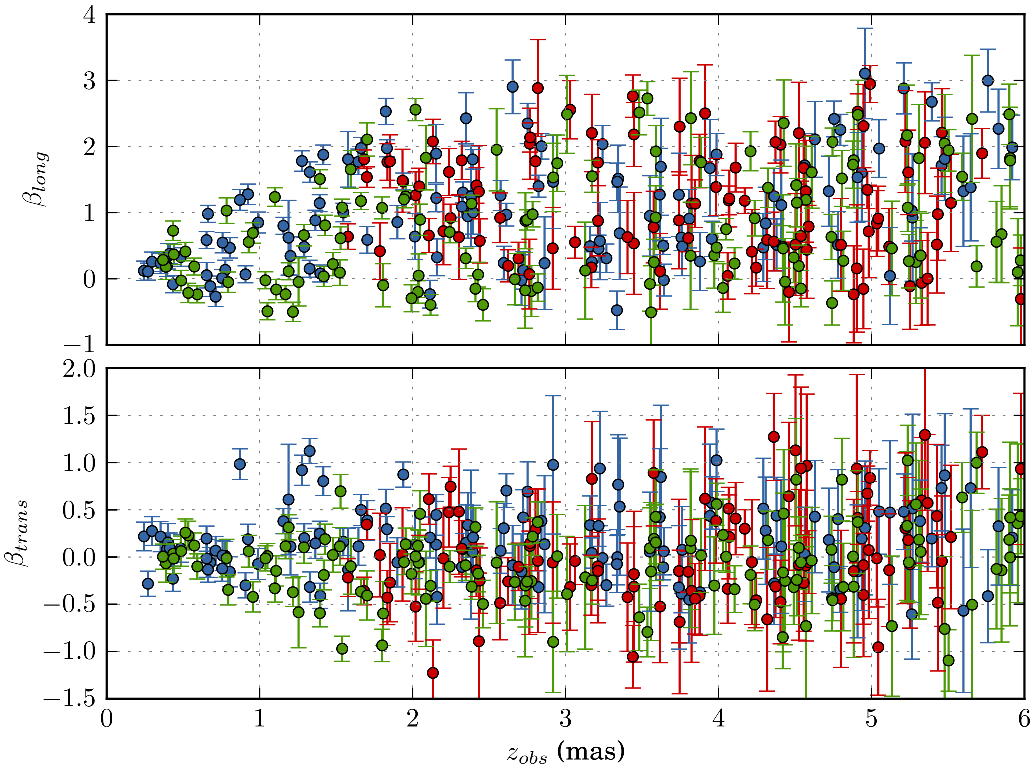

Figure 6.3: Longitudinal (top) and transverse (bottom) velocities of SSP measured in the jet of M87. The colors indicate the region of the SSP similarly to Fig.6.2: green and blue indicate the northern and southern rail respectively. Red indicates the central region.

of the jet, displacements of features comprise a northern and southern rail. The kinematics is more complex in the central region which manifests substantial transverse motions as well.

- Velocities in the central region are detected starting at around $z_{\rm obs} \sim 1.75$ mas, when the width of the jet corresponds to about three beam sizes.

- Both slow (subluminal) and fast (superluminal) speeds are found in each of the three jet regions. This might be the result of jet stratification.

- Apparent acceleration is observed in the first 2 mas of the southern and northern part of the jet. At a distance $z_{\rm obs} \sim 0.25$ mas, the maximum apparent velocity is $\beta_{\rm app} \sim 0.2c$. The maximum apparent velocity then linearly increases up to $\beta_{\rm app} \sim 2.5c$ at $z_{\rm obs} \sim 2$ mas.

- Between $z_{\rm obs} \sim 2$ mas and $z_{\rm obs} \sim 6$ mas, we measure no or slow acceleration. A maximum velocity of $\beta_{\rm app} \sim 3\,c$ is found at $z_{\rm obs} \sim 5$ mas.

- We also observe an oscillation in the velocities. Minima in the jet speed are found at $z_{\rm obs} \sim 1.2$ mas, 2.25 mas and 4.25 mas.

- In the counter jet side, one component that we can follow over 5 epochs is found to move away from the core at a position which is consistent with the extension of the jet northern rail. We can interpret it as originating from the counter jet, hence making the first determination of a speed in the counter jet.
- Several other features in the outer part of the counter jet have a slow motion tending towards the northward direction, suggesting a clockwise rotation around the jet axis as viewed projected onto the sky. Their origin is not clear at present, and it should be a matter of further investigation.

In order to assess the robustness of the result, we perform a bootstrapping analysis consisting of carrying out a WISE analysis with a similar configuration on a randomly shuffled list of images. We found that while the global correlation coefficient of the shuffled results is similar to the formal one, the number of matched SSPs is on average 50 % less important. The initial acceleration in the first 2 mas has for consequence a correlation between z_{obs} and β_{long} which is not seen in the shuffled results. This demonstrate that the solution found by WISE does not represent a spurious correlation. However, because of the complexity of the kinematic in this jet a statistical approach must be taken to interpret this solution. As a first step, we will investigate the stratification of the jet using stacked cross correlation analysis.

6.2.2 Stacked cross correlation analysis

The large range of velocities measured all along and across the jet indicate a complex physical nature of the flow, with both acceleration and stratification likely to play important roles. Is is difficult to determine the basic properties of the stratified flow from the WISE velocity field analysis alone and a stacked cross correlation (SCC) is required in this case. Different jet regions can be examined using this method. We follow the procedure described in Sect. 4.6: The SCC is computed on a specified region of the jet using pairs of consecutive epochs. Peaks in the resulting cross correlation map are then located and the significance and error of these peaks are determined following the procedures introduced in Sect. 3.5.1 and Sect. 3.5.2. For the analysis described below, the SSP detected at 3 different scales between 0.035 mas and 0.105 mas are used.

Close to the core, stratification is not so important and the SNR of the SSP is usually quite high, so the regions located between 0.5 mas and 1 mas in the northern and southern part of the jet can be analyzed independently. However further away from the core, empirical attempts revealed that analyzing an extended region between 1 mas and 4 mas was necessary to obtain the required significane of the SCC.

SCC analysis of the jet region between 0.5 and 1 mas from the core

In the northern part of the jet, the SCC is computed from a total of 42 SSP. The resulting cross correlation maps and the corresponding significance measurements

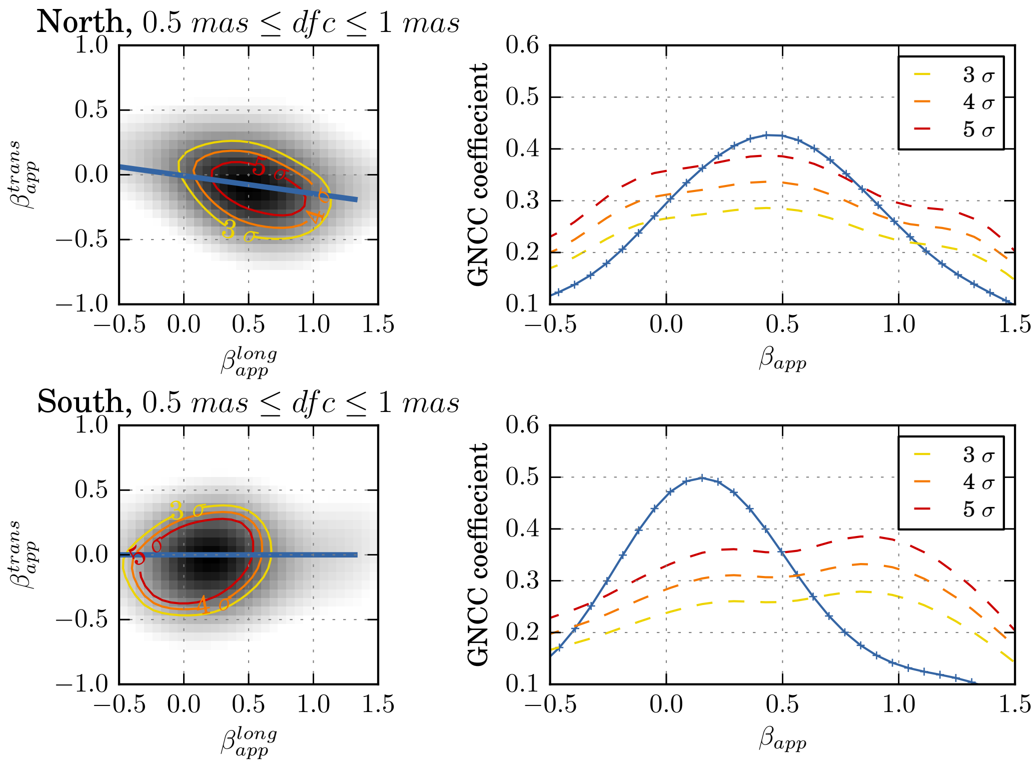

Figure 6.4: Stacked cross correlation analysis of the northern (top panel) and southern limbs (bottom panel) of the jet at distances between 0.5 and 1 mas from the core. The cross correlation map is shown in the left in greyscale. Contours indicate the statistical significance of the correlation. A slice along the blue line is shown at the right. A single velocity component with more than $5\,\sigma$ significance is found in both parts.

are plotted in Fig. 6.4. A single velocity component is found in this case with an apparent speed of $\beta_{\rm app}^{\rm north} = 0.48 \pm 0.06c$ and a significance of $5.9\,\sigma$. In the southern part, SCC using a total of 47 SSP reveal also a single velocity component with $\beta_{\rm app}^{\rm south} = 0.21 \pm 0.04c$ and a significance of $8.7\,\sigma$. The results are further summarized in Table 6.1.

The SCC analysis hence did not unveil any stratification close to the core. This result confirms however the speeds measured in Sect. 6.2.1 and that generally subluminal speeds are found in this region. If any stratification would be present, their respective velocity difference would be too small to be detected using the SCC. In this case, the apparent velocity measured by this method can be interpreted as a mean velocity of the different layers probed by the observations.

SCC analysis of the jet between 1 and 4 mas from the core

The SCC analysis was performed independently in the northern, southern and central parts of the jet, using 245, 267, and 217 SSP, respectively. The resulting cross-correlation maps are plotted in Fig. 6.5. The measured correlations suggest a strong

Table 6.1: Velocity components identified from stacked cross correlation analysis of the northern and southern region at distances between 0.5 and 1 mas from the core.

Region	$\beta_{\rm app}^{trans}$	$\beta_{\rm app}^{long}$	$\beta_{\rm app}$	Significance
North	-0.10 ± 0.03	0.47 ± 0.05	0.48 ± 0.06	5.9
South	-0.02 ± 0.03	0.21 ± 0.03	0.21 ± 0.04	8.7

Table 6.2: Velocity components identified from stacked cross correlation analysis of the northern, central and southern region at distances between 1 and 4 mas from the core.

Region	$\beta_{\rm app}^{trans}$	$\beta_{\rm app}^{long}$	$\beta_{\rm app}$	Significance
Fast velocity component				
North	0.27 ± 0.04	2.40 ± 0.03	2.41 ± 0.05	8.0
Center	-0.1 ± 0.1	2.32 ± 0.17	2.32 ± 0.20	4.0
South	-0.41 ± 0.07	2.16 ± 0.14	2.20 ± 0.15	2.5
Slow velocity component				
North	0.01 ± 0.03	0.17 ± 0.04	0.17 ± 0.06	5.1
Center	0.13 ± 0.12	0.34 ± 0.30	0.37 ± 0.32	4.4
South	-0.14 ± 0.07	0.47 ± 0.22	0.49 ± 0.24	3.9

stratification, unveiling two main velocity components in all three regions of the jet: a slow, mildly relativistic speed ($\beta_{\rm app} \sim 0.35\,c$) and a faster, relativistic speed ($\beta_{\rm app} \sim 2.3\,c$). The cross-correlation measurements are summarized in Table 6.2. In most case the significance of the velocity components are above $4\,\sigma$. All but one kinematic components are detected at significances $\geq 3.9\,\sigma$. The somewhat low (2.5σ) formal significance of the correlation found for the fast velocity component in the southern jet region may result from a broader range of velocities compared to the northern region. The overall significance of the measured stratification is further supported by the fact that we find consistent results in all three regions of the jet.

The similarity of both the fast and the slow velocity components of the central region to the respective velocity components of the northern and southern regions suggests that the SSP detected in all three regions originate from the same layer of the jet. Based on the well established limb brightening of the jet in M87, we can expect that the SSP detected in this central region will be brighter when they originate from the outer regions of the flow. This suggest that the putative spine is either too faint or optically thick at our observing frequency.

The observed jet stratification can be interpreted in several different ways. One potential scenario involves a two components jet: an inner fast relativistic outflow originating either from the magnetosphere of the central engine, or from the inner part of the accretion disk, and an outer non-relativistic wind originating from surroundings parts of the accretion disk [Sol et al., 1989; Tsinganos and Bogovalov,

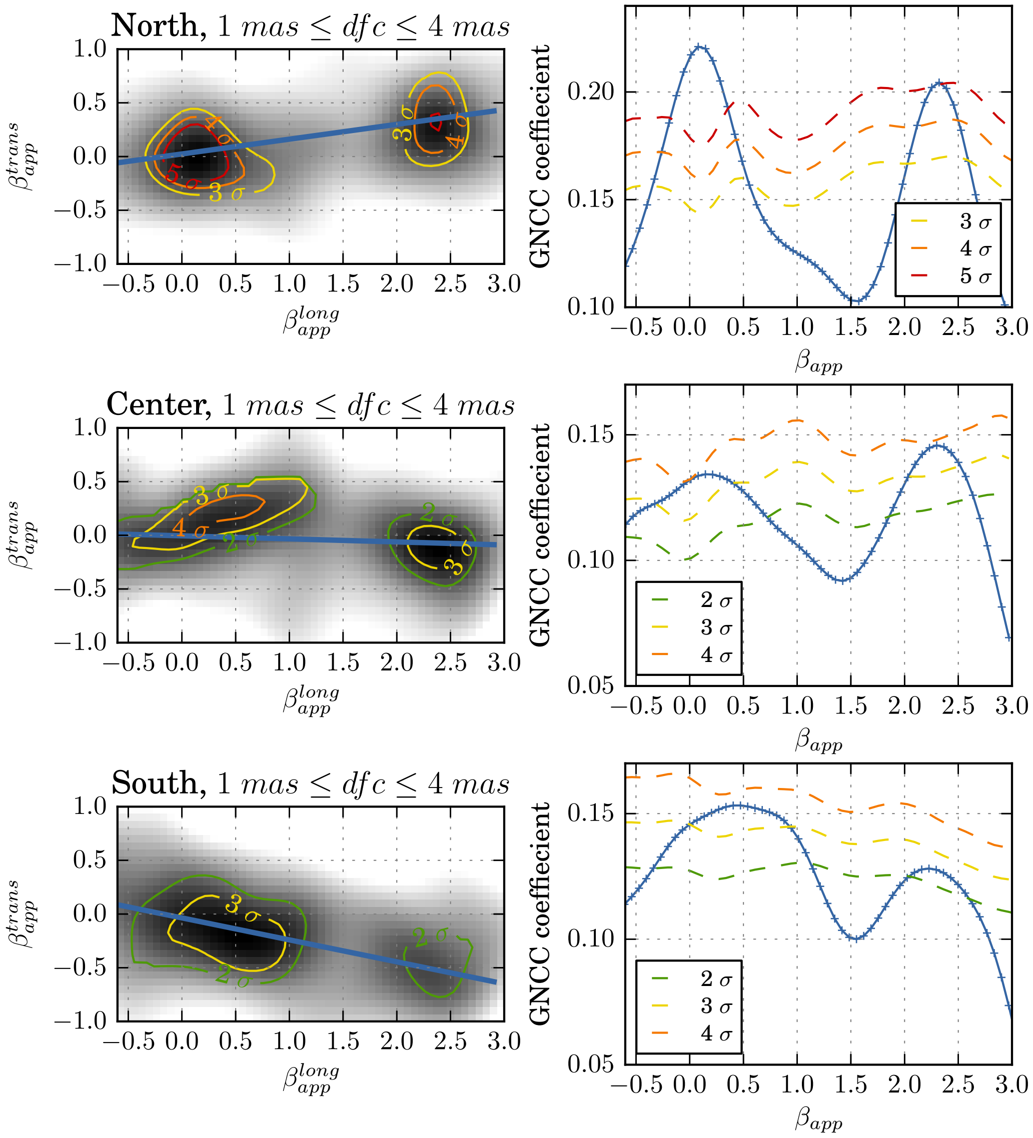

Figure 6.5: Stacked cross correlation analysis of the northern (top panel), central (middle panel) and southern limbs (bottom panel) at a distance between 1 and 3 mas from the core. The cross correlation map is shown on the left in greyscale along with contours of the significance. A slice along the blue line is shown at the right. Two main velocity components are consistently found in the three regions of the jet.

2002]. We note also that MHD simulation of AGN jets has shown important velocity gradients transverse to the flow [e.g. Komissarov et al., 2007]. In this context field lines originating from different parts of the accretion disk would result in different flow speed.

In a second scenario, the fast component would be the intrinsic flow speed, while the slower one would be interpreted as a pattern speed associated with current driven (CD) or velocity shear driven (K-H) instability, or changes in jet direction. In general, K-H instability pattern speed is expected to be considerably slower than the flow speed. The detailed analysis of the jet in in 3C 120 that we conducted in Sect. 5.4 reveals that the detected helical mode of the K-H instability propagates in this jet at a speed two time slower on average than the underlying flow. It is also suggested that the slow sub-relativistic speed ($\beta_{\mathrm{app}} \sim 0.5\,c$) detected in the jet in M87 at kiloparsec scale indicate a pattern speed from K-H instability [Lobanov et al., 2003].

6.2.3 Jet collimation

In the MHD context, the jet collimation profile plays an important role in the acceleration of the flow and hence in the conversion from Poynting flux into kinetic energy [Begelman and Li, 1994; Lyubarsky, 2010]. The SWD method introduced in Sect.3.3 provides a reliable way to analyze the evolution of the jet radius with distance from the core. The resulting images are less affected by noise, and it is possible to select the optimal scale for the structure that we are analyzing. This procedure is further improved by considering the full set of the observations.

To determine the jet collimation profile, stacked wavelet scale (SWS) images of M87 are prepared, composed of all SSP detected at a given scale j from all available epochs. Close to the core, the jet limb is well described by the SWS at the smallest wavelet scale. As the jet expands, the width of each of its limbs is best described by progressively larger SWS scales. Scale 1 (corresponding to 0.07 mas) of the SWS is used between $z_{\mathrm{obs}} = 0.4$ mas and $z_{\mathrm{obs}} = 0.8$ mas, scale 2 (0.14 mas) is then used up to $z_{\mathrm{obs}} = 1.6$ mas, and finally scale 3 (0.21 mas) is selected at larger core separations.

The jet radius is estimated by taking transverse profiles of the stacked-epoch SWS image of the jet at regular intervals ($\delta z = 1$ px $= 0.035$ mas) and measuring the distance between the two limbs of the jet. A Gaussian profile is fitted to each of the limbs to further improve this calculation. It is particularly difficult to obtain a robust uncertainty estimate for these measurements. Our conservative approach is to assume that the position error of limb determination is 1/4 of the beam (0.07 mas) at the core of the jet, and it linearly increases to reach 1/2 of the beam at the last profile, located at 6.6 mas from the core. The result is plotted in Fig. 6.6. The apparent jet opening angle can also be computed using:

$$\Theta_{\mathrm{app}} = \arctan\left(\frac{r}{z_{\mathrm{obs}}}\right) \tag{6.1}$$

The jet collimation profile is well described by a power law $r \propto z^k$ with $k = 0.60 \pm 0.02$

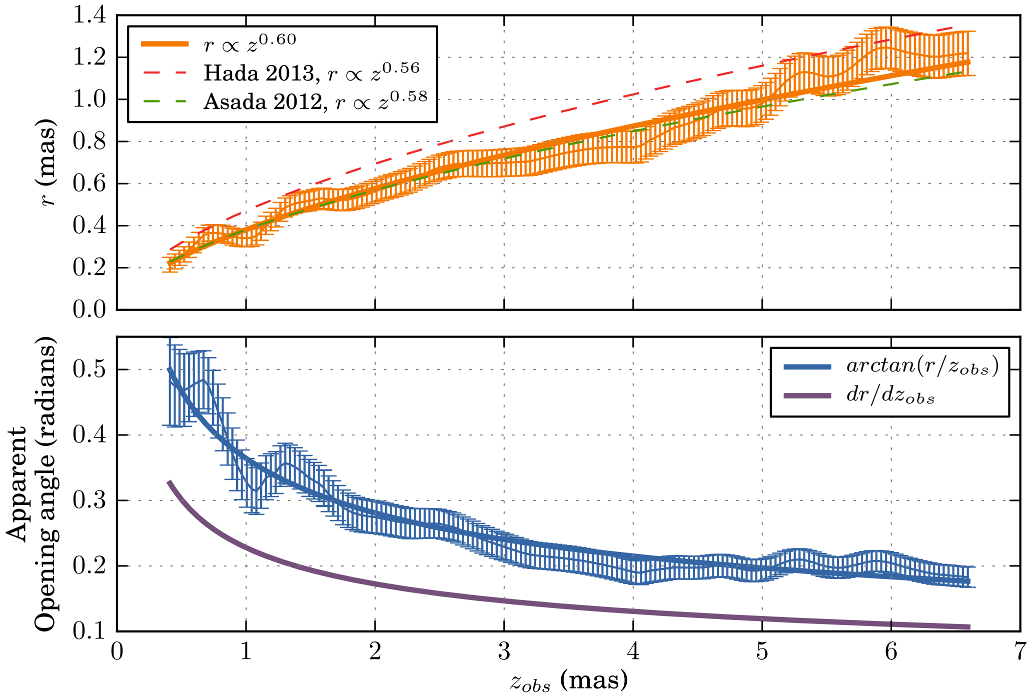

Figure 6.6: Jet radius (orange) and apparent opening angle (blue) of the jet in M87 with distance from the core. The power law fit of the jet radius is consistent with results obtained by Asada and Nakamura [2012] (green) and Hada et al. [2013] (red). The local opening angle (violet) is computed from the power law modeling of the jet radius.

(reduced $\chi^2 = 0.55$). This result is consistent with previous measurements made by Asada and Nakamura [2012] ($k = 0.58 \pm 0.02$) and Hada et al. [2013] ($k = 0.56 \pm 0.03$). As seen from Fig. 6.6, the expansion of the jet reveals an oscillatory pattern, most likely reflecting repeated over-collimation and over-expansion of the flow. The over-collimation is visible at $z_{\rm obs} \sim 1$, 1.9 and 4 mas, and the over-expansion manifests itself at $z_{\rm obs} \sim 0.75$, 1.4 and 2.6 mas, suggesting that the spatial period of these oscillations increases with the distance as $\sim z_{\rm obs}$. Oscillations of the jet width seen at distances $\gtrsim 5$ mas have a shorter period (0.5 mas) and might reflect the evolution of elliptical surface mode of K-H instability. The potential relevance of K-H instability for the jet shape is further supported by the fact that we do not observe any shock in the jet at the considered range. If these oscillations are of hydrodynamic nature, the pressure ratio between the jet and the external medium might be close to one[Daly and Marscher, 1988]. Oscillating expansion is also expected to be found in an expanding magnetized flow [Lyubarsky, 2009]. In the latter two cases, they are correlated with variations of the Lorentz factor of the flow, which is also observed in the jet in M87.

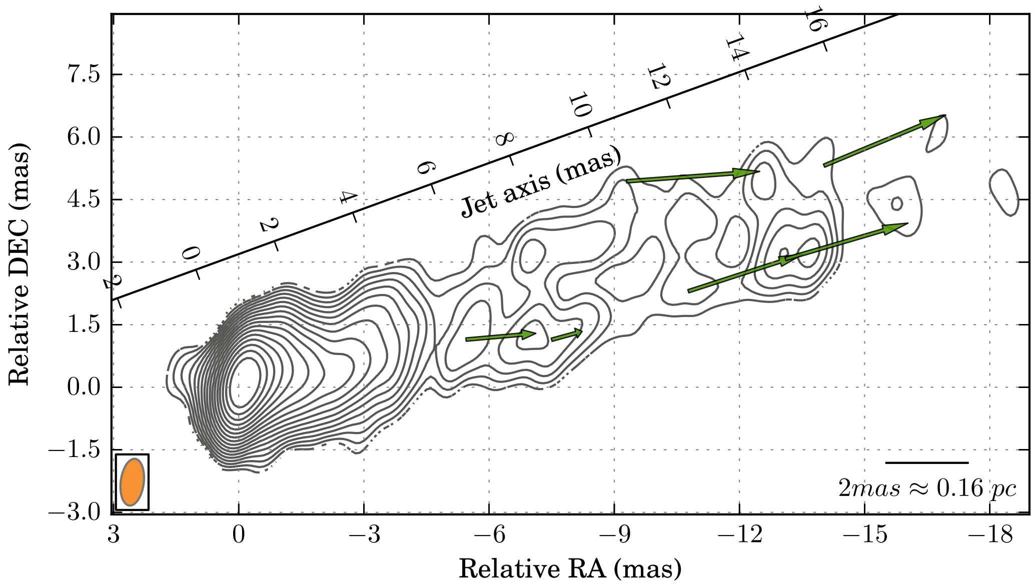

Figure 6.7: Two-dimensional displacements (green) of structural patterns detected using WISE analysis of 2 cm VLBA observations between 2000/04/07 and 2000/06/27. The tracks are overplotted on a stacked-epoch image of the jet.

6.3 WISE analysis of 2 cm VLBA observations

Between 1995 and 2010, the jet in M87 has been regularly observed as part of the MOJAVE project. The MOJAVE database contains 30 images of this jet, providing, on average, one observation every seven months. This cadence allows detection of jet speeds up to $\beta_{\rm app} \sim 1.6\,{\rm c}$ assuming a maximum detectable displacement of 4 times the beam size. In an analysis of this data using a model-fitting technique, Kovalev et al. [2007] detected only a slow, subluminal motion with a maximum speed $\beta_{\rm app} \sim 0.05\,{\rm c}$. This result is in contradiction with several other aspects of the jet, including the counter-jet flux density ratio, and so they suggested in their paper that the measured subluminal speed might represent pattern motions of either shocks or plasma instabilities. Using the WISE analysis, we can attempt to detect a faster speed from the MOJAVE data. The application of the SWD made for this purpose is performed using four scales, ranging from 0.4 mas (scale 2) to 3.2 mas (scale 5).

The interval between two epochs is generally too long to warrant detection of the fast velocity $\beta_{\rm app} \sim 2.5\,{\rm c}$ that has been measured in the 7 mm VLBA data. We concentrate therefore on the pair of observations separated by the shortest time interval. From the full database we selected two epochs (2000/04/07 and 2000/06/27) that matched this criteria. The result of applying the WISE algorithm to this pair of images is plotted in Fig. 6.7. We successfully detect fast relativistic speeds of $\beta_{\rm app} \sim 3\,c$–$3.5\,c$ for 4 different SSP in both the northern and southern limbs of the jet.

The result of this analysis is not definitive and further full-tracks VLBA observation at 2 cm with at most a 2 month cadence will be necessary to obtain a reliable velocity field. The analysis presented here suggests however that relativistic velocities can also be detected with VLBI observations made at a 2 cm wavelength.

6.4 Counter jet, viewing angle

The presence of a counter-jet in M87 jet has been suggested based on the structure detected in 2 cm VLBA maps [Kovalev et al., 2007]. A similar structural detail resembling a counter jet is also observed in the 7 mm maps [Ly et al., 2007; Walker et al., 2008]. At both frequencies, a number of tests were performed during the data reduction in order to ensure that the emission detected on the couter-jet side was not an artifact of the imaging procedure. The WISE analysis performed on the 7 mm data has revealed a component located in the counter-jet structure and moving outward with a speed similar to the one measured on the jet side at the same distance from the core. We will use this velocity measurement to constrain the viewing angle of the jet.

Relativistic Doppler beaming affects differently the flux density in the jet and the counter-jet. If the jet is seen at a viewing angle θ, the observed intensity ratio between the jet and counter-jet is given by:

$$R = \frac{I_{\rm jet}}{I_{\rm cjet}} = \left[\frac{\gamma_{cj}(1+\beta_{cj}\cos(\theta))}{\gamma_j(1-\beta_j\cos(\theta))}\right]^{2+\alpha} \tag{6.2}$$

with β_j, β_{cj} the intrinsic speed of the plasma in the jet and counter-jet respectively, γ_j, γ_{cj} the corresponding Lorentz factor and α the spectral index of the synchrotron radiation. In a recent publication, Hovatta et al. [2014] found $\alpha = 1$ for the radio emission on sub-parsec scales in the M87 jet.

We measure the intensity ratio R by taking a longitudinal profile of emission brightness along the jet axis. In order to reference properly the jet and counter-jet locations, special attention must be paid to identification of the position of the core. Because of synchrotron self-absorption, the observed location of the jet core does not correspond exactly to the true base of the jet [Lobanov, 1998b]. However, in the case of M87, Hada et al. [2011] found that the central engine of M87 and the radio core at 43 GHz are separated by a projected distance of only 41 ± 12 µas. Considering the position uncertainty of ~ 0.14 mas measured in the 7 mm VLBA images, we can safely assume the core to be the point of symmetry of the jet. In the profile obtained, flux density is measured at every pixel (0.035 mas; 1/8 of the beam size). The counter jet component is located in the northern limb of the counter jet. To preserve the symmetry, the jet to counter-jet intensity ratio is measured between the northern limb of the counter jet and the southern limb of the jet. The result is shown in Fig. 6.8.

We recall that the beam size is ~ 0.3 mas. It affects strongly the intensity measured close to the core, and hence we do not consider the measurements made within 0.4 mas from the core for this analysis. Between 0.4 mas and 0.8 mas, we

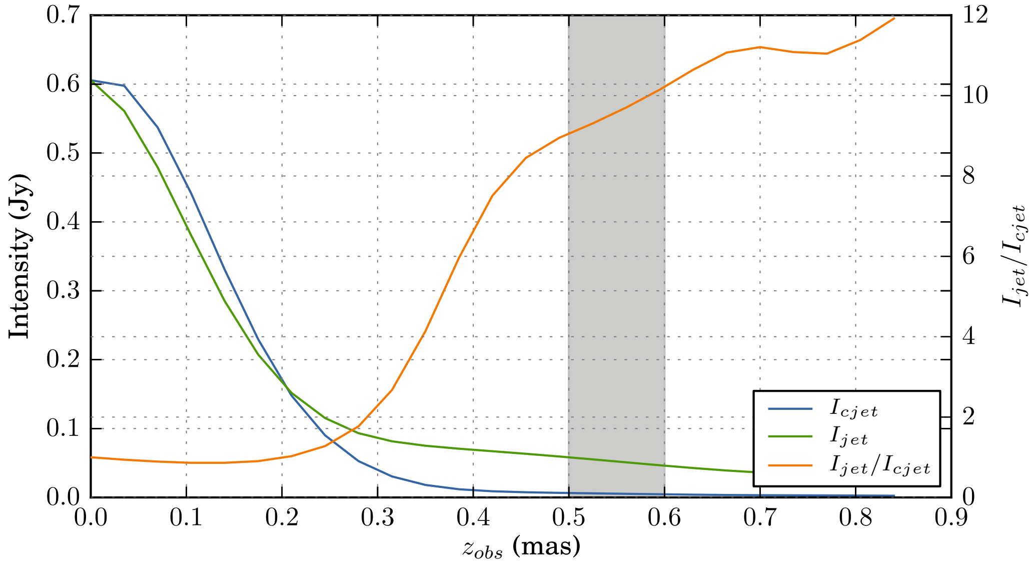

Figure 6.8: Jet (green) and counter jet (blue) intensity measured on a longitudinal slice of the jet and corresponding ratio (yellow). The gray area indicate the the location of the detected counter jet component.

observe a sharp increase of the jet to counter-jet intensity ratio from ∼ 7 to ∼ 11 which can be attributed to acceleration, thus supporting the results obtained by our WISE analysis. In this region, three components were detected on the jet side with apparent speeds ranging from $\beta_{\text{app}}^{\text{jet}} = 0.16 \pm 0.02\,c$ to $\beta_{\text{app}}^{\text{jet}} = 0.24 \pm 0.01\,c$. This is shown in Fig. 6.9. On the counter jet side, we measure an apparent speed of $\beta_{\text{app}}^{\text{cjet}} = 0.14 \pm 0.02\,c$. A first conservative constraint on the viewing angle can be determined using the maximum and minimum measured speed. In Fig. 6.10, we can see that the viewing angle and the intrinsic speed which reconcile both the apparent speed and the measured jet to counter-jet intensity ratio are in the range:

$$13° \leq \theta \leq 27°,\ 0.32 \leq \beta \leq 0.4 \tag{6.3}$$

This estimate assumes symmetry of the velocity and intensity between the jet and counter jet. It is however highly probable that different layers of the stratified jet are dominating the emission in the jet and the counter-jet sides. To take this possibility into account, we will now use both the apparent speed found in the jet and the speed measured in the counter jet. The counter-jet component C1 is detected at distances of 0.5–0.6 mas from the core (see Fig. 6.9). In this region, we measure a jet to counter-jet intensity ratio $R = 9.5 \pm 1.5$. On the jet side, we can use a more robust velocity measurement obtained from the stacked cross correlation analysis discussed in Sect. 6.2.2. Between 0.5 and 1 mas from the core, we measure a jet speed $\beta_{\text{app}}^{\text{jet}} = 0.21 \pm 0.04\,c$ in the southern limb of the jet. Then, using Eqs. 6.2, we obtain:

$$\theta = 17.2 \pm 3.3°,\ \beta_{\text{jet}} = 0.42 \pm 0.07,\ \beta_{\text{cjet}} = 0.33 \pm 0.06 \tag{6.4}$$

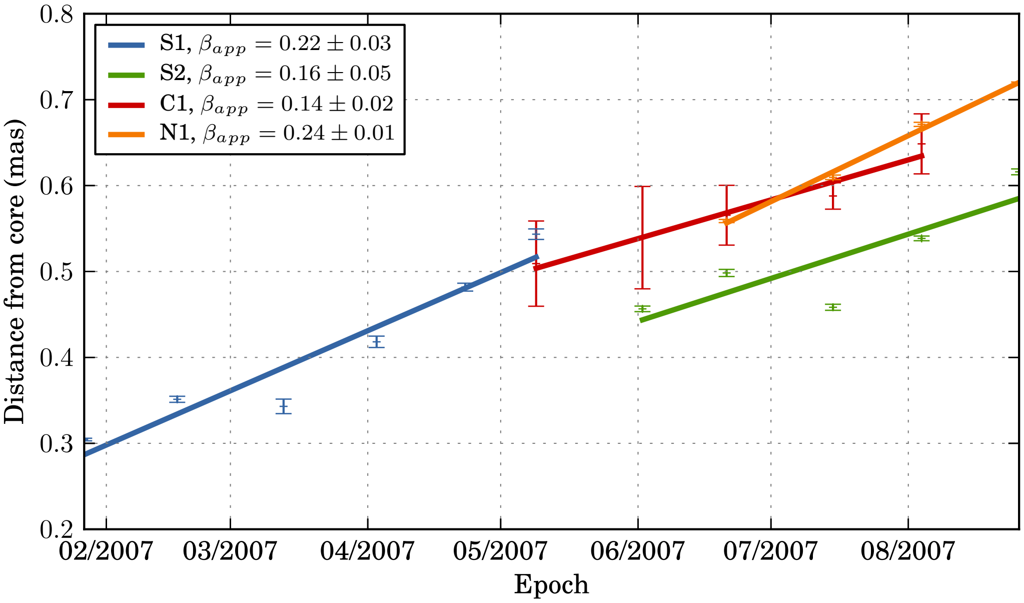

Figure 6.9: Core separations of the SSP that we tracked for at least 4 epochs over a 0.8 mas extent in both the jet and counter-jet direction. The jet components S1 (blue) and S2 (green) are detected in the southern limb of the jet, while the jet component N1 (orange) is detected in the northern limb of the jet. In the counter jet side, one component, C1 (red) is detected in the northern limb of the flow.

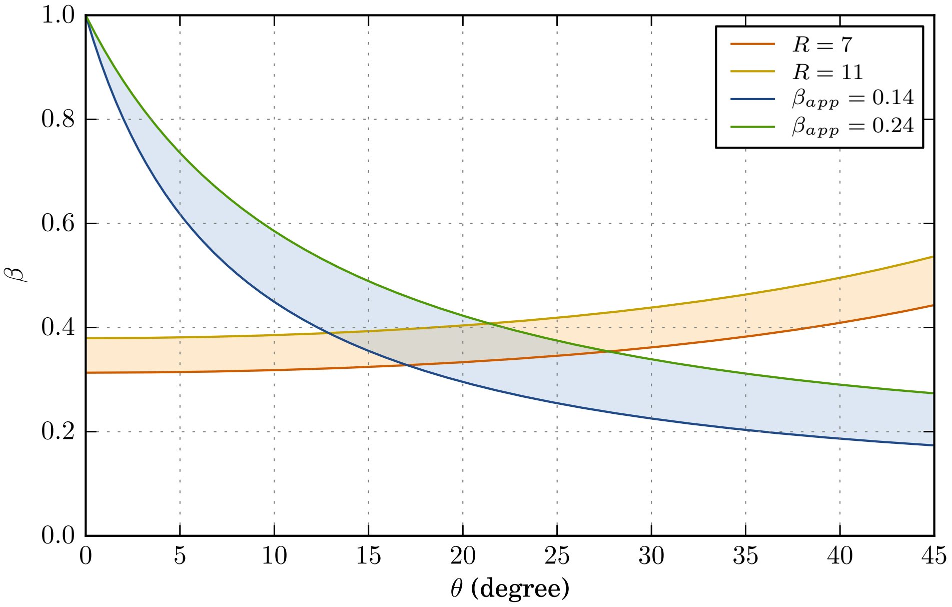

Figure 6.10: The jet viewing angle constraints obtained from the minimum and maximum jet to counter jet intensity ratio R and apparent velocity $\beta_{\rm app}$ measured at core separations between 0.4 and 0.8 mas.

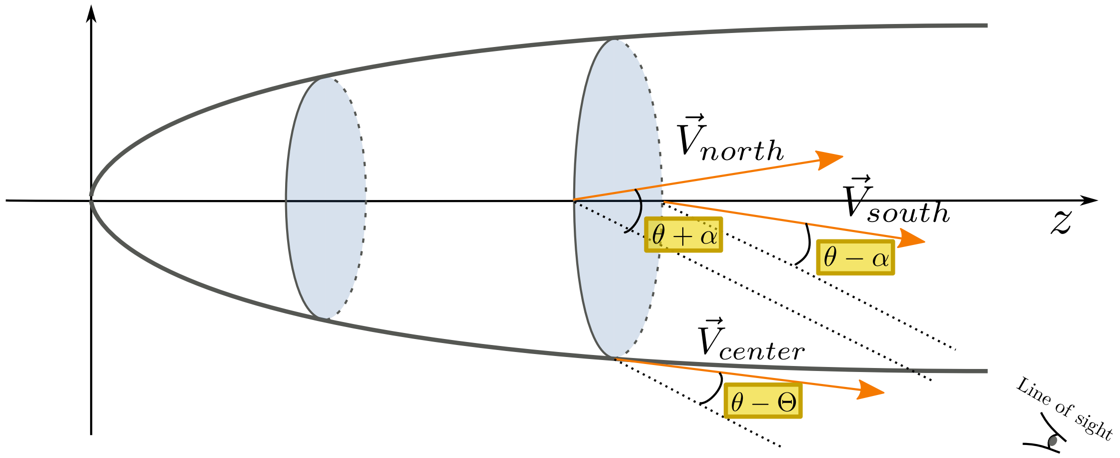

Figure 6.11: Schematic illustration of the effect of the jet rotation on the viewing angle in the three regions of the jet. In the northern and southern limb the traveling features are viewed with an angle to our line of sight $\theta_{\rm north} = \theta + \alpha$, $\theta_{\rm south} = \theta - \alpha$ respectively. In the central part of the jet, the opening angle needs to be taken into consideration, $\theta_{\rm center} = \theta - \Theta$.

The viewing angle agrees well with the maximum speed $\beta_{\rm app} \sim 6\,c$ measured at HST-1 which requires a viewing angle $\theta < 19°$.

6.5 Jet rotation

The stacked cross correlation analysis has revealed substantial difference between the velocities in the northern and southern limb of the jet. At core separations of 0.5–1.0 mas, the significance of this difference is $\sim 4\,\sigma$, while it is $\gtrsim 1.5\,\sigma$ for both the fast and slow velocity components detected between 1 and 4 mas.

This difference can be explained naturally by invoking jet rotation. In this framework, for a clockwise rotation of the jet, the SSP components moving along the northern limb of the jet would be viewed at a larger viewing angle, $\theta_{\rm jet} + \alpha$, while in the southern limb, the effective viewing angle would be reduced by α. This effect would not apply in the central limb of the jet, however velocities in this region are observed with a viewing angle reduced by the local opening angle Θ of the jet. This is illustrated in Fig. 6.11. The resulting viewing angle for the three regions can then be written as:

$$\theta_{\rm north} = \theta + \alpha,\ \ \theta_{\rm south} = \theta - \alpha,\ \ \theta_{\rm center} = \theta - \Theta \qquad (6.5)$$

If we assume that the flow has the same intrinsic velocity β in the three regions, we can determine α by solving a system of two equations with three unknowns: the

Table 6.3: Parameters for jet rotation estimated in region A (0.5 mas $\leq z_{\mathrm{obs}} \leq$ 1 mas) and region B 1 mas $\leq z_{\mathrm{obs}} \leq$ 3 mas for $\theta = 18°$.

Parameter	region A	region B slow	region B fast
$\alpha(degrees)$	7.5 ± 2.3	-9.7 ± 4.0	3.4 ± 1.7
β_p	0.55 ± 0.03	0.54 ± 0.10	0.924 ± 0.005
β_ϕ	0.08 ± 0.02	-0.09 ± 0.04	0.05 ± 0.03

Note: α – viewing angle modification due to jet rotation; β_p, β_ϕ – poloidal (axial) and toroidal (azimuthal) component of the speed of the flow.

viewing angle θ, the rotation angle α an the intrinsic speed β:

$$\begin{cases} \beta_{\mathrm{app}}^{\mathrm{north}} = \dfrac{\beta \sin(\theta + \alpha)}{1 - \beta \cos(\theta + \alpha)} \\ \beta_{\mathrm{app}}^{\mathrm{south}} = \dfrac{\beta \sin(\theta - \alpha)}{1 - \beta \cos(\theta - \alpha)} \end{cases} \tag{6.6}$$

In the case we can estimate the velocity in the central region, we have an additional equation:

$$\beta_{\mathrm{app}}^{\mathrm{center}} = \frac{\beta \sin(\theta - \Theta)}{1 - \beta \cos(\theta - \Theta)} \tag{6.7}$$

The intrinsic opening angle Θ can be estimated from the apparent opening angle measured in Fig. 6.6, using $\Theta = \Theta_{\mathrm{app}} \sin(\theta)$, and so, in this case, we have a complete set of equations which can be used to also estimate the viewing angle.

We use a least-square fitting technique to solve these equations. Robust estimates of the fit uncertainties are obtained from a Monte Carlo simulation: simulation with 1000 trials using the input parameters drawn from Gaussian distributions with a mean and standard deviation provided by the fitted value and a formal uncertainty for a given fitted parameter. The resulting output distribution of the fitted values also follows a Gaussian distribution, for each parameter of the fit, and we therefore determine the uncertainty of the fitted parameters by computing the standard deviation of this distribution.

The intrinsic speed can be decomposed into a poloidal (along the z and r axis, β_p) and toroidal (or azimuthal, β_ϕ) components:

$$\begin{aligned} \beta_p &= \beta \cos(\alpha) \\ \beta_\phi &= \beta \sin(\alpha) \end{aligned} \tag{6.8}$$

In the region 0.5 mas $\leq z_{\mathrm{obs}} \leq$ 1 mas (region A), the difference between the northern and southern limbs suggests a clockwise rotation. In the region 1 mas $\leq z_{\mathrm{obs}} \leq$ 3 mas (region B), the stacked cross correlation analysis has revealed two independent velocity components (see Sect. 3.5) which we will examine separately.

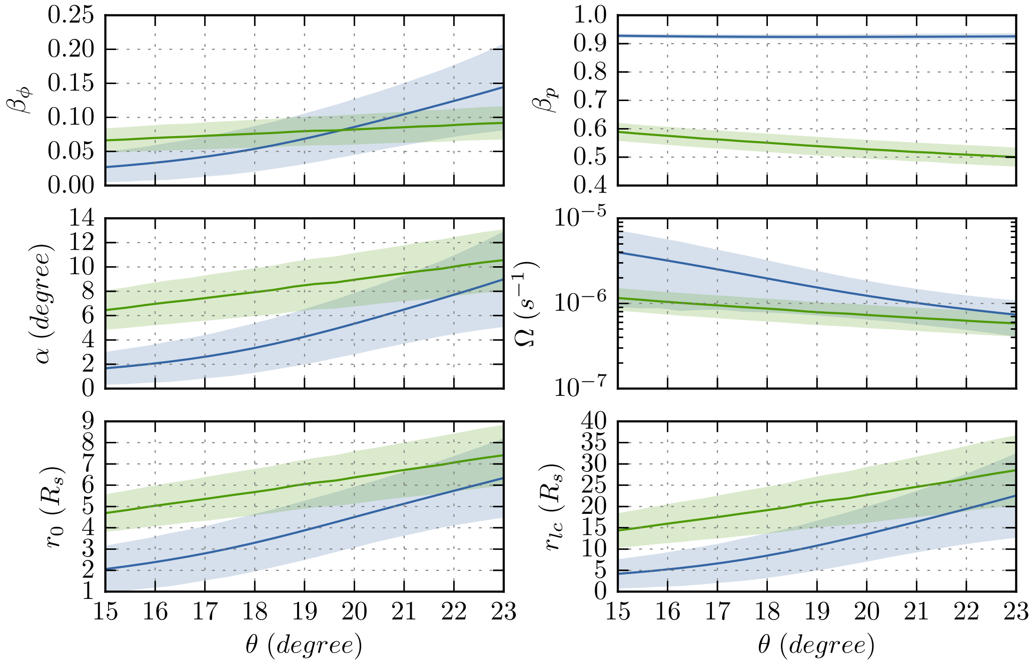

Figure 6.12: Parameters of the jet rotation obtained for the regions between 0.5 and 1 mas (green, region A) and between 1 and 3 mas (blue, region B) at different effective viewing angle θ.

The fast component is compatible with a clockwise rotation, and the additional measurement of the velocity in the central part of the jet using $\Theta_{\text{app}} = 0.15$ rad, allows us to obtain an estimate on the effective viewing angle:

$$\theta = 19.9 \pm 3.4^\circ \tag{6.9}$$

The slow component of region B is on the contrary consistent with a counterclockwise rotation. Substantial uncertainty in the speed in the central part (100% of relative uncertainty) does not permit estimating the viewing angle. The rotation parameters obtained for the three cases are summarized in Table 6.3 assuming a viewing angle $\theta = 18^\circ$ which is a compromise between estimates obtained here and in Sect 6.4.

There can be several explanations for the apparent rotation of the flow measured above. Plasma instability can produce pattern motions with a substantial azimuthal velocity component, as we have seen in the case of the jet in 3C 120 (Sect. 5.4). This might be the case for the slow component detected in region B, which has already been associated with instability pattern (see Sect. 3.5.

It is also possible that we observe an intrinsic, physical rotation of the flow. In the context of an MHD jet launched by magneto-centrifugal forces, the initial toroidal velocity is associated either with the Keplerian speed at the launching location in the accretion disk [Blandford and Payne, 1982] or with the spin of the central engine [Blandford and Znajek, 1977]. Conservation of the angular momentum will result in a slow decrease of the toroidal velocity beyond the light cylinder [Vlahakis, 2015]. The signature of such jet rotation has been previously reported in jets from young stellar objects (YSO), based on spectroscopic radial velocity analysis [Anderson et al., 2003; Choi et al., 2011], and it has been successfully associated with an MHD process, giving a constraint on the jet launching location. Jet rotation has so far not been directly detected in AGN jets. If our measured rotation is associated with the conserved angular momentum in the jet and if the jet is launched from the accretion disk via the Blandforf- Payne mechanism, its rotation direction should be the same as the rotation direction of the disk itself. Using spectroscopic HST measurements, Harms et al. [1994] found that the ionized gas associated with the accretion disk in M87 should rotate in a clockwise direction. This is indeed the observed rotation direction found in region A and for the fast component in region B. It is also interesting to note that the toroidal velocity measured closer to the central engine is greater than the one measured farther away, which is what the conservation of angular momentum predicts. We will now try to associate this observed rotation with MHD properties of the flow, following Anderson et al. [2003].

In the approximation of a cold steady MHD jet, the equation of conservation of specific energy (μ) and angular momentum (L) can be combined, eliminating B_ϕ and yielding the jet specific momentum [Anderson et al., 2003]:

$$J = \mu c^2 - \Omega L = \gamma c^2 - \Omega r c \gamma \beta_\phi \tag{6.10}$$

This quantity is conserved along a field line and can used to obtain an expression for the angular velocity, which remains constant along a given field line:

$$\Omega = \frac{c}{r\beta_\phi}\left(1 - \frac{J}{c^2\gamma}\right) \tag{6.11}$$

At the origin of the outflow, we can consider that β_ϕ is well below the speed of light ($\Omega r_0 \ll c$, $\beta_{\phi,in} \ll 1$), which gives $J \simeq \gamma_{in} c^2 \simeq c^2$. Knowing the toroidal velocity and Lorentz factor of the flow, Eq. 6.11 can be used to estimate the angular velocity. Assuming Keplerian rotation in the accretion disk, we can also obtain the launching location of a field line:

$$r_0 = \left(\frac{Gm}{\Omega^2}\right)^{1/3} \tag{6.12}$$

with m denoting the mass of the central engine.

The resulting parameters obtained for the region A and the fast component region B are summarized in Table 6.4. For completion, rotation parameters and angular velocity estimates for viewing angles between 15° and 23° are also provided in Fig 6.12. If regions A and B are both part of the same field line, the derived parameters should be equal. Although there is a difference between the angular velocities derived for the two regions it is below $1\,\sigma$ significance. The continuity of the flow between these two regions apparent in the VLBI map (Fig. 6.2) both in the southern and northern limb of the jet, indicate that region A and region B are part of the same field line.

Table 6.4: Angular velocity and launching location estimated in region A (0.5 mas $\leq z_{obs} \leq 1$ mas) and for the fast component of region B (1 mas $\leq z_{obs} \leq 3$ mas) for $\theta = 18°$.

Parameter	region A	region B fast
$\Omega(10^{-6}\ s^{-1})$	0.9 ± 0.3	2.0 ± 1.2
$r_0(R_s)$	5.7 ± 1.1	3.3 ± 1.3
$r_{lc}(R_s)$	19 ± 5	8 ± 5

In this case, the weighted average of the two measurement would give:

$$\begin{aligned} \Omega &= 1.12 \pm 0.34 \times 10^{-6} s^{-1} \\ r_0 &= 4.6 \pm 0.8\ R_s \end{aligned} \tag{6.13}$$

In the context of YSO jets, the validity of jet rotation measurements has been discussed. The stronger assumption here is that of a steaδy-state jet. Numerical simulations have shown that several disruptive effects, for instance shocks [Fendt, 2011] or plasma instability [Staff et al., 2015] can indeed affect the rotation signature. However, none of this effects seam to be important in our case: we base our rotation measurements on the fast component velocity which should be related to the inner layers of the jet and thus less affected by plasma instability. We remark also that no re-collimation shocks are observed in the VLBA images of the M87 jet and that the jet continues to be straight and steady up to Knot A at a de-projected distance of several kiloparsecs. We finally note that the location of the jet launching region that we derived from the angular velocity measurement is in the inner part of the accretion disk close to the Innermost Stable Circular Orbit (ISCO) of the black hole, which agrees well with the result from numerical simulations of magnetized relativistic jets [Meier et al., 2001; Komissarov et al., 2007].

6.6 Jet collimation and acceleration

Analytical and simulation works on MHD jets have shown that collimation and acceleration are related and occur on the same spatial scales in relativistic flows. Most of the flow acceleration results from the so-called “magnetic nozzle” effect [Li et al., 1992; Vlahakis, 2015]. This effect is at work whenever the flow collimates so that the distance between streamlines increases faster than the radius of the flow. This results in a small deviation of the local poloidal magnetic field from the mean magnetic field which drives the acceleration. Because this deviation is small, the fluid is only slowly accelerated by a small residual force and the acceleration zone can extend over a large distance. Both numerical simulations and observational evidence suggest that jet acceleration continues up distances of 10^3–10^4 R_s [Vlahakis and Königl, 2004].

The ideal MHD equations may be written as a set of two non-linear differential equations describing the equilibrium of forces perpendicular (Grad- Shafranov or transfield equation) and parallel (Bernoulli equation) to the magnetic surface. A complete analytic solution of these equations can be obtained only in specific, restricted cases, (e.g. self-similar solutions). Approximations can also be made to simplify the equations in specific cases. The force free approximation is often used to describe jets in the near zone, inside the light cylinder ($r \lesssim r_{lc}$) [Blandford and Znajek, 1977]. At larger radial separations, different sets of approximations may need to be used.

In a recent paper, Lyubarsky [2009] obtained asymptotic solutions in the case of a cold, ideal, Poynting flux dominated ($\sigma \gg 1$) MHD jet in the far-zone ($r \gg r_{lc}$). Different set of approximations are used depending on the decay of the external pressure confining the jet. AGN jets can be confined by a variety of forces including gas pressure from ambient medium, ram pressure from the outer, subrelativistic wind and the stress of a magnetic field anchored in the disk. In general, the evolution of the confining pressure can be approximated by a power law:

$$P_{ext} = P_0 z^{-\kappa} \tag{6.14}$$

Depending on κ, Lyubarsky [2009] found different scaling relations for the jet shape and acceleration:

- if $\kappa < 2$, the jet is in the so-called *equilibrium* regime. The residual of the hoop stress and the electric force are counterbalanced by the pressure of the poloidal magnetic field so that at any distance from the source, the structure of the flow is the same as the structure of an appropriate cylindrical equilibrium configuration. The jet shape is given by a power law $r \propto z^k$, with $k = \kappa/4$ converging to a cylindrical shape at large distance. The acceleration is linear, meaning that it is proportional to the jet radius: $\gamma \propto r \propto z^k$.

- if $\kappa > 2$, the jet is at first in a regime similar to the above equilibrium regime. The jet shape is parabolic $r \propto z^k$ and the acceleration is linear. At some distance, the pressure of the poloidal magnetic field become small so that the flow could be viewed as a composition of coaxial magnetic loops. This regime is called *non-equilibrium*. The flow reaches ultimately a conical shape and the acceleration is determined by the curvature of the flow, $\gamma \propto z^{(\kappa-2)/2}$.

We found in Sect. 6.2.3 that the evolution of the cylindrical cross-section of the jet in M87 is described by a power law with an index $k \sim 0.56$–0.60. Asada and Nakamura [2012] found that the M87 jet then reaches a conical shape at kiloparsec scales, similarly to the $\kappa > 2$ case above. To determine the acceleration profile, we compute the Lorentz factors for the velocity field obtained from WISE analysis at 7 mm (Sect. 6.2.1) and 2 cm (Sect. 6.3), using a viewing angle $\theta = 18°$. We complement the radio measurements with the optical and radio velocities determined

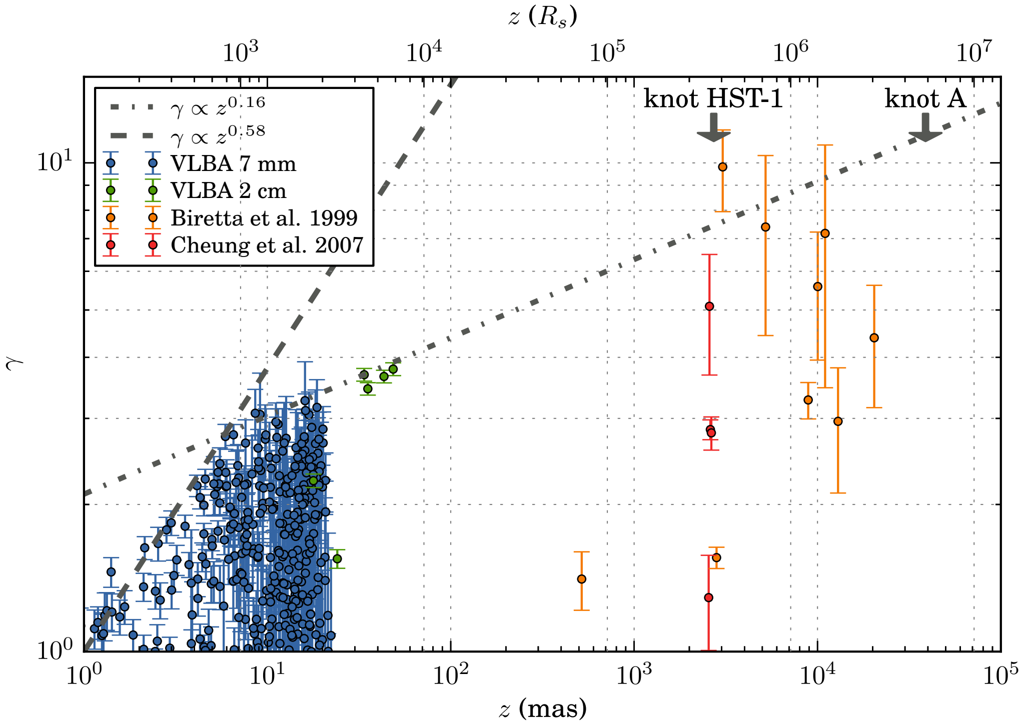

Figure 6.13: Acceleration profile of the jet in M87. We plot the Lorentz factor measured from WISE analysis of VLBA images at 7 mm (blue), 2 cm (green), from Cheung et al. [2007] using VLBA at 1.7 Ghz (red), and from optical images using HST[Biretta et al., 1999] (orange). Two regimes are found with a linear acceleration up to $z \sim 10^3 R_s$, followed by a slow acceleration up to HST-1.

in the kiloparsec structure of the jet [Cheung et al., 2007; Biretta et al., 1999; Giroletti et al., 2012]. The combined evolution of the Lorentz factor plotted in Fig. 6.13 indicates two different regimes for the acceleration. The acceleration is at first linear with $\gamma \propto r \propto z^{0.58}$ up to $z \sim 8$ mas ($\sim 10^3 R_s$), and then it becomes weaker, with $\gamma \propto z^{0.16}$, agreeing well with the measurements obtained at larger scales, up to the knot HST-1. The jet appears to enter the non-equilibrium regime ($\kappa > 2$) on these scales. One must however be cautious about this interpretation. The scaling relations obtained for the $\kappa > 2$ case are valid when the jet shape becomes approximately conical. However there is some indication that the jet in M87 transits to a conical shape only at $z \sim 10^3$ mas. An alternative explanation for this slower acceleration is early saturation of Poynting flux conversion. In this case the conversion would be nearly complete at $z \sim 10^3 R_s$, and acceleration would then continue slowly until full conversion is achieved.

In the following, we will investigate these two possibilities using the velocity profile of the fast components of the jet flow that we identified in Sect. 3.5. This velocity profile is obtained by computing the mean of the fastest 10% of the speeds measured within individual bins of 0.1 mas in size. To improve the robustness of the velocity determination, resampling is done using bins of 0.2 mas for $0.4 \geq z_{\text{obs}} < 2$

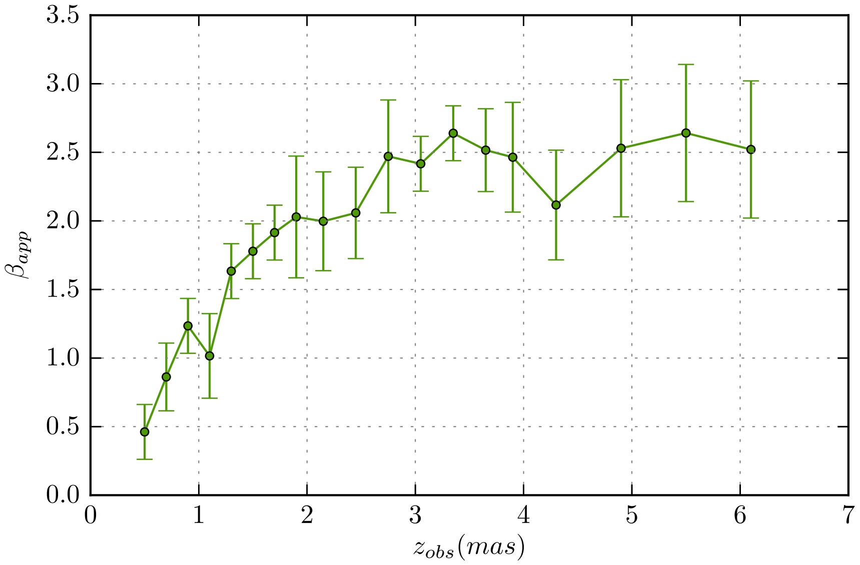

Figure 6.14: Apparent velocity of the investigated field line.

mas, 0.3 mas for $2 \geq z_{\mathrm{obs}} < 4$ mas and finally 0.6 mas for $z_{\mathrm{obs}} \geq 4$ mas. The result is plotted in Fig. 6.14. We associate these measured velocities with a field line in the jet with the collimation profile determined in Sect. 6.2.3.

Under this assumption, the measured velocities can be associated with a single field line (located on a single magnetic flux surface), assuming $\Omega =$ const. In this case we can conveniently use variables scaled to the light cylinder radius:

$$R = \frac{\Omega r}{c}, Z = \frac{\Omega z}{c} \tag{6.15}$$

6.6.1 Asymptotic relations in the far-zone Poynting dominated approximation

In the cold ideal MHD assumption, one can further simplify the interpretation framework by considering the additional approximation of a Poynting dominated jet ($\sigma \gg 1$) in the far-zone ($R \gg 1,\ \gamma \gg 1$)[Lyubarsky, 2009].

In the *equilibrium* case and for $\kappa > 2$ one can obtain the following relations for the jet shape:

$$R = \sqrt{\frac{2-\kappa}{\pi}} \left(\frac{3\,Z^{\kappa}}{\beta}\right)^{1/4} \left[\frac{1}{C_1}\cos^2(S) + C_1\left(C_2\cos(S) + \frac{\pi}{2-\kappa}\sin(S)\right)^2\right]^{1/2} \tag{6.16}$$

$$S = \frac{2\sqrt{\beta}}{2-\kappa} Z^{1-\kappa/2} - \frac{4-\pi}{2-\kappa}\frac{\pi}{4} \tag{6.17}$$

with β_{plasma}, describing the ratio of the plasma pressure to the magnetic pressure:

$$\beta_{\mathrm{plasma}} = \frac{6\pi p_0}{B_0^2}, \tag{6.18}$$

Table 6.5: Best fit parameters reproducing the observed acceleration and collimation using asymptotic relations in the far-zone of the Poynting dominated approximation.

Parameter	Best fit
$z_{\text{obs}}^{\text{break}}(mas)$	1.7 (fixed)
$\Theta_{\text{app}}^{\text{break}}(degrees)$	10.5 (fixed)
k	0.588 ± 0.005
$\Omega(10^{-6}\ s^{-1})$	0.86 ± 0.02
β_{plasma}	79 ± 12
$\theta(degrees)$	19 ± 4
C_1	0.10 ± 0.03
C_2	-1 ± 2
a_γ	0.63 ± 0.13
$\phi_\gamma(degrees)$	35 ± 7

and B_0 and p_0 giving the characteristic magnetic field and the external pressure at the light surface, respectively.

The Lorentz factor can also be obtained, depending on the equilibrium regime:

$$\gamma = \begin{cases} R & \text{(equilibrium)} \\ \dfrac{Z^{(\kappa-2)/2}}{\sqrt{\beta}\Theta_{\text{app}}^{\text{break}}} & \text{(non-equilibrium)} \end{cases} \tag{6.19}$$

with $\Theta_{\text{app}}^{\text{break}}$ describing the local opening angle at the transition between the two regimes. We assume $\Theta_{\text{app}}^{\text{break}} = 0.182$ using Fig. 6.6.

The Lorentz factor and the collimation profile are fitted simultaneously using a Levenberg-Marquardt least-squares minimization routine, and uncertainties in the fitted parameters are obtained using the standard error obtained from the estimated covariance matrix.

Some modifications to the Lorentz factor were necessary for the fit to converge. An additional scaling, α_γ, was introduced modifying the Lorentz factor so that: $\gamma^\star = a_\gamma \gamma$, and the Lorentz factor was phase shifted along the axial coordinate of the jet by $S_\gamma^\star = S + \phi_\gamma$, in order to be able to account for the fact that the maxima and minima found in the collimation profile do not correspond exactly to the maxima and minima found in the Lorentz factor profile.

All parameters were allowed to vary freely, including the viewing angle θ and the angular velocity Ω. The best fit obtained under these conditions has a reduced $\chi^2 = 0.24$. In detail, this corresponds to $\chi_r^2 = 0.22$ and $\chi_\gamma^2 = 0.34$ for the collimation and Lorentz factor fit respectively. We recall that $\chi_r^2 = 0.55$ was found by modeling the collimation profile as a simple power law. This indicates an improvement, by a factor of ~ 2, of the quality of the fit provided by the Poynting flux approximation for the jet collimation profile.

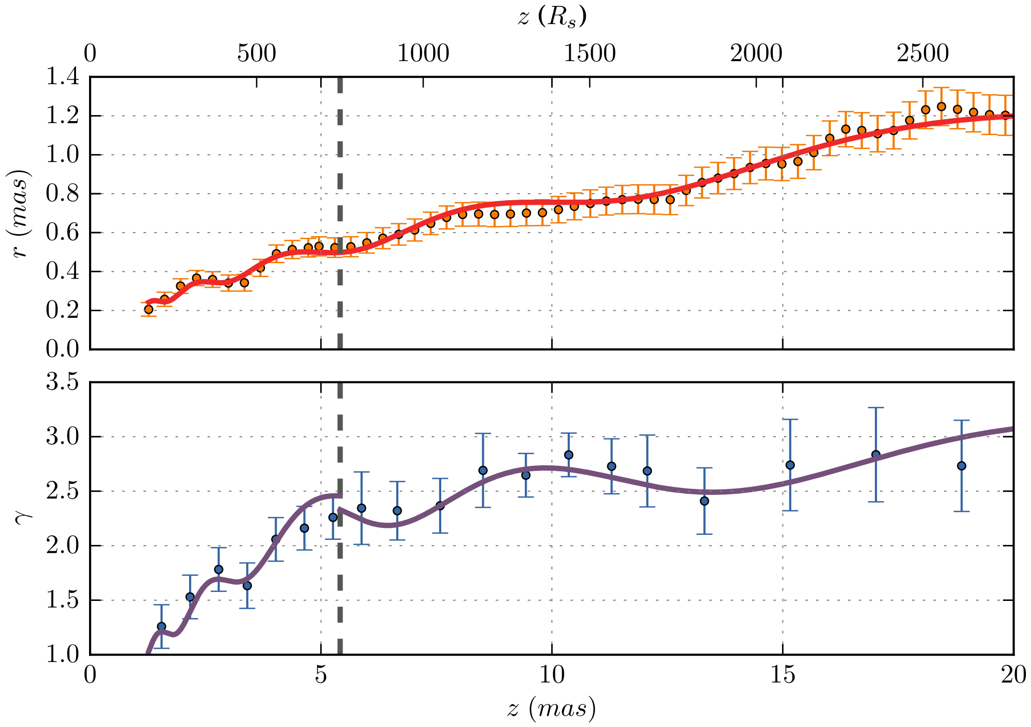

Figure 6.15: Best fit for the observed acceleration (blue) and collimation (orange) of the jet in M87. Viewing angle and angular velocity are determined from the fitting.

The best fit is plotted in Fig. 6.15, and the derived parameters of the model are summarized in Table 6.5. It is remarkable that the viewing angle and the angular velocity agree, within the uncertainties, with the respective values found from the analysis of the counter jet (Sect. 6.4) and the jet rotation (Sect.3.5). The oscillations in both the jet width and the Lorentz factor are also particularly well reproduced. The physical significance of ϕ_γ and a_γ is however unclear. A possible reason for the phase shift is that the measured Lorentz factor may come from a streamline slightly inside the measured jet shape. In this case the maxima in the Lorentz factor will be offset from the maxima in the jet width, with a shift proportional to the jet radius [Norman et al., 1982]. The explanation for the need of the scaling factor, α_γ, may be found in the assumption made by Lyubarsky [2009] to derive the scaling relations using a constant angular velocity for all field lines. This assumption is usually valid only in the case of a jet launched from the magnetosphere (Sect. 2.1). In the case of disk launching, we expect differential rotation and Tchekhovskoy et al. [2008] found that $\gamma < R$ under these conditions. We shall recall here also that the relations were derived with assumptions which are only partially valid in our case, specifically $R \gg 1$ and $\gamma \gg 1$ and this might also explain the need to scale the Lorentz factors determined from the observed velocity field.

It is still unclear however if the slow acceleration after $z_{\rm break}$ is due to the non-equilibrium regime or saturation. A change of regime should be associated with a change in the collimation profile, with the jet becoming conical in the case $\kappa > 2$. The fact that the collimation profile stays parabolic up to a de-projected distance $z \sim 10^3$ mas suggests that jet acceleration is indeed quenched, and we will now investigate this case by solving the Bernoulli equation.

6.6.2 Wind solutions

Solving simultaneously the full transfield and the Bernoulli equations is only possible in a restrictive number of cases. The transfield equation will determine the shape of the field lines while the Bernoulli equation governs the acceleration of the flow. Assuming a flow shape, it is then possible to solve only the Bernoulli equation [Camenzind, 1986; Fendt and Ouyed, 2004; Toma and Takahara, 2013]. The resulting solution is called the wind solution. It is not strictly an exact MHD solution, and one should be careful not to over-interpret it. However it can be used in some specific case, *e.g.*, for investigating the acceleration efficiency, or in our case, the acceleration profile.

In the context of an ideal cold MHD jet, the poloidal and toroidal velocities can be written as follows:

$$\begin{aligned} \beta_p &= \frac{R^2 B_p(R)}{\eta(\mu-\gamma)}\left(1 - \frac{1}{R^2}\left(1 - \frac{\gamma_{in}}{\gamma}\right)\right) \\ \beta_\phi &= \frac{1}{R}\left(1 - \frac{\gamma_{in}}{\gamma}\right) \end{aligned} \tag{6.20}$$

where B_p is the poloidal magnetic field, μ is the total (magnetic + matter) specific energy, γ_{in} and η are the Lorentz factor and the distribution of mass flux at the inlet of the flow, respectively. The quantity η is a field line constant and it is given by the following equation:

$$\eta = \frac{4\pi\gamma\rho_0\beta_p c^2}{B_p} \tag{6.21}$$

with ρ_0 describing the rest-mass density. We also define the ratio of the Poynting to the matter energy flux, also called magnetisation parameter, as:

$$\sigma = \frac{\mu-\gamma}{\gamma} \tag{6.22}$$

The Bernoulli equation is obtained from:

$$\beta_p^2 + \beta_\phi^2 + \frac{1}{\gamma^2} = 1 \tag{6.23}$$

and can be reduced to a quartic equation for γ. To resolve it, one has to prescribe a model for the poloidal magnetic field B_p, which turns into a model for the flux function.

Toma and Takahara [2013] recently derived a set of models for B_p based on a realistic flux function $\Psi(r, z)$:

$$Z + \zeta(\psi) = A(\psi)(R - \varpi(\psi))^{a(\psi)} \tag{6.24}$$

where $\psi = \Psi/\Psi_0$. This function describes parabolic field lines appropriate for M87. The poloidal magnetic flux is then obtained recalling that $B_p = (\nabla\Psi \times \phi)/r$:

$$\begin{aligned} B_p(R) =& \frac{\Psi_0}{R^2}\left(\frac{\zeta'}{Z+\zeta} - \frac{A'}{A} - a'\ln(R-\varpi) + \frac{a\varpi'}{R-\varpi}\right)^{-1} \\ & \frac{R}{R-\varpi}\sqrt{\left(\frac{R-\varpi}{Z-\zeta}\right)^2 + a^2} \end{aligned} \tag{6.25}$$

At $r \lesssim r_{lc}$, the true shape of the field lines will probably deviate from the shape derived from Eq. 6.24 as it gets anchored into the accretion disk or the magnetosphere. However, the approximation will be valid in the region we are investigating.

In our case of interest and using $\theta = 18°$ and $\Omega = 10^{-6}$, we have $\zeta = \varpi = 0$, $A = 3.7$ and $a = 1/k = 1.73$, corresponding to the parabolic shape obtained by [Asada and Nakamura, 2012]. We also adopt $\gamma_{in} = 1$.

With the assumptions specified above, the Bernoulli equation admits 7 unknowns: μ, η, a', A', ζ', ϖ' and Ψ_0, resulting in over determination of the problem. We can however isolate some parameters and treat different cases separately. We define three models:

- **Model 1**: $a' \neq 0$, $A' = 0$,$\zeta' \neq 0$, $\varpi' = 0$,
- **Model 2**: $a' \neq 0$, $A' = 0$,$\zeta' = 0$, $\varpi' \neq 0$,
- **Model 3**: $a' \neq 0$, $A' \neq 0$,$\zeta' = 0$, $\varpi' = 0$,

The Bernoulli equation has two singularities at the Alfvénic point (AP) and at the fast magnetosonic point (FMP). The wind solution in which γ is growing towards infinity has to pass through both the AP and the FMP. Practically, the Bernoulli equation, being quartic for γ, admits four roots. To be valid,the wind solution needs to pass smoothly from one root to the other crossing the singularities. This adds a constraint, and for a given $B_p(R)$ and η, a unique value of μ corresponds to a valid wind solution.

A Nelder-Mead least-squares minimization routine is used to fit the Bernoulli equation to the measured Lorentz factor evolution. Within each iteration of the fitting algorithm, μ is determined so as to maintain a valid wind solution.

Fig. 6.13 suggests that the velocities measured at HST-1 and measured from 7 mm VLBA images originate from the same field line. To test this hypothesis we also fit the speed measured at HST-1 by Giroletti et al. [2012], assuming $r_{\text{HST-1}} = 26$ mas [Asada and Nakamura, 2012]. This addition does not affect the reduced χ_2 of the fit, thus supporting our hypothesis.

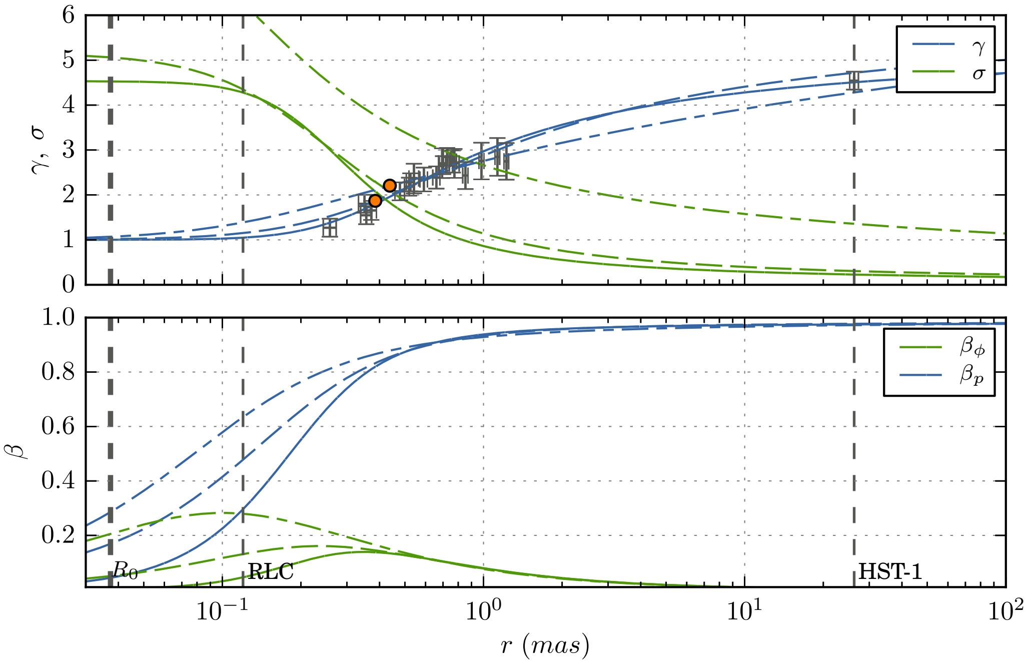

Figure 6.16: Wind solution for model 1 (solid line), model 2 (dashed line) and model 3 (dash-dotted line) of the flux function that reproduces the best observed acceleration (black points). The upper panel shows the total energy (blue) and magnetization parameter (green). The lower panel shows the toroidal (green) and poloidal (blue) velocity. The location of the fast magnetosconic point is indicated by an orange dot.

Satisfactory fits were obtained for Models 1 and 2, however we could not obtain a reasonable fit using Model 3. In order still to be able to analyze the impact of A' on the solution, we assigned a small value of ϖ' in this model. The results for the three models are summarized in Table 6.6 and corresponding wind solutions are plotted in Fig. 6.16.

Model 1 and 2 reproduce the best the measured acceleration. The jet parameters derived with these models are also similar. In the case of model 3, a higher value of μ was required, and the resulting conversion from Poynting to kinetic energy is slower. In all three cases the Alfvénic point is found to be located close to the light cylinder, in agreement with exact self-similar solutions [Vlahakis and Königl, 2004]. The fast magnetosonic point is located at $r \sim 0.4$ mas, corresponding to $z \sim 1$ mas, and in agreement with the expectation that $\gamma_{\mathrm{FMP}} \simeq \mu^{1/3}$.

A true solution would certainly be a combination of the three models, since we do not know the exact shape of the field line close to the central engine, and thus we cannot reconstruct the initial acceleration, which might help discriminate between the models, as suggested by the divergence of the poloidal and toroidal velocities observed in Fig. 6.16. Our result however strongly favors a moderate value of μ with an efficient transformation of Poynting to kinetic energy.

Table 6.6: Parameters for the wind solution that best reproduces the observed acceleration for the three models of the flux function.

Parameter	Model 1	Model 2	Model 3
χ^2	0.41	0.62	1.6
μ	5.5	6.2	10.1
L ($\times 10^{23}$) $[SI]$	4.1	4.7	8.2
FMP (R_{lc})	3.23	3.23	3.65
AP (R_{lc})	0.92	0.92	0.95
B_0/η $[SI]$	1.5	2.9	7.8

6.7 Discussion

6.7.1 Stratification

In Sect. 3.5, we have identified two velocity components using the stacked cross correlation. The slow component reflects either the pattern speed of a plasma instability or the bulk speed of an outer slower wind. The observed counter rotation of this component suggest that it is more likely related to instability. The fast velocity component has been successfully associated with the bulk speed along the magnetic field line connected to the observed jet shape, and we have obtained a wind solution for it. The inner deboosted part of the jet can be associated with an even faster speed along a field line located closer to the jet axis.

The limb brightened structure found at all scales might be explained by the combination of an enhanced magnetic field at the jet edge and a faster speed close to the jet axis. From analysis of the kiloparsec scale structure of the jet in M87, we can infer that indeed the inner part of the jet, dominant at optical wavelength as suggested by Perlman et al. [1999b], is consistently faster than the outer part, dominant at radio wavelength. Biretta et al. [1999] found apparent speeds as fast as $\beta_{\mathrm{app}} \sim 6$ c. Using $\theta = 18°$, this correspond to $\gamma \gtrsim 10$. We measure in a stacked-epoch image of the jet in M87 an intensity ratio between the inner part (the spine) and the edge (the sheath) $R \sim 0.5$ for $z_{\mathrm{obs}} \sim 3$ mas. Assuming $\gamma_{\mathrm{sheath}} \sim 2.7$, we can calculate the Lorentz factor of the spine necessary to reproduce the observed intensity ratio using:

$$R = \frac{I_{\mathrm{spine}}}{I_{\mathrm{sheath}}} = \frac{\gamma_{\mathrm{sheath}}(1-\beta_{\mathrm{sheath}}\cos(\theta))}{\gamma_{\mathrm{spine}}(1-\beta_{\mathrm{spine}}\cos(\theta))}^{2-\alpha} \tag{6.26}$$

Solving this equation, we find $\gamma_{\mathrm{spine}} \sim 6.5$. If we associate this spine with the optical measured speed, and using $\gamma_{\mathrm{spine}} \sim 10$ at HST-1, we can find a wind solution that would satisfy these observations.

Starting with the best solution found in Sect. 6.6.2 using Model 1, we set now $\Omega = 2.5 \times 10^{-6}$ corresponding to a field line anchored to a launching location closer

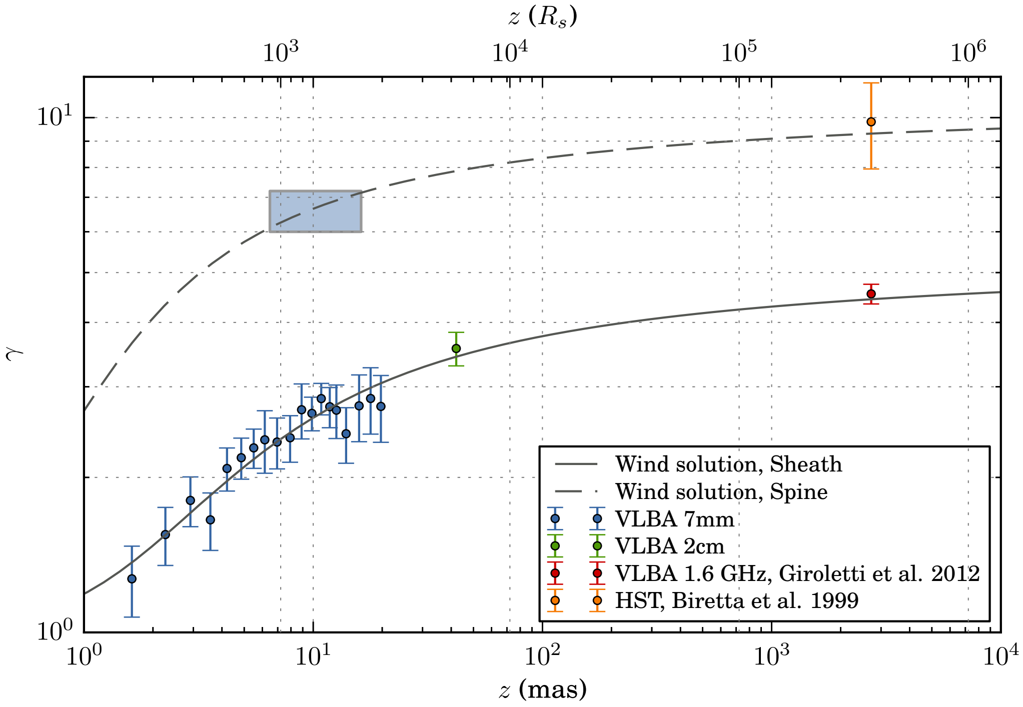

Figure 6.17: Wind solution for the spine (dashed line) and the sheath (solid line). The solution for the spine fits well the inferred velocity of the deboosted structure observed in the 7mm VLBA maps (blue box) and the velocity observed at HST-1 in the optical band. The solution for the sheath fits the fast velocities measured in the 7 mm and 2 cm VLBA data, and at HST-1 in the radio band.

to the ISCO ($r_0 \sim 2.8\ R_s$), $\mu = 11$, and $A = 6.6$ so that $r_{\mathrm{spine}}(z) = 0.5 r_{\mathrm{sheath}}(z)$. We then look for a valid wind solution that would fit the two estimates of the Lorentz factor of the jet spine. The result, plotted in Fig 6.17, indicates strongly that while the sheath field line can be associated with the velocity measured in the radio at HST-1, the spine field line connects well the inferred velocity of the deboosted structure in VLBA 7 mm maps and the velocity measured at HST-1 in the optical band.

6.7.2 Launching mechanism

Agreement between the estimates of the angular velocity obtained from the observed jet rotation, the jet acceleration and the jet collimation indicates that the sheath field line has an angular speed $\Omega \sim 10^{-6}\ \mathrm{s}^{-1}$. This parameter can be used to discriminate between the two major mechanisms that operate during the jet launching. In the Blandford and Payne (BP) model, the jet is launched from the accretion disk and the field line angular velocity depends on the distance from the black hole at which this field line is anchored. If we assume a Keplerian rotating accretion disk, this corresponds to $r_0 \sim 5\ R_s$. In the Blandford and Znajek (BZ) mechanism, the angular velocity depends on the spin of the central black hole a. Following Tchekhovskoy

[2015], the black hole angular speed is:

$$\begin{aligned} \Omega_H &= \frac{ac}{2r_H} \\ r_H &= \frac{R_S}{2}(1+\sqrt{1-a^2}) \end{aligned} \tag{6.27}$$

One can then obtain the corresponding field line angular speed:

$$\Omega_F \simeq 0.5\Omega_H \tag{6.28}$$

Using 1 mm VLBI observations, Doeleman et al. [2012] estimated the spin of the black hole in M87 $a \sim 0.6$ based on the measure of the size of the smallest resolvable structure, identified as the ISCO. This corresponds to $\Omega_F = 2.75 \times 10^{-6}$ s^{-1} and is a factor 3 times larger than the angular velocity that we measured. A BP mechanism would better account our observation, but a BZ launching cannot be firmly discarded owing to the uncertainty of this measurement. Nevertheless, the wind solutions obtained for the sheath and the spine imply $\mu_{\rm spine} \gtrsim \mu_{\rm sheath}$, which is a characteristic of differential rotation law as found both analytically and in simulation [Lyubarsky, 2009; Komissarov et al., 2007]. This favors therefor a disk launching at least for the sheath.

6.7.3 Poynting to kinetic energy conversion

The wind solution obtained for the sheath suggests a total energy at the base of the jet $\mu \sim 6$–10. In the first two models described in Sect.6.6.2, the conversion between magnetic and kinetic energy is efficient and the equipartition condition $\sigma \sim 1$ is achieved at:

$$r_{eq} \sim 1.5 \text{ mas} \sim 10\ r_{lc} \sim 200\ R_s \tag{6.29}$$

corresponding to

$$z_{eq} \sim 20 \text{ mas} \sim 2800\ R_s \tag{6.30}$$

In an MHD simulation of AGN jets, Komissarov et al. [2007] found nearly consistently, for different analyzed models, $r_{eq} \sim 30\ r_{lc}$. Considering their choice of total energy $\mu \sim 18$, our results for Model 1 and Model 2 are qualitatively similar to the results of Komissarov et al. [2007].

The conversion of Poynting to kinetic energy is less efficient for our Model 3, and equipartition is only achieved there at $r_{eq} \sim 40$ mas $\sim 300\ r_{lc}$. However this model does not reproduce our observed acceleration as well as the first two models.

6.7.4 Estimate of mass-loss rate

The mass-loss rate corresponds to the amount of matter extracted from the accretion disk and loaded into the jet. It can obtained from:

$$\dot{M} = \frac{\eta \Psi_0}{4c} \tag{6.31}$$

The wind solution describing the acceleration of the sheath requires $B_0/\eta \sim 2$–10, with B_0 describing the characteristic magnetic field at the light cylinder. The mass loss rate can then be estimated recalling that $\Psi_0 \sim B_0 r_{lc}^2$:

$$\dot{M} \sim \frac{\eta B_0 r_{lc}^2}{4c} \tag{6.32}$$

Using 1 mm VLBI observations, Kino et al. [2015] estimated the magnetic field at the base of the flow to be about 100 Gauss. Using this value for B_0, we get $\dot{M} \sim 10^{-7}$–$10^{-8}\ M_\odot\,\mathrm{yr}^{-1}$.

The mass accreted into the black hole of M87 is still undetermined. Using Chandra X-ray observations, the Bondi accretion rate of $\dot{M}_B = 0.12\ M_\odot\,\mathrm{yr}^{-1}$ was estimated by [Di Matteo et al., 2003]. However the measured X-ray luminosity, $L_X \sim 7 \times 10^{40}\,\mathrm{ergs}^{-1}$, suggests a lower accretion rate $\dot{M}_{acc} \ll \dot{M}_B$. Kuo et al. [2014] found an upper limit of $\dot{M}_{acc} < 1 \times 10^{-3}\ M_\odot\,\mathrm{yr}^{-1}$ using Faraday rotation measure. This limit would yield $\dot{M} \sim 10^{-4}$–$10^{-5}\dot{M}_{acc}$.

Thus, the mass-loss rate is much lower than the total mass accreted onto the black hole, implying that only a small fraction of the accreted matter is transported into the jet.

6.8 Summary

In this chapter, we have presented a detailed analysis of the two-dimensional kinematic evolution of the innermost jet in M87. This source allows us to investigate the question of the jet formation and propagation on scales of 10^3–$10^4 r_g$. WISE analysis was performed on 7 mm VLBA maps observed as part of the M87 VLBA movie project [Walker et al., 2008]. We summarize here the main findings of this analysis:

1. We have obtained the first complete velocity field of an AGN jet at sub-parsec scale, revealing a structured and highly stratified jet, with important transverse velocity.

2. The structure of the flow was also investigated using the SWD decomposition. The shape of the streamline is parabolic, well described by a power law $r \propto z^{0.58}$.

3. The viewing angle $\theta \simeq 18°$ was obtained using the speed of a moving component discovered in the counter jet, and the jet to counter jet intensity ratio. This viewing angle was also confirmed by the analysis of the jet rotation and from the modeling of the jet acceleration.

4. Stratification was analyzed using the SCC method, revealing a slow, mildly relativistic layer ($\beta \sim 0.5c$) associated either with an outer wind or with instability pattern speed, and a fast accelerating streamline ($\gamma \sim 2.5$ at $z_{\mathrm{obs}} \sim 3$ mas)

5. Acceleration and collimation of the flow was modeled following the theory of MHD jets, using two different methods. We found that the acceleration is at first linear $\gamma \propto r \propto z^{0.58}$, and then saturates, implying a magnetization at the base of the flow $\mu \sim 6$, and that equipartition between Poynting and kinetic energy is reached at a distance $z_{eq} \sim 3000\ R_s$, in excellent agreement with previous analytic and numerical simulation work.

6. The inner spine of the jet in M87 appears strongly deboosted and while we could not detect any features that we could unequivocally relate to this region, we estimated the Lorentz factor $\gamma_{\rm spine} \sim 6$ that would explain the intensity ratio between the sheath and the spine. We found a wind solution that connects this measure with the velocity observed at HST-1 in the optical regime, while the wind solution the we obtained for the sheath connects well with the velocity observed at HST-1 in the radio regime. This indicates that the kiloparsec structure observed in optical is of inner layers.

7. Indication of the jet rotation was found from the different velocity observed in the northern and southern limbs. This was used to obtain the angular velocity of the field line, $\Omega \sim 10^{-6} s^{-1}$. This suggests that this streamline is most likely launched in the inner region of the accretion disk, at a distance $r_0 \sim 5\ R_s$ from the central engine. However, a BZ scenario could not be excluded.

8. Finally, an estimate on the mass-loss $\dot{M} \sim 10^{-7}$–$10^{-8}\ M_\odot\,{\rm yr}^{-1}$ was obtained from the wind solution. This corresponds to $\dot{M} \sim 10^{-4}$–$10^{-5} \dot{M}_{acc}$.

Taken together, the WISE analysis of the jet in M87 draws a coherent picture of a magnetically launched, accelerated, and collimated jet. It is an important step for understanding the dominant physical mechanism of relativistic jets.

Continuation and expansion of the work started in this thesis will enable testing the results obtained for the jet in M87 and addressing other important aspects of the physics of relativistic flows. The methods that we used to model the acceleration and collimation zone in the M87 jets can be improved further to provide a more detailed physical description of the flow. One possibility would be to use more realistic flux function obtained from numerical simulation as input in the wind equation. Another possibility would be to attempt to reproduce our results by performing full 2D or 3D MHD simulations using the physical parameters that we estimated. This would allow us to investigate the inner part of the jet, providing further clues about the reason for the edge brightened morphology.

M87 jet is observed at 15 GHz as part of the MOJAVE project. We demonstrated in this thesis that the fast stream line is clearly detected at this frequency. Obtaining and analysis a closely sampled 15 GHz VLBA dataset on M87 would enable us to extend the analysis of the acceleration profile up to $z \sim 10^4\ R_s$. The ultra high resolution provided by the Global mm-VLBI Array (GMVA) could also be critical in confirming the results we obtained. The structure of the flow could be probed with GMVA at 86 GHz ($\lambda = 3\,\mathrm{mm}$) at distances from the central engine as close as as $\sim 10R_s$, giving as well the possibility to analyze the innermost part of the spine. Investigating the velocity would however requires better observing cadence than the current 4–6 month time intervals.

Chapter 7

Final conclusion and outlook

This thesis has provided a novel framework for addressing the problem of recovering two-dimensional structural and kinematic information from astronomical images and in answering several of the most debated questions regarding AGN physics, namely the formation and propagation up to large distance of their relativistic jets. Investigation of the structure and dynamics of the jets at parsec and sub-parsec scales is critical to determine the physical mechanisms governing the launching and propagation of extragalactic relativistic outflows. The analysis of multi epoch high resolution images obtained using the Very Large Baseline Interferometry (VLBI) technique at radio wavelengths is a unique way of studying structural evolution of jets in their innermost regions. This is however generally a very challenging task as relativistic jets are complex plasma outflows with complex internal structure affected by instabilities and shocks. Geometrical and relativistic effects resulting from extremely high bulk speed of the flow, the potential helical trajectories of some emitting regions, interaction of the flow with its surrounding environment all contribute to the complexity of the observed structure and dynamics of the flow. The sensitivity and sampling offered by VLBI observations is usually not optimal, making it difficult to relate observations made at different epochs. The algorithms and methods currently employed for this purpose are also limited especially for the analysis of transversely resolved jets. The structure of the jets is generally described using Gaussian model fitting technique which basically restrict the analysis to a one dimensional kinematic description, without any access to transverse distribution of the jet velocity.

The main aim of this thesis was to investigate the dynamics of relativistic jets by means of a new set of analysis tools able to recover the full wealth of structural information contained in VLBI images. Using these new methods, we wanted to answer three key questions: (1) what is the transverse kinematics and structure of parsec scale jets, and how it is related to jet instability, (2) what governs the acceleration and collimation of extragalactic relativistic outflows, (3) which mechanism is responsible for the launching of jets. To achieve these goals, we introduced a new wavelet based image segmentation and evaluation (WISE) method which provides robust decomposition and tracking of two-dimensional structural patterns in astronomical images. WISE was used to investigate the structure of parsec scale jets in three prominent radio sources, and to study in full detail the two-dimensional kinematic evolution of the innermost jet in M87, which is a unique probe of the jet acceleration and collimation region.

WISE comprises three main constituent parts. A key element of this method is the segmented wavelet decomposition (SWD) algorithm. It provides a structural representation of astronomical images, with exceptional sensitivity for identifying compact and marginally resolved features as well as to large scale structural patterns. The SWD decomposition delivers a set of two-dimensional structurally significant patterns (SSP), identified at each scale of the wavelet decomposition. Tracking of these SSP detected in multi-epochs images is performed with a multiscale cross correlation (MCC) algorithm. It combines structural information on different scales of the wavelet decomposition to provide a robust and reliable cross-identification of related SSP. Another critical aspect of the analysis of relativistic jets addressed by WISE is the ability to discriminate different partially overlapping emitting regions evolving at different speed. Investigation of this stratification is performed using a stacked cross correlation (SCC) analysis. SCC is a statistical approach providing robust identification of multiple velocity components which includes also an estimate on the significance and the uncertainty of each velocity components.

In order to assess the performance of WISE, several tests have been designed and performed, using both simulated images and images obtained from VLBI data. A set of simulated images of a compact jet was first used to characterize the fidelity and performance of the structural decomposition and velocity determination provided by WISE. This demonstrated the ability of WISE to recover complex structural evolution, to perform well on sparse or irregular sets of observations, and to be able to robustly identify different velocities in stratified flows. Subsequent applications of WISE on VLBI images of three prominent extragalactic jets observed as part of the MOJAVE project showed excellent agreement of the results obtained from WISE compared with the result provided by the MOJAVE team using the “standard” Gaussian model fitting technique.

The detailed analysis of the transverse kinematic and structure of MOJAVE sources, and in particular in the jets of 3C 273 and 3C 120, revealed the importance of the Kelvin-Helmoltz (K-H) instability to explain the morphologies of parsec scale jets. Going beyond global one dimensional kinematic analysis, WISE revealed transverse structure in the the jet of 3C 273 with three distinct flow lines clearly present inside the jet and evolving in a regular fashion, suggesting a pattern that may rise as a result of K-H instability. The positional precision of the WISE decomposition was also critical on modeling the helical trajectory of the components in the jet of 3C 120, revealing an helical surface mode of the K-H instability with an apparent wavelength $\lambda_{\mathrm{app}} = 15.8\,\mathrm{mas}$ and evolving at an apparent speed $\beta^{w}_{\mathrm{app}} = 2.0\,\mathrm{c}$.

To investigate the question of jet formation, we performed WISE analysis of the jet in M87. Its proximity combined with a large mass of the central black hole make it one of the primary source to probe the jet formation and acceleration region: for this source, 1 mas $\sim$ 0.08 pc $\sim$ 140 R_s. We used VLBA maps observed at 7 mm wavelength with a mean cadence of 21 days, suitable for the detection of the fastest components in the jet.

The structure of the flow was obtained from the SWD decomposition. The shape of the streamline is parabolic, well described by a power law $r \propto z^{0.58}$. Additionally, oscillations with an increasing spacial period are found to be superimposed on this smooth expansion.

Application of WISE on the jet in M87 has revealed for the first time a complete velocity field of an AGN jets at sub-parsec scale. It has unveiled a richly structured and highly stratified jet, with a wealth of dynamic evolution along and across the flow.

A component in the counter jet that could be followed over 5 consecutive epochs was used together with the intensity ratio between the jet and the counter jet to estimate the viewing angle, $\theta \simeq 18°$. This is the first reliable detection of a traceable kinematic changes in the counter jet in this source.

Stratification of the flow was studied by applying the SCC method to search for different velocity components in overlapping, optically thin regions of the flow. We detected a slow, mildly relativistic layer ($\beta \sim 0.5c$) associated either with an outer wind or with instability pattern speed, and a fast accelerating streamline ($\gamma \sim 2.5$ at $z_{\mathrm{obs}} \sim 3$ mas).

We further investigated the acceleration of the flow by studying the evolution of the velocity with distance from the core. In an initial phase, in the first 2 mas, the acceleration scales with the flow expansion, with $\gamma \propto r \propto z^{0.58}$. This strong connection between the acceleration and collimation is predicted by the theory of magnetized relativistic outflows. In this model the flow is collimated by a is much weaker, with magnetic field and is accelerated by conversion of magnetic, or Poynting, energy into kinetic energy. In a second phase, the acceleration rate strongly decrease, $\gamma \propto z^{0.16}$, which is expected to occur when the magnetic energy is coming closer to equipartition with the kinetic energy. The acceleration profile is also characterized by oscillations which are correlated with the oscillations found in the jet expansion.

Two different methods were employed to model the acceleration in combination with the collimation profile. The first method was based on analytical approximations describing the Poynting flux dominated flows, and the second one was based on the wind solution of the Bernoulli equation. Simple scaling relations can be obtained in the approximation of Poynting flux dominated jets. They described well our observations, in particular the initial acceleration regime. The observed oscillations are also predicted by this model. Another way to deal with the complexity of the magnetohydrodynamics (MHD) equations is to solve only the Bernoulli, or "wind", equation that governs the acceleration of the flow. We used this technique to describe the saturation of the jet acceleration. Our observations are best fitted by a magnetization at the inlet of the flow, with $\mu \sim 6$, reaching equipartition between Poynting and kinetic energy at a distance $z_{eq} \sim 3000\ R_s \sim 1.7$ pc, which is in excellent agreement with previous analytic and simulation works. After this point, the acceleration of the flow continues at a slower rate, and we found that our model connects remarkably well with the speed measured in the radio regime at the jet knot HST-1 ($\gamma \sim 4.5$), a peculiar feature of the jet located at a distance $z \sim 60pc \sim 10^5\ R_s$. This suggests that AGN jets are kinetic energy dominated at a distance of few parsec from the central engine. This conclusion is further supported by the fact that our analysis of the parsec-scale structures in three of the MOJAVE sources revealed ballistic motion and K-H instability.

The SCC analysis allows for an accurate measurement of the velocity in different regions of the flow. It revealed a systematic difference of the speed between the northern and southern limbs of the jet. This can be explained by the jet rotation which is expected in the context of magnetized outflow. Conservation of angular momentum is used to estimate the angular velocity of the field line, $\Omega \sim 10^{-6}s^{-1}$. This parameter is important to discriminate between the two main scenarios of magnetic jet launching, with either the accretion disk (Blandford & Payne, BP) or the magnetosphere of the central black hole (Blandford & Znajek, BZ) acting as the main source of the jet power. The angular velocity that we obtained suggests that the jet in M87 is launched in the inner part of the disk, at a distance $r_0 \sim 5\ R_s$ from the central engine, however a BZ scenario can not be entirely excluded.

The jet displays an edge brightened morphologies that can be explained by a fast deboosted inner spine. We estimated the Lorentz factor necessary to explain the intensity ratio between the spine and the sheath, $\gamma_{\text{spine}} \sim 6$ at a distance $z_{\text{obs}} \sim 3$ mas. Considering a streamline launched at the Innermost Stable Circular Orbit (ISCO) of the black hole, a solution of the wind equation for the spine can be found that would also connect with the velocity observed at HST-1 in the optical regime. This argues in favor of the spine-sheath scenario. However, more information on the intrinsic emissivity of these two components of the jet would be crucial to confirm this hypothesis.

Taken together, the WISE analysis of the jet in M87 draws a coherent picture of a magnetically launched, accelerated, and collimated jet. It is an important step for understanding the dominant physical mechanism of relativistic jets.

Continuation and expansion of the work started in this thesis will enable testing the results obtained for the jet in M87 and addressing other important aspects of the physics of relativistic flows. The methods that we used to model the acceleration and collimation zone in the M87 jets can be improved further to provide a more detailed physical description of the flow. One possibility would be to use more realistic flux function obtained from numerical simulation as input in the wind equation. Another possibility would be to attempt to reproduce our results by performing full 2D or 3D MHD simulations using the physical parameters that we estimated. This would allow us to investigate the inner part of the jet, providing further clues about the reason for the edge brightened morphology.

M87 jet is observed at 15 GHz as part of the MOJAVE project. We demonstrated in this thesis that the fast stream line is clearly detected at this frequency. Obtaining and analysis a closely sampled 15 GHz VLBA dataset on M87 would enable us to extend the analysis of the acceleration profile up to $z \sim 10^4\ R_s$. The ultra high resolution provided by the Global mm-VLBI Array (GMVA) could also be critical in confirming the results we obtained. The structure of the flow could be probed with GMVA at 86 GHz ($\lambda = 3\,\mathrm{mm}$) at distances from the central engine as close as as $\sim 10R_s$, giving as well the possibility to analyze the innermost part of the spine. Investigating the velocity would however requires better observing cadence than the current 4–6 month time intervals.

The Event Horizon Telescope (EHT) is another project that would provide an unparallel view of the accretion and outflow processes near the event horizon scale of the black hole in M87. At present time, EHT has been able to measure the extend of the ISCO, giving a hint on the spin of the black hole. With the inclusion of the Atacama Large Millimeter Array (ALMA), and the south pole telescope (SPT), it will be capable in the near future to directly observe this region.

We have demonstrated in this thesis the importance of WISE for the analysis of relativistic jets. Another unique and important aspects of WISE is that it is an automatic and extremely efficient method, which could be useful for the systematic analysis of large VLBI monitoring programs, like MOJAVE or the Boston University blazars project. This would broaden substantially the field of investigation to include a number of important aspects of jet physics, like instability, acceleration in the innermost part of the jets, or the connection of jet structural evolution with gamma-ray events.

List of Acronyms

ADAF Advection Dominated Accretion Flow

ALMA Atacama Large Millimeter Array

AGN Active Galactic Nuclei

AP Alfvén Point

APEX Atacama Pathfinder Experiment

BH Black Hole

CD Current Driven

DD Direct Detection

EHT Event Horizon Telescope

EVN European VLBI Network

FDR False Discovery Rate

FMP Fast Magnetosonic Point

FWHM Full Width at Half Maximum

GMVA Global mm-VLBI Array

GRB Gamma Ray Bursts

HST Hubble Space Telescope

ISCO Innermost Stable Circular Orbit

IWD Intermediate-scale Wavelet Decomposition

K-H Kelvin-Helmholtz

MCC Multiscale Cross Correlation

MHD Magnetohydrodynamics

MOJAVE Monitoring Of Jets in Active galactic nuclei with VLBA Experiments

NRAO National Radio Astronomy Observatory

PSF Point Spread Function

SCC Stacked Cross Correlation

SNR Signal to Noise Ratio

SSP Significant Structural Patterns

SWD Segmented Wavelet Decomposition

VLA Very Large Array

VLBA Very Large Baseline Array

VLBI Very Large Baseline Interferometry

WISE Wavelet-based Image Segmentation and Evaluation

WZNCC Weighted Zero-mean Normalized Cross Correlation

YSO Young Stellar Objects

Bibliography

A. Grossmann, J. M. (1984). Decomposition of hardy functions into square integrable wavelets of constant shape. *SIAM Journal on Mathematical Analysis*, 15:723–736.

Adams, N. J. and Williams, C. K. I. (2003). Dynamic trees for image modelling. *Image and Vision Computing*, 21(10):865–877.

Agarwal, S., Awan, A., and Roth, D. (2003). Learing to detect objecs in images via a spare, part-based representation. *IEEE Transactions on Pattern Analysis and Machine Intelligence*, 26:1475–1490.

Ahuja, N., Lertrattanapanich, S., and Bose, N. (2005). Properties determining choice of mother wavelet. *Vision, Image and Signal Processing, IEE Proceedings* -, 152(5):659–664.

Anderson, J. M., Li, Z.-Y., Krasnopolsky, R., and Blandford, R. D. (2003). Locating the launching region of t tauri winds: The case of dg tauri. *The Astrophysical Journal Letters*, 590:L107–L110.

Arulampalam, M. S., Maskell, S., and Gordon, N. andClapp, T. (2002). A tutorial on particle filters for online nonlinear/non-Gaussian Bayesian tracking. *IEEE Transactions on Signal Processing*, 50:174–188.

Asada, K. and Nakamura, M. (2012). The structure of the m87 jet: A transition from parabolic to conical streamlines. *The Astrophysical Journal Letters*, 745:L28.

Asada, K., Nakamura, M., Doi, A., Nagai, H., and Inoue, M. (2014). Discovery of sub- to superluminal motions in the m87 jet: An implication of acceleration from sub-relativistic to relativistic speeds. *The Astrophysical Journal Letters*, 781:L2.

Bach, U., Krichbaum, T. P., Middelberg, E., and Alef, W. andZensus, A. J. (2008). Resolving the jet in Cygnus A. In *The role of VLBI in the Golden Age for Radio Astronomy*.

Bardeen, J. M., Press, W. H., and Teukolsky, S. A. (1972). Rotating black holes: Locally nonrotating frames, energy extraction, and scalar synchrotron radiation. *The Astrophysical Journal*, 178:347.

Beckmann, V. and Shrader, C. R. (2012). *Active Galactic Nuclei*.

Begelman, M. C. and Li, Z.-Y. (1994). Asymptotic domination of cold relativistic mhd winds by kinetic energy flux. *The Astrophysical Journal*, 426:269–278.

Belongie, S., Malik, J., and Puzicha, J. (2002). Shape matching and object recognition using shape contexts. *IEEE Transactions on Pattern Analysis and Machine Intelligence*, 24(4):509–522.

Bertero, M., Boccacci, P., and Piana, M. (1997). Resolution and super-resolution in inverse diffraction. In Chavent, G. and Sabatier, P. C., editors, *Lecture Notes in Physics, Berlin Springer Verlag*, volume 486 of *Lecture Notes in Physics, Berlin Springer Verlag*, page 1.

Beucher, S. and Meyer, F. (1993). The morphological approach to segmentation: the watershed transformation. mathematical morphology in image processing. *Optical Engineering*, 34:433–481.

Biretta, J. A., Sparks, W. B., and Macchetto, F. (1999). Hubble space telescope observations of superluminal motion in the m87 jet. *The Astrophysical Journal*, 520:621–626.

Biretta, J. A., Zhou, F., and Owen, F. N. (1995). Detection of Proper Motions in the M87 Jet. ApJ, 447:582.

Biretta, J. A., Zhou, F., and Owen, F. N. (1995). Detection of proper motions in the m87 jet. *The Astrophysical Journal*, 447:582.

Blandford, R. D. and Konigl, A. (1979). Relativistic jets as compact radio sources. *The Astrophysical Journal*, 232:34.

Blandford, R. D. and Payne, D. G. (1982). Hydromagnetic flows from accretion discs and the production of radio jets. *Monthly Notices of the Royal Astronomical Society*, 199:883–903.

Blandford, R. D. and Rees, M. J. (1978). Extended and compact extragalactic radio sources - interpretation and theory. *Physica Scripta*, 17:265–274.

Blandford, R. D. and Znajek, R. L. (1977). Electromagnetic extraction of energy from kerr black holes. *Monthly Notices of the Royal Astronomical Society*, 179:433–456.

Camenzind, M. (1986). Centrifugally driven mhd-winds in active galactic nuclei. *Astronomy and Astrophysics*, 156:137–151.

Cheung, C. C., Harris, D. E., and Stawarz, L. (2007). Superluminal radio features in the m87 jet and the site of flaring tev gamma-ray emission. *The Astrophysical Journal*, 663(2):L65–L68.

Choi, M., Kang, M., and Tatematsu, K. (2011). Rotation of the ngc 1333 iras 4a2 protostellar jet. *The Astrophysical Journal Letters*, 728:L34.

Clark, B. G. (1980). An efficient implementation of the algorithm 'CLEAN'. A&A, 89:377.

Cornwell, T. J. (2008). Multiscale CLEAN Deconvolution of Radio Synthesis Images. *IEEE Journal of Selected Topics in Signal Processing*, 2:793–801.

Daly, R. A. and Marscher, A. P. (1988). The gasdynamics of compact relativistic jets. *The Astrophysical Journal*, 334:539–551.

Di Matteo, T., Allen, S. W., Fabian, A. C., Wilson, A. S., and Young, A. J. (2003). Accretion onto the supermassive black hole in m87. *The Astrophysical Journal*, 582(1):133–140.

Djamdji, J.-P., Bijaoui, A., and Maniere, R. (1993). Geometrical registration of remotely sensed images with the use of the wavelet transform. volume 1938, pages 412–422.

Doeleman, S. S., Fish, V. L., Schenck, D. E., Beaudoin, C., Blundell, R., Bower, G. C., Broderick, A. E., Chamberlin, R., Freund, R., Friberg, P., Gurwell, M. A., Ho, P. T. P., Honma, M., Inoue, M., Krichbaum, T. P., Lamb, J., Loeb, A., Lonsdale, C., Marrone, D. P., Moran, J. M., Oyama, T., Plambeck, R., Primiani, R. A., Rogers, A. E. E., Smythe, D. L., SooHoo, J., Strittmatter, P., Tilanus, R. P. J., Titus, M., Weintroub, J., Wright, M., Young, K. H., and Ziurys, L. M. (2012). Jet-launching structure resolved near the supermassive black hole in m87. *Science*, 338:355.

Doucet, A. and Gordon, N. J. (1999). Simulation-based optimal filter for maneuvering target tracking. In Drummond, O. E., editor, *Signal and Data Processing of Small Targets 1999*, volume 3809 of *Society of Photo-Optical Instrumentation Engineers (SPIE) Conference Series*, pages 241–255.

Doucet, A. and Wang, X. (2005). Monte Carlo methods for signal processing: a review in the statistical signal processing context. *IEEE Signal Processing Magazine*, 22:152–170.

Fanaroff, B. L. and Riley, J. M. (1974). The morphology of extragalactic radio sources of high and low luminosity. *Monthly Notices of the Royal Astronomical Society*, 167:31P–36P.

Fendt, C. (2011). Jet rotation driven by magnetohydrodynamic shocks in helical magnetic fields. *The Astrophysical Journal*, 737:43.

Fendt, C. and Ouyed, R. (2004). Ultrarelativistic magnetohydrodynamic jets in the context of gamma-ray bursts. *The Astrophysical Journal*, 608:378–390.

Fomalont, E. B. (1999). Image Analysis. In Taylor, G. B., Carilli, C. L., and Perley, R. A., editors, *Synthesis Imaging in Radio Astronomy II*, volume 180 of *Astronomical Society of the Pacific Conference Series*, page 301.

Fomalont, E. B. (1999). Image analysis. volume 180, page 301.

Fromm, C. M., Ros, E., Perucho, M., Savolainen, T., Mimica, P., Kadler, M., Lobanov, A. P., and Zensus, J. A. (2013). Catching the radio flare in cta 102. iii. core-shift and spectral analysis. *Astronomy and Astrophysics*, 557:A105.

Gebhardt, K., Adams, J., Richstone, D., Lauer, T. R., Faber, S. M., Gültekin, K., Murphy, J., and Tremaine, S. (2011). The black hole mass in m87 from gemini/nifs adaptive optics observations. *The Astrophysical Journal*, 729:119.

Giachetti, A. (2000). Matching techniques to compute image motion. *Image and Vision Computing*, 18(3):247–260.

Giroletti, M., Hada, K., Giovannini, G., Casadio, C., Beilicke, M., Cesarini, A., Cheung, C. C., Doi, A., Krawczynski, H., Kino, M., Lee, N. P., and Nagai, H. (2012). The kinematic of hst-1 in the jet of m 87. *Astronomy and Astrophysics*, 538:L10.

Hada, K., Doi, A., Kino, M., Nagai, H., Hagiwara, Y., and Kawaguchi, N. (2011). An origin of the radio jet in m87 at the location of the central black hole. *Nature*, 477(7363):185–187.

Hada, K., Kino, M., Doi, A., Nagai, H., Honma, M., Hagiwara, Y., Giroletti, M., Giovannini, G., and Kawaguchi, N. (2013). The innermost collimation structure of the m87 jet down to extasciitilde10 schwarzschild radii. *The Astrophysical Journal*, 775:70.

Hardee, P. E. and Eilek, J. A. (2011). Using twisted filaments to model the inner jet in m 87. *The Astrophysical Journal*, 735(1):61.

Hardee, P. E., Walker, R. C., and Gómez, J. L. (2005). Modeling the 3C 120 Radio Jet from 1 to 30 Milliarcseconds. ApJ, 620:646–664.

Hardee, P. E., Walker, R. C., and Gómez, J. L. (2005). Modeling the 3c 120 radio jet from 1 to 30 milliarcseconds. *The Astrophysical Journal*, 620(2):646.

Harms, R. J., Ford, H. C., Tsvetanov, Z. I., Hartig, G. F., Dressel, L. L., Kriss, G. A., Bohlin, R., Davidsen, A. F., Margon, B., and Kochhar, A. K. (1994). Hst fos spectroscopy of m87: Evidence for a disk of ionized gas around a massive black hole. *The Astrophysical Journal Letters*, 435:L35–L38.

Hirabayashi, H., Hirosawa, H., Kobayashi, H., Murata, Y., Edwards, P. G., Fomalont, E. B., Fujisawa, K., Ichikawa, T., Kii, T., Lovell, J. E. J., Moellenbrock, G. A., Okayasu, R., Inoue, M., Kawaguchi, N., Kameno, S., Shibata, K. M., Asaki, Y., Bushimata, T., Enome, S., Horiuchi, S., Miyaji, T., Umemoto, T., Migenes, V., Wajima, K., Nakajima, J., Morimoto, M., Ellis, J., Meier, D. L., Murphy, D. W., Preston, R. A., Smith, J. G., Tingay, S. J., Traub, D. L., Wietfeldt, R. D., Benson, J. M., Claussen, M. J., Flatters, C., Romney, J. D., Ulvestad, J. S., D'Addario, L. R., Langston, G. I., Minter, A. H., Carlson, B. R., Dewdney, P. E., Jauncey, D. L., Reynolds, J. E., Taylor, A. R., McCulloch, P. M., Cannon, W. H., Gurvits, L. I., Mioduszewski, A. J., Schilizzi, R. T., and Booth, R. S. (1998). Overview and initial results of the very long baseline interferometry space observatory programme. *Science*, 281:1825.

Högbom, J. A. (1974). Aperture Synthesis with a Non-Regular Distribution of Interferometer Baselines. A&AS, 15:417.

Holschneider, M., Kronland-Martinet, R., Morlet, J., and Tchamitchian, P. (1989). A real-time algorithm for signal analysis with the help of the wavelet transform. In Combes, J.-M., Grossmann, A., and Tchamitchian, P., editors, *Wavelets. Time-Frequency Methods and Phase Space*, page 286.

Hovatta, T., Aller, M. F., Aller, H. D., Clausen-Brown, E. andHoman, D. C., Kovalev, Y. Y., Lister, M. L. andPushkarev, A. B., and Savolainen, T. (2014). MOJAVE: Monitoring of Jets in Active Galactic Nuclei with VLBA Experiments. XI. Spectral Distributions. AJ, 147:143.

Hummel, C. A., Muxlow, T. W. B., Krichbaum, T. P. andQuirrenbach, A., Schalinski, C. J., and Witzel, A. andJohnston, K. J. (1992). MERLIN and VLBI observations of the quasar 0836 + 710: Morphology of a parsec-kiloparsec scale jet. A&A, 266:93–100.

Högbom, J. A. (1974). Aperture synthesis with a non-regular distribution of interferometer baselines. *Astronomy and Astrophysics Supplement Series*, 15:417.

Jordán, A., Côté, P., Blakeslee, J. P., Ferrarese, L., McLaughlin, D. E., Mei, S., Peng, E. W., Tonry, J. L., Merritt, D., Milosavljevic, M., Sarazin, C. L., Sivakoff, G. R., and West, M. J. (2005). The acs virgo cluster survey. x. half-light radii of globular clusters in early-type galaxies: Environmental dependencies and a standard ruler for distance estimation. *The Astrophysical Journal*, 634:1002–1019.

Kadler, M., Ros, E., Perucho, M., Kovalev, Y. Y., Homan, D. C., Agudo, I., Kellermann, K. I., Aller, M. F., Aller, H. D., Lister, M. L., and Zensus, J. A. (2008). The trails of superluminal jet components in 3c 111. *The Astrophysical Journal*, 680:867–884.

Kardashev, N. S., Khartov, V. V., Abramov, V. V., Avdeev, V. Y., Alakoz, A. V., Aleksandrov, Y. A., Ananthakrishnan, S., Andreyanov, V. V., Andrianov, A. S., Antonov, N. M., Artyukhov, M. I., Arkhipov, M. Y., Baan, W., Babakin, N. G., Babyshkin, V. E., Bartel', N., Belousov, K. G., Belyaev, A. A., Berulis, J. J., Burke, B. F., Biryukov, A. V., Bubnov, A. E., Burgin, M. S., Busca, G., Bykadorov, A. A., Bychkova, V. S., Vasil'kov, V. I., Wellington, K. J., Vinogradov, I. S., Wietfeldt, R., Voitsik, P. A., Gvamichava, A. S., Girin, I. A., Gurvits, L. I., Dagkesamanskii, R. D., D'Addario, L., Giovannini, G., Jauncey, D. L., Dewdney, P. E., D'yakov, A. A., Zharov, V. E., Zhuravlev, V. I., Zaslavskii, G. S., Zakhvatkin, M. V., Zinov'ev, A. N., Ilinen, Y., Ipatov, A. V., Kanevskii, B. Z., Knorin, I. A., Casse, J. L., Kellermann, K. I., Kovalev, Y. A., Kovalev, Y. Y., Kovalenko, A. V., Kogan, B. L., Komaev, R. V., Konovalenko, A. A., Kopelyanskii, G. D., Korneev, Y. A., Kostenko, V. I., Kotik, A. N., Kreisman, B. B., Kukushkin, A. Y., Kulishenko, V. F., Cooper, D. N., Kut'kin, A. M., Cannon, W. H., Larionov, M. G., Lisakov, M. M., Litvinenko, L. N., Likhachev, S. F., Likhacheva, L. N., Lobanov, A. P., Logvinenko, S. V., Langston, G., McCracken, K., Medvedev, S. Y., Melekhin, M. V., Menderov, A. V., Murphy, D. W., Mizyakina, T. A., Mozgovoi, Y. V., Nikolaev, N. Y., Novikov, B. S., Novikov, I. D., Oreshko, V. V., Pavlenko, Y. K., Pashchenko, I. N., Ponomarev, Y. N., Popov, M. V., Pravin-Kumar, A., Preston, R. A., Pyshnov, V. N., Rakhimov, I. A., Rozhkov, V. M., Romney, J. D., Rocha, P., Rudakov, V. A., Räisänen, A., Sazankov, S. V., Sakharov, B. A., Semenov, S. K., Serebrennikov, V. A., Schilizzi, R. T., Skulachev, D. P., Slysh, V. I., Smirnov, A. I., Smith, J. G., Soglasnov, V. A., Sokolovskii, K. V., Sondaar, L. H., Stepan'yants, V. A., Turygin, M. S., Turygin, S. Y., Tuchin, A. G., Urpo, S., Fedorchuk, S. D., Finkel'shtein, A. M., Fomalont, E. B., Fejes, I., Fomina, A. N., Khapin, Y. B., Tsarevskii, G. S., Zensus, J. A., Chuprikov, A. A., Shatskaya, M. V., Shapirovskaya, N. Y., Sheikhet, A. I., Shirshakov, A. E., Schmidt, A., Shnyreva, L. A., Shpilevskii, V. V., Ekers, R. D., and Yakimov, V. E. (2013). Radioastron"-a telescope with a size of 300 000 km: Main parameters and first observational results. *Astronomy Reports*, 57:153–194.

Kino, M., Takahara, F., Hada, K., Akiyama, K., Nagai, H., and Sohn, B. W. (2015). Magnetization degree at the jet base of m87 derived from the event horizon telescope data: Testing the magnetically driven jet paradigm. *The Astrophysical Journal*, 803:30.

Kirk, J. G. and Duffy, P. (1999). Topical review: Particle acceleration and relativistic shocks. *Journal of Physics G Nuclear Physics*, 25:163.

Komissarov, S. S., Barkov, M. V., Vlahakis, N., and Konigl, A. (2007). Magnetic acceleration of relativistic agn jets. *Monthly Notices of the Royal Astronomical Society*, 380(1):51–70.

Konigl, A. (1981). Relativistic jets as x-ray and gamma-ray sources. *The Astrophysical Journal*, 243:700–709.

Kovalev, Y. Y., Lister, M. L., Homan, D. C., and Kellermann, K. I. (2007). The inner jet of the radio galaxy m87. *The Astrophysical Journal*, 668(1):L27–L30.

Kovalev, Y. Y., Lobanov, A. P., and Pushkarev, A. B. andZensus, J. A. (2008). Opacity in compact extragalactic radio sources and its effect on astrophysical and astrometric studies. A&A, 483:759–768.

Krichbaum, T. P., Roy, A., Wagner, J., Rottmann, H., Hodgson, J. A., Bertarini, A., Alef, W., Zensus, J. A., Marscher, A. P., Jorstad, S. G., Freund, R., Marrone, D., Strittmatter, P., Ziurys, L., Blundell, R., Weintroub, J., Young, K., Fish, V., Doeleman, S., Bremer, M., Sanchez, S., Fuhrmann, L., Angelakis, E., and Karamanavis, V. (2013). Zooming towards the event horizon - mm-vlbi today and tomorrow. *ArXiv e-prints*, 1305:2811.

Kuo, C. Y., Asada, K., Rao, R., Nakamura, M., Algaba, J. C., Liu, H. B., Inoue, M., Koch, P. M., Ho, P. T. P., Matsushita, S., Pu, H.-Y., Akiyama, K., Nishioka, H., and Pradel, N. (2014). Measuring mass accretion rate onto the supermassive black hole in m87 using faraday rotation measure with the submillimeter array. *The Astrophysical Journal*, 783(2):L33.

Lal, D. V., Lobanov, A. P., and Jiménez-Monferrer, S. (2010). Array configuration studies for the square kilometre array - implementation of figures of merit based on spatial dynamic range. *arXiv:1001.1477 [astro-ph]*.

Lewis, J. (1995). Fast normalized cross-correlation. *Vision Interface*, 10(1):120–123.

Li, Z.-Y., Chiueh, T., and Begelman, M. C. (1992). Electromagnetically driven relativistic jets - a class of self-similar solutions. *The Astrophysical Journal*, 394:459–471.

Lister, M. L., Aller, M. F., Aller, H. D., Homan, D. C., Kellermann, K. I., Kovalev, Y. Y., Pushkarev, A. B., Richards, J. L., Ros, E., and Savolainen, T. (2013). Mojave. x. parsec-scale jet orientation variations and superluminal motion in active galactic nuclei. *The Astronomical Journal*, 146:120.

Lobanov, A., Hardee, P., and Eilek, J. (2003). Internal structure and dynamics of the kiloparsec-scale jet in m87. *New Astronomy Reviews*, 47(6-7):629–632.

Lobanov, A. P. (1998a). Spectral distributions in compact radio sources. I. Imaging with VLBI data. A&AS, 132:261–273.

Lobanov, A. P. (1998b). Ultracompact jets in active galactic nuclei. A&A, 330:79–89.

Lobanov, A. P. (2012). The SKA and "High-Resolution" Science. In Barbosa, D., Anton, S., Gurvits, L., and Maia, D., editors, *Square Kilometre Array: Paving the Way for the New 21st Century Radio Astronomy Paradigm*, page 75. Springer-Verlag: Belrin Heidelrberg.

Lobanov, A. P., Krichbaum, T. P., Witzel, A., Kraus, A., Zensus, J. A., Britzen, S., Otterbein, K., Hummel, C. A., and Johnston, K. (1998). Vsop imaging of s5 0836+710: a close-up on plasma instabilities in the jet. *Astronomy and Astrophysics*, 340:L60–L64.

Lobanov, A. P. and Zensus, J. A. (1999). Spectral Evolution of the Parsec-Scale Jet in the Quasar 3C 345. ApJ, 521:509–525.

Lobanov, A. P. and Zensus, J. A. (2001). A Cosmic Double Helix in the Archetypical Quasar 3C273. *Science*, 294:128–131.

Ly, C., Walker, R. C., and Junor, W. (2007). High frequency vlbi imaging of the jet base of m87. *The Astrophysical Journal*, 660(1):200–205.

Lyubarsky, Y. (2009). Asymptotic structure of poynting dominated jets. *The Astrophysical Journal*, 698(2):1570–1589.

Lyubarsky, Y. E. (2010). Transformation of the poynting flux into kinetic energy in relativistic jets. *Monthly Notices of the Royal Astronomical Society*, 402:353–361.

Mallat, S. G. (1989). A theory for multiresolution signal decomposition - the wavelet representation. *IEEE Transactions on Pattern Analysis and Machine Intelligence*, 11:674–693.

Marshall, H. L., Miller, B. P., Davis, D. S., Perlman, E. S., Wise, M., Canizares, C. R., and Harris, D. E. (2002). A high-resolution x-ray image of the jet in m87. *The Astrophysical Journal*, 564:683–687.

Meier, D. L., Koide, S., and Uchida, Y. (2001). Magnetohydrodynamic production of relativistic jets. *Science*, 291:84–92.

Men'shchikov, A., André, P., Didelon, P., Motte, F., Hennemann, M., and Schneider, N. (2012). A multi-scale, multi-wavelength source extraction method: getsources. *Astronomy and Astrophysics*, 542:A81.

Mertens, F. and Lobanov, A. (2015). Wavelet-based decomposition and analysis of structural patterns in astronomical images. *Astronomy & Astrophysics*, 574:A67.

Meyer, E. T., Sparks, W. B., Biretta, J. A., Anderson, J., Sohn, S. T., van der Marel, R. P., Norman, C., and Nakamura, M. (2013). Optical proper motion measurements of the m87 jet: New results from the hubble space telescope. *The Astrophysical Journal Letters*, 774:L21.

Michel, F. C. (1969). Relativistic stellar-wind torques. *The Astrophysical Journal*, 158:727.

Mizuno, Y., Lyubarsky, Y., Nishikawa, K.-I., and Hardee, P. E. (2012). Three-dimensional relativistic magnetohydrodynamic simulations of current-driven instability. iii. rotating relativistic jets. *The Astrophysical Journal*, 757(1):16.

Myint, S. W., Yuan, M., Cerveny, R. S., and Giri, C. P. (2008). Comparison of remote sensing image processing techniques to identify tornado damage areas from landsat tm data. *Sensors*, 8(2):1128–1156.

Nakamura, M. and Asada, K. (2013). The parabolic jet structure in m87 as a magnetohydrodynamic nozzle. *The Astrophysical Journal*, 775:118.

Narayan, R., Mahadevan, R., and Quataert, E. (1998). Advection-dominated accretion around black holes. pages 148–182, eprint: arXiv:astro-ph/9803141.

Norman, M. L., Winkler, K.-H. A., Smarr, L., and Smith, M. D. (1982). Structure and dynamics of supersonic jets. *Astronomy and Astrophysics*, 113:285–302.

Owen, F. N., Hardee, P. E., and Cornwell, T. J. (1989). High-resolution, high dynamic range vla images of the m87 jet at 2 centimeters. *The Astrophysical Journal*, 340:698–707.

Pan, B., Xie, H., and Wang, Z. (2010). Equivalence of digital image correlation criteria for pattern matching. *Applied Optics*, 49(28):5501.

Paulson, C., Ezekiel, S., and Wu, D. (2010). Wavelet-based image registration. volume 7704, pages 77040M–77040M–12.

Pearson, T. J. (1999). Non-Imaging Data Analysis. In Taylor, G. B., Carilli, C. L., and Perley, R. A., editors, *Synthesis Imaging in Radio Astronomy II*, volume 180 of *Astronomical Society of the Pacific Conference Series*, page 335.

Perlman, E. S., Biretta, J. A., Zhou, F., Sparks, W. B., and Macchetto, F. D. (1999a). Optical and radio polarimetry of the m87 jet at 0.2” resolution. *The Astronomical Journal*, 117:2185–2198.

Perlman, E. S., Biretta, J. A., Zhou, F., Sparks, W. B., and Macchetto, F. D. (1999b). Optical and radio polarimetry of the m87 jet at 0.2” resolution. *The Astronomical Journal*, 117:2185–2198.

Porcas, R. W. (2009). Radio astrometry with chromatic agn core positions. *Astronomy and Astrophysics*, 505:L1–L4.

Pushkarev, A. B., Hovatta, T., Kovalev, Y. Y., Lister, M. L., Lobanov, A. P., Savolainen, T., and Zensus, J. A. (2012). Mojave: Monitoring of jets in active galactic nuclei with vlba experiments. ix. nuclear opacity. *Astronomy and Astrophysics*, 545:113.

Rees, M. J. (1966). Appearance of relativistically expanding radio sources. *Nature*, 211:468–470.

Rué, F. and Bijaoui, A. (1997). A multiscale vision model to analyse field astronomical images. *Experimental Astronomy*, 7:129–160.

Schinzel, F. K., Lobanov, A. P., Taylor, G. B., Jorstad, S. G., Marscher, A. P., and Zensus, J. A. (2012). Relativistic outflow drives gamma-ray emission in 3c 345. *Astronomy and Astrophysics*, 537:A70.

Seymour, M. D. and Widrow, L. M. (2002). Multiresolution analysis of substructure in dark matter halos. *The Astrophysical Journal*, 578(2):689–701.

Shakura, N. I. and Sunyaev, R. A. (1973). Black holes in binary systems. observational appearance. *Astronomy and Astrophysics*, 24:337–355.

Shensa, M. J. (1992). The discrete wavelet transform: wedding the a trous and mallat algorithms. *IEEE Transactions on Signal Processing*, 40:2464–2482.

Sidenbladh, H., Svenson, P., and Schubert, J. (2004). Comparing multi-target trackers on different force unit levels. In Kadar, I., editor, *Signal Processing, Sensor Fusion, and Target Recognition XIII*, volume 5429 of *Society of Photo-Optical Instrumentation Engineers (SPIE) Conference Series*, pages 306–314.

Sikora, M., Begelman, M. C., Madejski, G. M., and Lasota, J.-P. (2005). Are quasar jets dominated by poynting flux? *The Astrophysical Journal*, 625:72–77.

Sol, H., Pelletier, G., and Asseo, E. (1989). Two-flow model for extragalactic radio jets. *Monthly Notices of the Royal Astronomical Society*, 237:411–429.

Spruit, H. C. (2010). Theory of magnetically powered jets. In Belloni, T., editor, *The Jet Paradigm*, number 794 in Lecture Notes in Physics, pages 233–263. Springer Berlin Heidelberg.

Staff, J. E., Koning, N., Ouyed, R., Thompson, A., and Pudritz, R. E. (2015). Hubble space telescope scale 3d simulations of mhd disc winds: a rotating two-component jet structure. *Monthly Notices of the Royal Astronomical Society*, 446:3975–3991.

Starck, J.-L. and Murtagh, F. (1994). Image restoration with noise suppression using the wavelet transform. *Astronomy and Astrophysics*, 288:342–348.

Starck, J.-L. and Murtagh, F. (2006). *Astronomical image and data analysis*. Springer.

Tchekhovskoy, A. (2015). Launching of active galactic nuclei jets. In Contopoulos, I., Gabuzda, D., and Kylafis, N., editors, *The Formation and Disruption of Black Hole Jets*, number 414 in Astrophysics and Space Science Library, pages 45–82. Springer International Publishing.

Tchekhovskoy, A., McKinney, J. C., and Narayan, R. (2008). Simulations of ultra-relativistic magnetodynamic jets from gamma-ray burst engines. *Monthly Notices of the Royal Astronomical Society*, 388(2):551–572.

Toma, K. and Takahara, F. (2013). Efficient acceleration of relativistic magnetohydrodynamic jets. *Progress of Theoretical and Experimental Physics*, 2013:083E02.

Tout, C. A. and Pringle, J. E. (1996). Can a disc dynamo generate large-scale magnetic fields? *Monthly Notices of the Royal Astronomical Society*, 281:219–225.

Tsinganos, K. and Bogovalov, S. (2002). Magnetic collimation of relativistic outflows in jets with a high mass flux. *Monthly Notices of the Royal Astronomical Society*, 337:553–558.

Unser, M. (1999). Splines: a perfect fit for signal and image processing. *IEEE Signal Processing Magazine*, 16:22–38.

Unwin, S. C., Wehrle, A. E., Lobanov, A. P. andZensus, J. A., Madejski, G. M., and Aller, M. F. andAller, H. D. (1997). Variability in the Inverse-Compton X-Ray Flux from the Jet in Quasar 3C 345. ApJ, 480:596–606.

Urry, C. M. and Padovani, P. (1995). Unified schemes for radio-loud active galactic nuclei. *Publications of the Astronomical Society of the Pacific*, 107:803.

Vanderbrug, G. and Rosenfeld, A. (1977). Two-stage template matching. *IEEE Transactions on Computers*, C-26(4):384–393.

Vlahakis, N. (2015). Theory of relativistic jets. In Contopoulos, I., Gabuzda, D., and Kylafis, N., editors, *The Formation and Disruption of Black Hole Jets*, number 414 in Astrophysics and Space Science Library, pages 177–205. Springer International Publishing.

Vlahakis, N. and Königl, A. (2004). Magnetic driving of relativistic outflows in active galactic nuclei. i. interpretation of parsec-scale accelerations. *The Astrophysical Journal*, 605:656–661.

Walker, R. C., Ly, C., Junor, W., and Hardee, P. J. (2008). A vlba movie of the jet launch region in m87. *Journal of Physics: Conference Series*, 131(1):012053.

Witkin, A., Terzopoulos, D., and Kass, M. (1987). Signal matching through scale space. *International Journal of Computer Vision*, 1(2):133–144.

Yuan, D., Elvidge, C. D., and Lunetta, R. (1998). Survey of multispectral methods for land cover changeanalysis". In Eden, M. and Parry, J., editors, *Remote Sensing Change Detection, Environmental Monitoring Methods andApplications*, page 1. Ann Arbor Press.

Zensus, J. A., Cohen, M. H., and Unwin, S. C. (1995). The Parsec-scale jet in quasar 3C 345. ApJ, 443:35–53.

Zheng, Q. and Chellappa, R. (1993). A computational vision approach to image registration. *IEEE Transactions on Image Processing*, 2(3):311–326.

Zitová, B. and Flusser, J. (2003). Image registration methods: a survey. *Image and Vision Computing*, 21:977–1000.

List of Figures

1.1 VLA image of the 100 kpc long jets in Cygnus A. 2
1.2 Schematic representation of the current AGN unification model. . . . 4

2.1 Artist view of a black hole surrounded by an accretion disk of hot gas and torus of cooler gas and dust. 8
2.2 Illustration of the magnetic field lines configuration near the black hole. 10
2.3 Typical example of evolution of the velocity and magnetic field, with distance from the central engine, of a magnetic flow. 11
2.4 Example of Kelvin-Helmholtz and Current Driven instabilities that are known to develop in AGN jets. 13
2.5 Example of relativistic effect with implication on the apparent velocity and observed radiation. 14

3.1 Relation between scales of a wavelet transform and spatial scales represented by the FWHM of a Gaussian profile. 19
3.2 Schematic illustration of the method used for SSP localization, applied to a one-dimensional case. 22
3.3 Example of the SWD decomposition performed on a radio map of the jet in M87 observed using the VLA telescope. 24
3.4 Illustration of the feature-matching method using a coarse-to-fine strategy. 26
3.5 Schematic illustration of the detection method used for displacement measurements in a one-dimensional case. 29
3.6 Relation between scales of a wavelet transform and spatial scales represented by the FWHM of a Gaussian profile for the triangle and a triangle2 scaling function. 31

4.1 SWD decomposition of a map of a simulated jet at scales of 1.6, 0.8, and 0.4 beam size. 36
4.2 Fractional detection rates of the SWD method in comparison with the direct detection for different feature SNR and FWHM 38
4.3 Characterization of the separability of two close features with varying FWHM ratio. 39

4.4 WISE decomposition and analysis of a simulated jet with an accelerating sinusoidal velocity field and an additional r.m.s of 0.28 FWHM of the beam 41
4.5 WISE decomposition and analysis of a simulated jet with an accelerating sinusoidal velocity field and an additional r.m.s of 0.43 FWHM of the beam 42
4.6 WISE decomposition and analysis of a simulated jet with two speed components. 43
4.7 Stacked cross correlation analysis of simulated stratified jet. 44
4.8 Stacked cross correlation analysis of simulated jet with random velocity field. 45

5.1 Core separation plot of the most prominent features in the jet of 3C 273 comparing the WISE analysis with the model-fit based MOJAVE results. 49
5.2 Two-dimensional tracks of the SSP detected by WISE at scales 3–4 of the SWD in the jet of 3C 273. 50
5.3 Detailed analysis of the jet of 3C 273 at the scale 2 of SWD for the epochs between 11/2003 and 12/2006. 51
5.4 Core-separation plot of the features identified in the jet of 3C 120 comparing the WISE analysis with the model-fit based MOJAVE results. 52
5.5 Two-dimensional tracks of SSP detected in 3C 120 overplotted on a stacked-epoch image of the jet rotated by -1.17 radian. In three insets, we plot the time and PA of each components crossing a distance from the core of 2 mas, 7 mas and 12 mas respectively. 53
5.6 Time of the first PA maximum of the sinusoid function describing the change of PA with time at a certain distance from the core. 55
5.7 Evolution of the instability in the jet of 3C120 with time. 55
5.8 Core-separation plot of the features identified in the jet of 3C 111. . . 56
5.9 Two-dimensional tracks of SSP detected in 3C 111 at scale 2 of SWD. 57
5.10 Two-dimensional tracks of SSP detected in 3C 111 at scale 2 of SWD for a selection of components. 57

6.1 Radio and Optical image of the jet in M87 observed using the VLA and HST telescopes showing the kiloparsec structure. 62
6.2 Observed displacements of the significant structural patterns detected in the jet of M 87. 65
6.3 Longitudinal and transverse velocities of SSP measured in the jet of M87. 66
6.4 Stacked cross correlation analysis of the northern and southern limbs of the jet at distances between 0.5 and 1 mas from the core. 68
6.5 Stacked cross correlation analysis of the northern and southern limbs of the jet at distances between 1 and 3 mas from the core. 70

6.6 Jet radius and apparent opening angle of the jet in M87 with distance from the core. 72
6.7 Two-dimensional displacements of structural patterns detected using WISE analysis of 2 cm VLBA observations between 2000/04/07 and 2000/06/27. 73
6.8 Jet and counter jet intensity measured on a longitudinal slice of the jet and corresponding ratio. 75
6.9 Core separations of the SSP that we tracked for at least 4 epochs over a 0.8 mas extent in both the jet and counter-jet direction. 76
6.10 The jet viewing angle constraints obtained from the minimum and maximum jet to counter jet intensity ratio R and apparent velocity β_{app} measured at core separations between 0.4 and 0.8 mas. 76
6.11 Schematic illustration of the effect of the jet rotation on the viewing angle in the three regions of the jet. 77
6.12 Parameters of the jet rotation obtained for the regions between 0.5 and 1 mas and between 1 and 3 mas at different effective viewing angle θ. 79
6.13 Acceleration profile of the jet in M87 from WISE analysis and historical measurements. 83
6.14 Apparent velocity of the investigated field line. 84
6.15 Best fit of the observed acceleration and collimation of the jet in M87. 86
6.16 Wind solution for different models of the flux function that reproduces the best the observed acceleration. 89
6.17 Wind solution for the spine and the sheath. 91

List of Tables

4.1 Performance of the SWD detection compared to a direct detection (DD) in terms of SNR at which at 95% of the simulated features are detected. 37

6.1 Velocity components identified from stacked cross correlation analysis of the northern and southern region at distances between 0.5 and 1 mas from the core. 69

6.2 Velocity components identified from stacked cross correlation analysis of the northern, central and southern region at distances between 1 and 4 mas from the core. 69

6.3 Parameters for jet rotation estimated in region A (0.5 mas $\leq z_{\mathrm{obs}} \leq$ 1 mas) and region B 1 mas $\leq z_{\mathrm{obs}} \leq$ 3 mas for $\theta = 18°$. 78

6.4 Angular velocity and launching location estimated in region A (0.5 mas $\leq z_{obs} \leq$ 1 mas) and for the fast component of region B (1 mas $\leq z_{obs} \leq$ 3 mas) for $\theta = 18°$. 81

6.5 Best fit parameters reproducing the observed acceleration and collimation using asymptotic relations in the far-zone of the Poynting dominated approximation. 85

6.6 Parameters for the wind solution that best reproduces the observed acceleration for the three models of the flux function. 90

Acknowledgement

I would like to conclude this dissertation by expressing my gratitude to all the people that helped and supported me these last years.

I am indebted first and foremost to my advisor, Andrei Lobanov, this thesis would just not have been possible without him. During these three years he always had the right advice to advance on this project, contributing with a lot of ideas, the sanes and the crazies. He was also an invaluable person during the hard times, always knowing what to say to keeps me motivated, and was generally a wonderful person to talk with.

I am grateful to Prof. Anton Zensus for giving me the opportunity to work on this project, and giving me support and resource. I also take this opportunity to thanks the members of my thesis committee, Prof. Andreas Eckart, Tuomas Savolainen and Olaf Wucknitz for their guidance, and for making sure that I was staying on the right track. My thanks should go as well to Manolis Angelakis and Simone Pott for kindly assisting me during these years regarding all IMPRS matters.

The world of VLBI is a strange place, and the road towards mastering this technique is adventurous at will. In this regards, I was greatly helped with the unique expertise of the people of the VLBI group. I could not have better guide than Andrei and Tuomas for this. I also want to thanks Richard Porcas for sharing his deep experience of VLBI.

I would like to sincerely thanks Craig Walker for sharing the data of his wonderful M87 VLBA movie project, and Philip Hardee for his suggestions and comments that helped me interpreting the kinematic of this source. I also acknowledge the MOJAVE team in general for the use of data from their monitoring program. I think that it should be mention how an amazing job they are doing.

This list would not be complete without mentioning the wonderful people of the VLBI group, starting from my current and previous office mates Dhanya, Ioannis Bindu and Jeff, the fellows PhD students next door, Bia and Vassilis who helped me make this stay enjoyable. I am really grateful to Christoph who did a great job translating the abstract into German language.

There is always a special thanks, and this one goes without any doubt to Norma, who encouraged me starting this PhD, was always supportive when I needed it. My last thanks should go to my parents Maryline and Léo in this small village in the middle of France where I am from.

Erklärung

Ich versichere, dass ich die von mir vorgelegte Dissertation selbständig angefertigt, die benutzten Quellen und Hilfsmittel vollständig angegeben und die Stellen der Arbeit, einschließlich Tabellen, Karten und Abbildungen, die anderen Werken im Wortlaut oder dem Sinn nach entnommen sind, in jedem Einzelfall als Entlehnung kenntlich gemacht habe; dass diese Dissertation noch keiner anderen Fakultät oder Universität zur Prüfung vorgelegen hat; dass sie, abgesehen von unten angegebenen Teilpublikationen – noch nicht veröffentlicht worden ist sowie, dass ich eine solche Veröffentlichung vor Abschluss des Promotionsverfahrens nicht vornehmen werde. Die Bestimmungen der Promotionsordnung sind mir bekannt. Die von mir vorgelegte Dissertation ist von Prof. Dr. J. Anton Zensus und Prof. Dr. Andreas Eckart betreut worden.

Köln, den 14.11.2013

Teilpublikationen

Mertens, F., & Lobanov, A. 2015, "*Wavelet-based decomposition and analysis of structural patterns in astronomical images*" A&A, 574, AA67

Mertens, F., & Lobanov, A. 2014, "*Longitudinal and transverse velocity fields in parsec-scale jets*", Proceedings of the 12th European VLBI Network Symposium and Users Meeting (EVN 2014). 7-10 October 2014. Cagliari, Italy.

Lebenslauf

Florent Mertens

Geburtsdatum	02. October 1983
Geburtsort	Tulle (Frankreich)
Staatsangehörigkeit	Französisch
Telefon	+49 (221) 42361704
E-mail	florent.mertens@gmail.com; fmertens@mpifr.de
Wohnort	Sürther Str. 59 50996 Köln

Ausbildung

2014	Ph.D., Universität Köln, Deutschland: “Internal structure and dynamics of extragalatic relativistic jets”
2006	**Master of Science in Physics**, University Paris XI, Paris, France.
2005	**Bachelor of Science in Physics**, University Paris XI, Paris, France.
2001	**Abitur**, Lycée Edmond Perrier, Tulle, France

Arbeitserfahrung

2010 - 2012	**Software Entwickler**, Recommind, Bonn, Germany. Feature-Entwicklung einer Unternehmenssuche und Inhaltskategorisierung Software; Qualitätssicherung, Unit-Test und automatische Testentwicklung.
2007 - 2012	**Ingenieur**, Paris Observatory (LESIA), Paris, France. Datenmanager für die COROT Satelliten. Verwaltung der Datenbank; Datenqualitätssicherung; Entwicklung von Anwenderprogramm und Web-Anwendungen für die Verwaltung und die Visualisierung der Daten.
2006	**Diplomarbait**, ONERA, Paris, France Erarbeitung einer Methode, um Vibrationen für die extreme adaptive Optiksystem SPHERE erkennen.